



**FORMATION OF HARD MAGNETITE DEPOSITS IN SIMULATED  
PRESSURIZED WATER REACTOR STEAM GENERATOR ENVIRONMENT**

Lappeenranta–Lahti University of Technology LUT

Energy technology

Master's thesis

2022

Veera Peltonen

Examiners: Juhani Hyvärinen, Professor, D. Sc. (Tech.)

Konsta Sipilä, Senior Scientist, M.Sc. (Tech.)

## Abstract

Lappeenranta–Lahti University of Technology LUT

LUT School of Energy Systems

Energy Technology

Veera Peltonen

### **Formation of hard magnetite deposits in simulated pressurized water reactor steam generator environment**

Master's thesis

2022

77 pages, 38 figures, 22 tables and 5 appendices

Examiners: Professor, D. Sc. (Tech.) Juhani Hyvärinen

Senior Scientist, M. Sc. (Tech.) Konsta Sipilä

Supervisor: Senior Scientist, M. Sc. (Tech.) Konsta Sipilä

Keywords: magnetite, deposition, hardening, steam generator, secondary circuit, SEM, EDS

The integrity of the steam generators has a significant impact on the safety and long-term operation of the pressurized water reactor nuclear power plants. The corrosion of secondary circuit materials subjects steam generators to various degradation phenomena and reduces plant efficiency as corrosion products may deposit on steam generator surfaces and harden. This master's thesis focuses on studying the deposition and especially the hardening of the corrosion product, magnetite, in simulated steam generator conditions.

The deposition and hardening of magnetite were studied with two experimental setups. The in-situ laboratory system allowed real-time observation of deposit formation at atmospheric pressure and temperatures up to 100 °C. The detected processes are analyzed by electrochemical impedance spectroscopy and modelled with simple equivalent circuits. The second setup, pipe cell, enabled to perform magnetite hardening experiments in simulated steam generator conditions and estimate the deposition effects to heat transfer properties. The cell samples are examined by scanning electron microscopy and energy dispersive spectrometry to analyze microscopic properties.

When imaging the pieces from the regions of the pipe cell experiment, various surface morphologies were observed indicating different deposition behaviour of magnetite. The imaging of the filtrations cast in SEM resin was challenging due to the applied alumina and silica, but at the same time helped to highlight the small differences between the experiments. No formation of uniform deposits was achieved with the in-situ EIS laboratory equipment and only the oxide layer on the metal surface and the electrical double layer was detected in the recorded impedance spectrum. Unfortunately, this experimental setup broke down in the middle of the last experiment, but a new version is already being designed for possible further studies.

## Tiivistelmä

Lappeenrannan–Lahden teknillinen yliopisto LUT

LUT School of Energy Systems

Energiatekniikka

Veera Peltonen

### **Kovien magnetiittikerrostumien muodostuminen simuloitussa painevesireaktorin höyrystinympäristössä**

Energiatekniikan diplomityö

2022

77 sivua, 38 kuvaa, 22 taulukkoa ja 5 liitettä

Tarkastajat: Professori, TkT Juhani Hyvärinen

DI Konsta Sipilä

Ohjaaja: DI Konsta Sipilä

Avainsanat: magnetiitti, saostuminen, kovettuminen, höyrystin, sekundääripiiri, SEM, EDS

Höyrystimien kunnolla on merkittävä vaikutus painevesireaktoriydinvoimalaitosten turvallisuuteen ja pitkäaikaiseen toimintaan. Sekundääripiirin materiaalien korroosio altistaa höyrystimet erilaisille vaurioitumisilmiöille ja heikentää laitoksen hyötysuhdetta, koska korroosiotuotteet voivat saostuvat höyrystimen pinnoille ja kovettua. Tässä diplomityössä keskitytään korroosiotuotteen, magnetiitin, saostumiseen ja erityisesti kovettumiseen simuloituissa höyrystinolosuhteissa.

Magnetiitin saostumista ja kovettumista tutkittiin kahdella koelaitteistolla. Laboratoriojärjestelmä mahdollisti saostuman reaaliaikaisen havainnoinnin ilman paineessa ja jopa 100 °C:n lämpötiloissa. Havaitut prosessit analysoitiin sähkökemiallisella impedanssispektroskopialla ja mallinnettiin yksinkertaisilla ekvivalenttipiireillä. Toinen koelaitteisto, putkikkenno, mahdollisti magnetiitin kovettumiskokeiden toteuttamisen simuloituissa höyrystinolosuhteissa sekä saostuman vaikutuksen arvioinnin lämmönsiirtoon. Kennonäytteitä tutkittiin pyyhkäisyelektronimikroskoopilla ja energiadiispersiivisellä spektrometrialla pienten ominaisuuksien havaitsemiseksi.

Kuvattaessa näytteitä putkikennokokeiden alueilta havaittiin erilaisia pinnan muotoja viitaten magnetiitin erilaisiin saostumiin. Valettujen suodatusten kuvantaminen oli haastavaa kokeissa käytettyjen alumiini- ja piidioksidin vuoksi, mutta samalla ne auttoivat tuomaan esiin pieniä eroja kokeiden välillä. Laboratoriolaitteistolla ei saatu muodostettua yhtenäisiä saostumia, ja impedanssispektristä havaittiin vain metallin pinnalla oleva oksidi- ja sähköinen kaksoiskerros. Valitettavasti tämä koelaitteisto hajosi kesken viimeisen kokeen, mutta uutta versiota suunnitellaan jo mahdollisia jatkotutkimuksia varten.

## ACKNOWLEDGEMENTS

This thesis was conducted at the VTT Technical Research Centre of Finland in Espoo in the research team Advanced material for nuclear energy from November 2021 to May 2022.

I would especially like to thank my thesis supervisor Senior Scientist Konsta Sipilä for his professional insights and support. A big thank you also goes to Senior Research Engineer Seppo Peltonen, without whom none of the experimental setups would exist or work. Last but not least, thanks to the rest of my co-workers at Kemistintie for the warm welcome and cheerful atmosphere.

I am extremely happy to have had a wonderful time studying in Lappeenranta, for which I can express my gratitude to all my amazing friends. Thanks to the energy technology student organisation Armatuuri Ry for the eventful board years and the warmth and student-filled guild room. Also, a special thank you to Professor Juhani Hyvärinen for sparking my interest in nuclear energy.

In Espoo on June 3<sup>rd</sup>, 2022

*Veera Peltonen*

## SYMBOLS AND ABBREVIATIONS

### Roman characters

|          |                           |                       |
|----------|---------------------------|-----------------------|
| <i>A</i> | area                      | m <sup>2</sup>        |
| <i>C</i> | capacitance               | F                     |
| <i>E</i> | potential                 | V                     |
| <i>f</i> | frequency                 | Hz                    |
| <i>h</i> | heat transfer coefficient | W/(m <sup>2</sup> °C) |
| <i>I</i> | current                   | A                     |
| <i>k</i> | thermal conductivity      | W/(m°°C)              |
| <i>L</i> | length                    | m                     |
| <i>p</i> | pressure                  | bar                   |
| <i>Q</i> | charge                    | C, As                 |
| <i>q</i> | heat transfer rate        | W                     |
| <i>R</i> | resistance                | Ω                     |
| <i>r</i> | radius                    | m                     |
| <i>T</i> | temperature               | °C, K                 |
| <i>t</i> | time                      | s                     |
| <i>U</i> | voltage                   | V                     |
| <i>W</i> | Warburg impedance         | Ω                     |
| <i>Z</i> | impedance                 | Ω                     |

### Greek characters

|           |                   |       |
|-----------|-------------------|-------|
| $\varphi$ | phase angle       | °     |
| $\omega$  | angular frequency | rad/s |
| $\zeta$   | zeta potential    | V     |

### Abbreviations

|     |                          |
|-----|--------------------------|
| AC  | Alternating current      |
| AVT | All volatile treatment   |
| BWR | Boiling water reactor    |
| BSE | Back-scattered electrons |
| C   | Carbon                   |
| Cr  | Chromium                 |

|                                |  |
|--------------------------------|--|
| Cu                             | Copper   |
| EDL                            | Electrical double layer                                  |
| EDS                            | Energy dispersive spectrometry                           |
| EIS                            | Electrochemical impedance spectroscopy                   |
| EPK                            | Electrokinetic phenomena                                 |
| EPR                            | European pressurized water reactor                       |
| FAC                            | Flow-accelerated corrosion                               |
| Fe                             | Iron   |
| Fe <sub>2</sub> O <sub>3</sub> | Hematite   |
| Fe <sub>3</sub> O <sub>4</sub> | Magnetite  |
| H                              | Hydrogen   |
| H <sub>2</sub> O               | Water  |
| HCl                            | Hydrogen chloride  |
| IAEA                           | International Atomic Energy Agency                       |
| ICP-OES                        | Inductively Coupled Plasma Optical Emission Spectroscopy |
| IEP                            | Isoelectric point  |
| LOCA                           | Loss-of-Coolant Accident                                 |
| MgCl <sub>2</sub>              | Magnesium chloride                                       |
| Mg(OH) <sub>2</sub>            | Magnesium hydroxide                                      |
| Mn                             | Manganese  |
| N                              | Nitrogen   |
| NH <sub>3</sub>                | Ammonia  |
| N <sub>2</sub> H <sub>4</sub>  | Hydrazine  |
| Ni                             | Nickel   |
| NPP                            | Nuclear power plant                                      |
| O                              | Oxygen   |
| OH                             | Hydroxide  |
| P                              | Phosphorus   |
| PWR                            | Pressurized water reactor                                |
| PZC                            | Point of Zero Charge                                     |
| S                              | Sulphur  |
| SC                             | Secondary circuit  |

|                  |  |
|------------------|--|
| SCC              | Stress corrosion cracking                |
| SE               | Secondary electrons                      |
| SEM              | Scanning electron microscope             |
| SG               | Steam generator                          |
| SiO <sub>2</sub> | Silica                                   |
| Ti               | Titanium                                 |
| VTT              | Technical Research Centre of Finland Ltd |
| VVER             | Water-water energetic reactor            |

## TABLE OF CONTENTS

|  |    |
|--|----|
| Abstract.....  | 2  |
| Tiivistelmä .....  | 3  |
| Symbols and abbreviations .....  | 5  |
| Table of contents.....   | 8  |
| 1 Introduction .....   | 10 |
| 2 Secondary circuit of the pressurized water reactor and related corrosion phenomena | 13 |
| 2.1 Steam generator.....   | 14 |
| 2.2 Water chemistry .....  | 16 |
| 2.3 Corrosion in the secondary circuit .....   | 18 |
| 2.3.1 Flow-accelerated corrosion.....  | 21 |
| 2.3.2 Corrosion related issues in steam generator .....                              | 23 |
| 3 Factors affecting magnetite deposition and formation of hard deposits.....         | 32 |
| 4 Research methods.....  | 36 |
| 4.1 High-pressure and temperature magnetite cell.....                                | 36 |
| 4.1.1 Heat transfer calculation .....  | 41 |
| 4.1.2 Ex-situ characterization with scanning electron microscope.....                | 43 |
| 4.2 Experimental setup for in-situ monitoring of deposit formation .....             | 46 |
| 4.2.1 Electrochemical Impedance Spectroscopy .....                                   | 48 |
| 5 Results and conclusions.....   | 53 |
| 5.1 Heat transfer in the magnetite pipe cell.....                                    | 53 |
| 5.2 Gravimetric measurement .....  | 55 |
| 5.3 SEM and EDS results.....   | 58 |
| 5.4 EIS results and equivalent circuit analysis.....                                 | 61 |
| 5.5 Error analysis .....   | 65 |
| 5.5.1 Heat transfer.....   | 65 |
| 5.5.2 SEM and EDS .....  | 67 |
| 5.5.3 In-situ deposit monitoring setup .....   | 68 |
| 6 Future considerations.....   | 71 |
| 7 Summary.....   | 73 |
| References.....  | 74 |



## Appendices

Appendix I High-pressure and temperature magnetite cells

Appendix II Temperature and pressure data measurements from the magnetite cell experiments

Appendix III Filtrations with Zeiss Axio Zoom V16 microscope

Appendix IV SEM images and elemental maps

Appendix V EIS – Nyquist and Bode plots

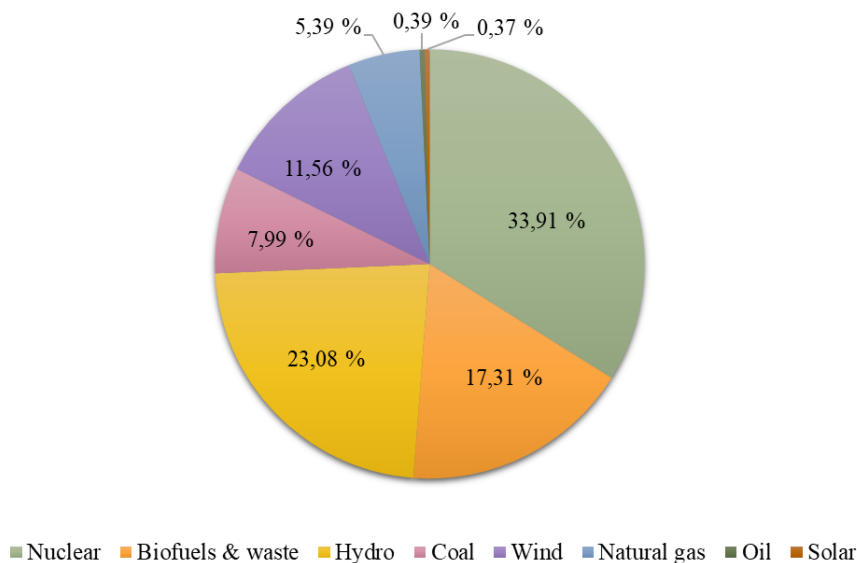
## 1 INTRODUCTION

Finland has four operating nuclear reactors, with a combined net capacity of 2,8 GW<sub>e</sub>. Loviisa nuclear power plant (NPP) and Olkiluoto nuclear power plant both have two operating units. Loviisa 1 is the first NPP unit in Finland. The Loviisa units are modified Soviet-designed pressurized water reactors (water-water energy reactor, VVER) and the Olkiluoto units are boiling water reactors (BWR). The third unit at Olkiluoto is a European pressurized water reactor (EPR), which is expected to begin commercial operation in mid-2022. (World Nuclear Association 2022) Table 1.1 contains information about Finnish nuclear power plant types, their electricity generation capacities and commissioning dates.

**Table 1.1.** Nuclear power in Finland. (World Nuclear Association 2022)

| NPP         | Reactor type and model | Capacity [MW <sub>e</sub> ] | Commercial operation          | Operator |
|-------------|------------------------|-----------------------------|-------------------------------|----------|
| Loviisa 1   | VVER-440 V-213         | 507                         | 9 <sup>th</sup> May 1977      | Fortum   |
| Loviisa 2   | VVER-440 V-213         | 507                         | 5 <sup>th</sup> January 1981  | Fortum   |
| Olkiluoto 1 | BWR-2500               | 890                         | 10 <sup>th</sup> October 1979 | TVO      |
| Olkiluoto 2 | BWR-2500               | 890                         | 10 <sup>th</sup> July 1982    | TVO      |
| Olkiluoto 3 | EPR                    | 1 720                       | June 2022                     | TVO      |

In 2020, nuclear generated 33,9% of the country's electricity (World Nuclear Association 2022). Finland's electricity production by source in 2020 is presented in Figure 1.1.



**Figure 1.1.** Electricity generation by source 2020 (data from IEA 2022).

The safety of nuclear energy is an important issue. Efforts are being made to improve and optimize the safety and long-term operation of nuclear power plants. Materials used in the plants must meet certain safety requirements, so the behavior and integrity of materials must be considered during the lifetime of the plant. The corrosion of these materials and related issues are a major concern for the safety and lifetime of the plant. (Féron 2012)

Corrosion reactions occurring in the secondary circuit of a PWR causes a release of particles, which can be minimized by either limiting the formation of corrosion products, preventing their precipitation, or removing them from the circuit. Corrosion products, mainly magnetite, interfere with the normal operation of the plant by forming deposits in the steam generator (SG). This limits the heat transfer between primary and secondary circuits and can alter the water chemistry locally, subjecting the structural materials to localized corrosion and stress corrosion cracking (SCC). Construction materials, water chemistry and plant operation influence the formation of corrosion products and their precipitation. The water chemistry must be suitable for all parts of the secondary circuit.

Based on the above premises, the aim of this thesis is to study the factors influencing the deposition of magnetite, in particular its hardening in the steam generators. The hardened deposit adheres to the surface so tightly that the surrounding liquid can no longer remove it. The formation of such a hardened layer is influenced by temperature, particle precipitation, solubility and thus its porosity (Vepsäläinen 2010). The deposition and hardening of magnetite in the steam generator of a PWR is simulated using two different experimental setups. These setups enable the study of deposition and hardening phenomena by adjusting the following parameters: water chemistry, applied chemicals, temperature, and time.

This thesis first discusses the conditions and corrosion phenomena in the secondary circuit of a PWR. The problems caused by corrosion in the steam generators are discussed in more detail in subsection 2.3. The interparticle forces and their effect on magnetite deposition is examined in section 3. The electric double layer and zeta potential are used to explain the deposition processes of colloidal particles such as magnetite.

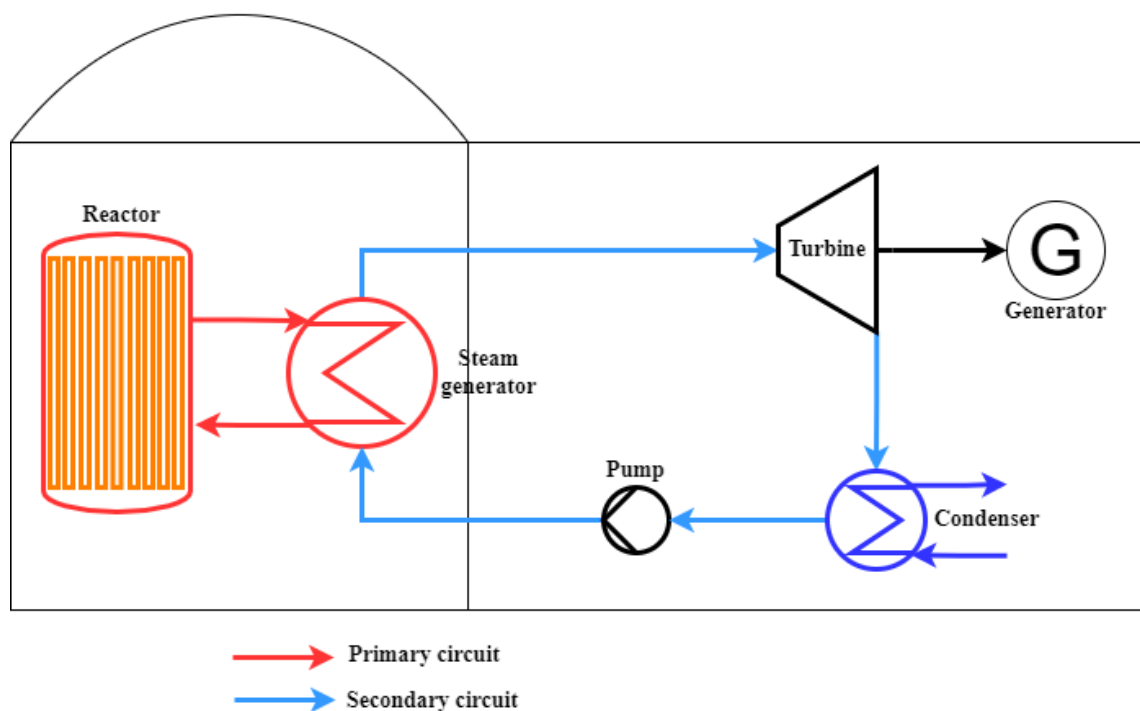
Most of the deposits that form on steel surfaces under secondary circuit conditions are magnetite ( $\text{Fe}_3\text{O}_4$ ), and therefore, understanding its behavior under these conditions is important for simulating deposition in steam generators. For this thesis, VTT Technical Research Centre of Finland in Espoo developed two experimental setups for magnetite

deposition and hardening studies: in-situ laboratory equipment, and high-pressure and temperature pipe cell. The laboratory system allows in-situ monitoring of deposition at atmospheric pressure and up to 100 °C. The suitability of electrochemical impedance spectroscopy (EIS) for in-situ deposit monitoring was also experimented. In contrast, the high-pressure and temperature cell enables studies in representative pressure, temperature, and water chemistry of power plants. Scanning electron microscopy (SEM) is used to examine the results of the experiment to see the structural differences in the deposition in different cell samples. At the same time, energy dispersive spectrometry (EDS) enables the determination of the elemental distribution of the sample.

Section 5 presents and analyses the results of the experiments. The results of the pipe cell experiment focus on the heat transfer during the experiments and the quality and quantity of the samples. Outcome of the laboratory system is based on the visual observation during the experiments and the data graphs analyzing afterwards. The electrochemical response of the system obtained with EIS can be used to further model the detected processes with a simple equivalent circuits.

## 2 SECONDARY CIRCUIT OF THE PRESSURIZED WATER REACTOR AND RELATED CORROSION PHENOMENA

The operating principle of a NPP is based on fission, and the utilization of the thermal energy it produces to generate electricity. The PWR uses light water as a coolant and moderator. PWRs consist of two separate circuits: primary and secondary. The coolant in the primary circuit is kept under high pressure so that it cannot boil even when the temperature rises to approximately 300 °C. The heated cooling water is then fed to steam generators, where it evaporates the feedwater in the secondary circuit. Steam is generated and fed to the turbines to produce electricity. The steam from the turbine is condensed and pumped back to the to the steam generator. (Breeze, 2014) Basic principle of PWR and its circuits are illustrated in Figure 2.1.



**Figure 2.1.** Schematic of a PWR.

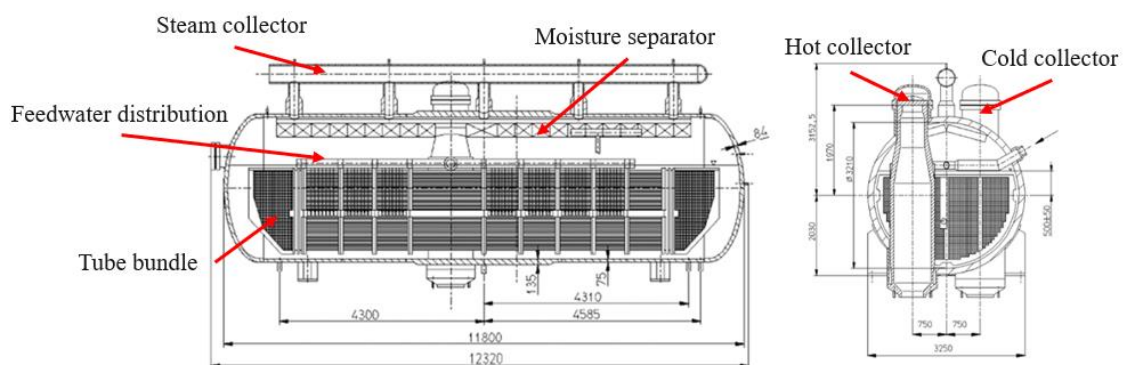
Conditions in the secondary circuit vary significantly between different parts of the water-steam circuit. Conditions, such as temperature, pressure, and flow rates, set certain demands on the circuit materials. Corrosion and related problems are one of the main challenges for the plant in terms of operating life and safety.

## 2.1 Steam generator

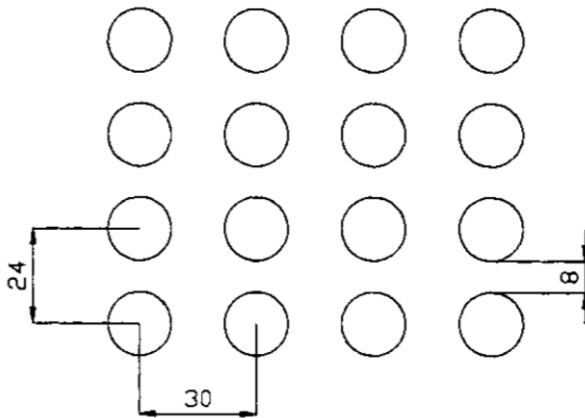
Steam generators can be considered one of the most important components in NPP because they have an important influence on the safe and long-term operation of the NPP. The main purpose of SG is heat transfer from the radioactive primary side to the secondary side of SG where the steam is generated. (Kritsky 1999)

Primary coolant enters the SG through a vertical hot collector, travels through the horizontal U-shaped submerged tubing, and exits through a vertical cold collector. Primary coolant releases heat to the secondary side feedwater, which is distributed above the tube bundles. Feedwater evaporates and its excess moisture is removed via moisture separator by gravitational separation and converted steam is collected. (Kang et al. 2011)

The steam generator pressure vessel is a horizontal cylinder with elliptical heads. The vertical hot and cold collectors are near the vessel center. A cross-sectional view of the SG is shown in Figure 2.2. U-tubes are arranged in corridor and attached to the collectors, which act as “tubesheets”. The tube bundle arrangement is presented in Figure 2.3. The steam generator has an excess number of tubes so that the tubes do not need to be replaced if a fault is detected during an inspection but are plugged instead. It is important to check the tubes because the radioactive water circulating on the primary side must not mix with the uncontaminated secondary side feedwater. (Riznic 2017) Details of the steam generator characteristics are given in Table 2.1.



**Figure 2.2.** Cross section of the VVER-440 steam generator. (Slugeň 2011)



**Figure 2.3.** Tube bundle arrangement. (Trunov and Dragunov 2004)

**Table 2.1.** Design and thermal characteristics of VVER-440 steam generator. (Kritsky 1999)

| Characteristics                                | VVER-440 |
|--|----------|
| Number of SG per one reactor [-]               | 6        |
| Length [mm]                                    | 11 950   |
| Inner diameter [mm]                            | 3 210    |
| Max height of tube bundle [mm]                 | 1 900    |
| Number of the tubes [-]                        | 5 146    |
| Diameter of the tubes [mm]                     | 16 × 1,4 |
| Average tube length [mm]                       | 8 700    |
| Tube bundle arrangement                        | Corridor |
| Tube bundle spacing (vertical/horizontal) [mm] | 24/29,5  |
| SG heating surface [m <sup>2</sup> ]           | 2 500    |
| P <sub>e</sub> per one SG [MW]                 | 73,3     |
| Coolant temperature at SG inlet/outlet [°C]    | 301/268  |
| Coolant velocity in tubes [m/s]                | 2,70     |
| Coolant pressure [Mpa]                         | 12,5     |
| Feedwater temperature [°C]                     | 226      |
| Steam pressure [Mpa]                           | 4,6      |
| Steam temperature [°C]                         | 259      |
| Steam capacity [kg/s]                          | 125      |

Steam generator tubes and collectors are made from stabilized austenitic stainless-steel alloy 08Cr18Ni10Ti. The alloy is equivalent to AISI 321. The vessel is made from carbon steel 22K. (IAEA 2011) The composition of both mentioned alloys are given in Table 2.2.

**Table 2.2.** Chemical composition of VVER steam generator materials [mass-%]. (Riznic 2017)

| Element | 08Cr18Ni10Ti     | 22K         |
|---------|------------------|-------------|
| C       | $\leq 0,08$      | 0,19 – 0,26 |
| Cr      | 17 – 19          | $\leq 0,3$  |
| Ni      | 10 – 11,5        | $\leq 0,3$  |
| Ti      | $\geq 0,4$ – 0,6 |             |
| Mn      | $\leq 1,5$       | 0,75 – 1,0  |
| Si      | $\leq 0,8$       | 0,2 – 0,4   |
| Co      | $< 0,3$          |             |
| Cu      | $< 0,3$          |             |
| S       | $< 0,02$         | 0,03        |
| N       | $< 0,05$         |             |
| P       | $< 0,035$        | 0,03        |

The horizontal position of the steam generator makes the component technologically effective and safe to operate, which leads to several advantages, such as a large cooling water storage in case of LOCA, good accessibility and a large heat exchange surface. The steam generator is the most corrosion-sensitive component of a NPP due to its challenging internal conditions and complicated material composition and structure. That and other disadvantages must be considered during the operation and maintenance of a NPP. (Slugeň 2011)

## 2.2 Water chemistry

The aim of secondary water chemistry is to minimize the formation of deposits in the circuit, prevent corrosion damage to circuit materials and maintain the effective operation of the plant. To achieve this, the water chemistry must be properly implemented for all parts of the secondary circuit: steam generators (SGs), turbines, condensers, feedwater heaters, moisture separator reheaters and piping. Deposits can form on the heat transfer surfaces of the steam generator, turbine flow paths and condensate-feed piping, for example. This increases the potential risk of corrosion and reduces the plant efficiency. (Tyapkov and Erpyleva 2017)

The secondary side water chemistry selected to protect SGs is usually also satisfactory for all of the secondary side components. Secondary water chemistry control at PWR should be operated according to an “all volatile treatment (AVT)” or an “all volatile treatment with

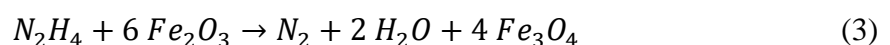


high pH". This treatment uses only volatile alkaline reagents such as ammonia and/or amines and a reducing agent is added if necessary. The use of ammonia, amines and reducing agents and their concentrations are site-specific. The concentrations should be such that the secondary circuit has an appropriate pH value. The values are chosen so that flow-accelerated corrosion (FAC) of carbon steels is avoided or minimized, limiting the amount of corrosion products transport into the SG, and they are compatible with the materials of the circuit and its cleaning systems. (IAEA 2011)

Typical amines for preventing FAC are monoethanolamine (ETA) and morpholine (MPH). Ammonia (NH<sub>3</sub>) is not an amine but is used as one. These amines are compared in Table 2.3. Hydrazine (N<sub>2</sub>H<sub>4</sub>) is used as an oxygen scavenger, but it also acts as a corrosion inhibitor. In its main function, hydrazine reacts with oxygen to form water and nitrogen. It can also potentially raise the pH if oxygen is not present when it decomposes to ammonia. (Kang et al. 2011) Hydrazine can operate as a passivator and contribute to the formation of a protective oxide layer. These reactions are presented in chemical equations (1), (2) and (3). (Li et al. 2020)

**Table 2.3.** Characteristics of ammonia and amines. (Tyapkov and Erpyleva 2017)

| Amine        | Chemical formula                                  | Molar mass [g/mol] | Dissociation constant -log(K <sub>b</sub> ) |      |      | Steam/water partition coefficient K <sub>p</sub> |      |      |
|--------------|---|--------------------|---|------|------|--|------|------|
|              |   |                    | Temperature [°C]                            |      |      |  |      |      |
|              |   |                    | 25  | 150  | 300  | 25   | 150  | 300  |
|              |   |                    |   |      |      |  |      |      |
| Ammonia      | NH <sub>3</sub>                                   | 17,034             | 4,76  | 5,13 | 6,83 | 30,2   | 10,0 | 3,23 |
| Morpholine   | C <sub>4</sub> H <sub>8</sub> ONH                 | 87,122             | 5,5   | 5,3  | 6,63 | 0,12   | 0,77 | 1,29 |
| Ethanolamine | C <sub>2</sub> H <sub>4</sub> (OH)NH <sub>2</sub> | 61,083             | 4,5   | 4,83 | 6,4  | 0,004  | 0,11 | 0,66 |



A typical water chemistry for VVER SGs has initially been ammonia and/or hydrazine. As the copper alloys have been removed from the secondary circuit and replaced with stainless steel or titanium, there is the possibility of using higher concentrations of ammonia and

increase the pH of the circuit, which in turn lowers the corrosion rate of carbon steel and reduces the risk of SG corrosion. (Féron 2012) The different water chemistries and their parameters used in VVERs are given in Table 2.4.

**Table 2.4.** VVER water chemistry specifications. (Kang et al. 2011)

| Parameter                                       | Hydrazine-<br>ammonia | Morpholine | Ammonia-<br>ethanolamine |
|---|-----------------------|------------|--------------------------|
| pH <sub>25°C</sub>                              | 8,8–9,2               | 8,9–9,3    | 9,3–9,7                  |
| Conductivity [ $\mu\text{S}/\text{cm}$ ]        | $\leq 0,3$            | $\leq 0,3$ | 0,3                      |
| Hydrazine [ $\mu\text{g}/\text{l}$ ]            | $\geq 20$             | $\geq 10$  | 10                       |
| Morpholine [ $\mu\text{g}/\text{l}$ ]           | -                     | 2,5–4,5    | -                        |
| Ammonia [ $\mu\text{g}/\text{l}$ ]              | -                     | -          | 800–3000                 |
| Ethanolamine                                    | -                     | -          | 300–800                  |
| Dissolved oxygen<br>[ $\mu\text{g}/\text{kg}$ ] | 10                    | 10         | 5                        |
| Iron [ $\mu\text{g}/\text{kg}$ ]                | $\leq 15$             | $\leq 10$  | 5                        |

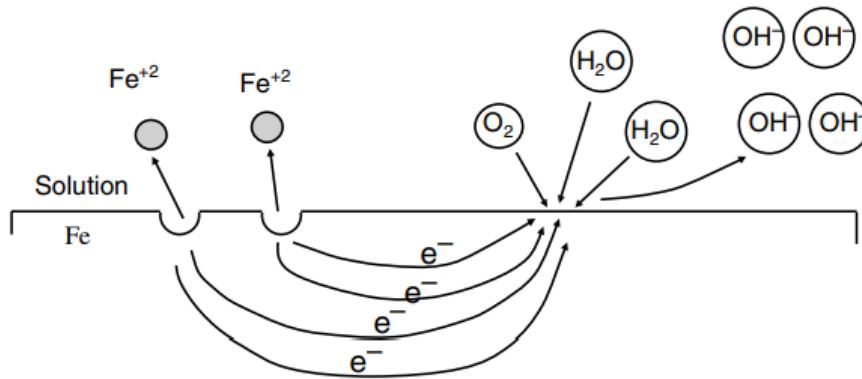
### 2.3 Corrosion in the secondary circuit

Corrosion is degradation of metals by reaction with the environment. Corrosion is either a chemical or electrochemical reaction depending on environmental conditions. (Pederferri 2018)

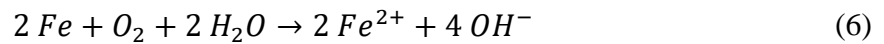
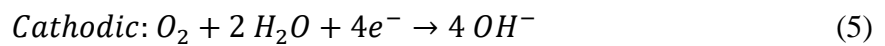
The metal corrosion occurs via electrochemical reactions at the interface between the metal and the solution. The corrosion rate is determined by the equilibrium between two opposing electrochemical reactions. The first is the anodic reaction, in which the metal is oxidized, meaning that electrons are released into the metal. The opposing cathodic reaction receives the released electrons, thereby reducing the solution species. In the chemical equations, the cathodic and anodic reactions can be identified by which side of the equation the electrons are on. In the anodic reaction the electrons are on the right and in the cathodic they are on the left. (Féron 2012)

Corrosion requires an anodic and cathodic reaction, a conductive path between these reaction sites, and an electrolyte. (McCafferty 2010) Figure 2.4 illustrates corrosion of an iron surface, when at certain site iron atoms pass into the solution as  $\text{Fe}^{2+}$  ions and the four free

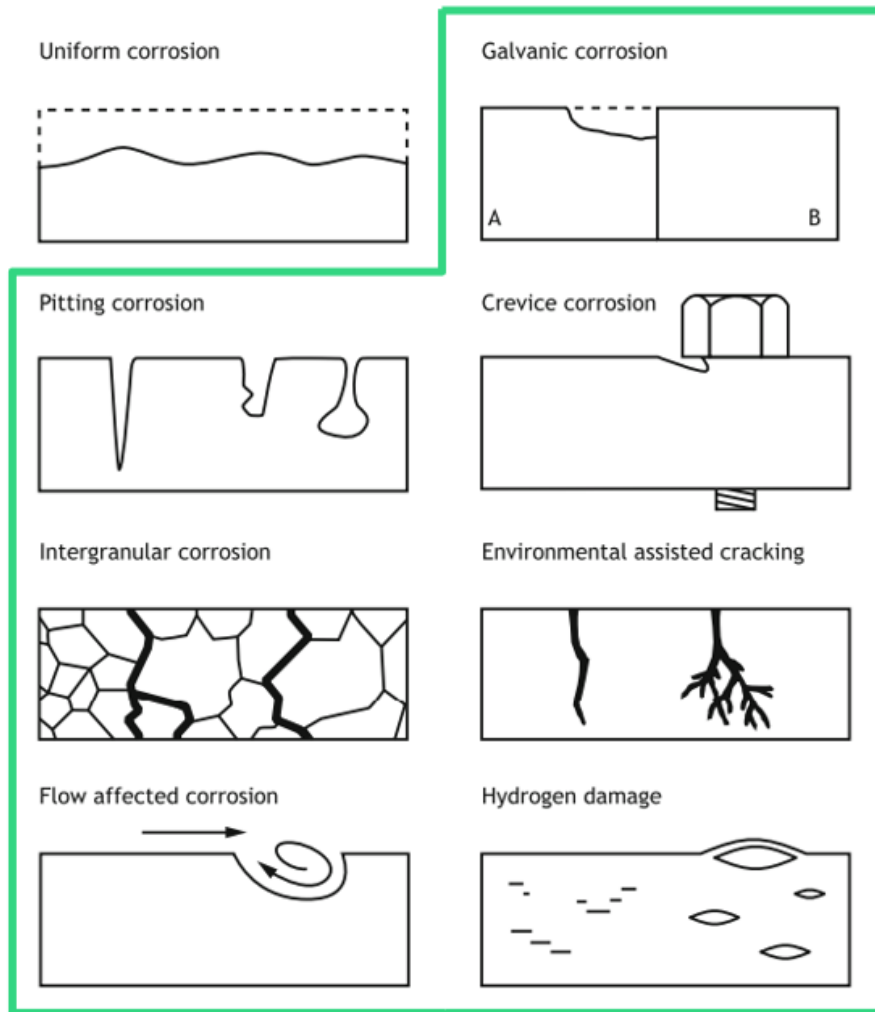
electrons react with oxygen and water to form hydroxide ions  $\text{OH}^-$ . The same phenomenon is also presented in the chemical equations (4), (5) and (6) by anodic, cathodic and their combination reactions. (Féron 2012)



**Figure 2.4.** Anodic and cathodic reactions occurring on iron surface. (McCafferty 2010)



Corrosion affecting the entire surface is uniform (or general) corrosion, and corrosion at a specific area of the surface is called localized corrosion. Localized corrosion can manifest in many different ways. (Pedferri 2018) Uniform corrosion and seven localized corrosion forms are presented in Figure 2.5.



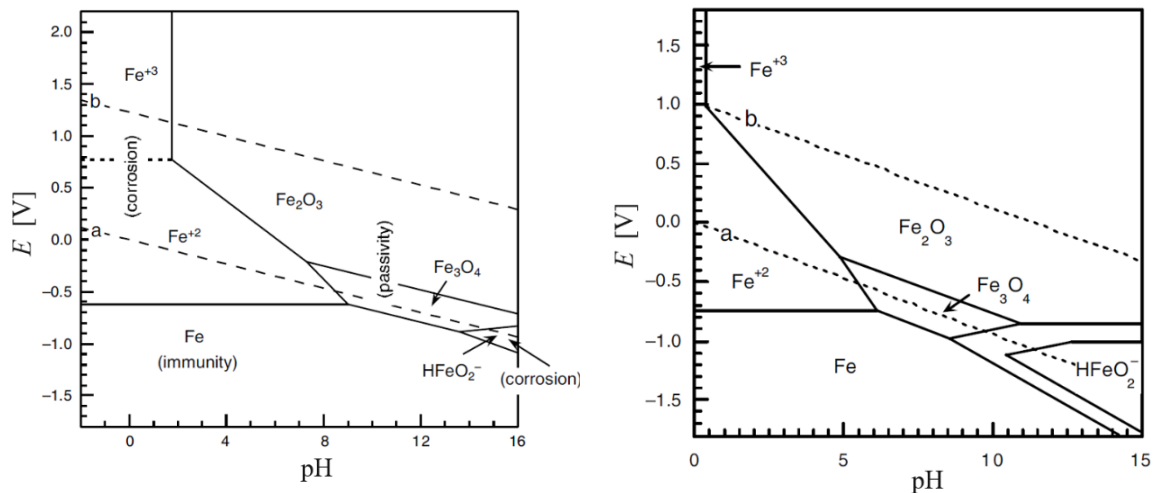
**Figure 2.5.** Different corrosion forms on metals. (Pedferri 2018) Localized corrosion forms are circled with green.

Corrosion damage typically occurs only at the anodic sites. If the alloy is prone to general corrosion, metal thinning will occur rather uniformly, because the anodic and cathodic locations tend to move randomly on the surface of the metal. Metal alloys covered by a passive oxide film are relatively corrosion resistant. On the other hand, in this case the anodic location may localize, which can cause severe localized corrosion damage. (McCafferty 2010)

A protective oxide layer is formed on the metal surface due to an anodic reaction under the suitable potential and pH conditions. The formation of protective or passive layers on the metal surface are called passivation. These passive layers typically have a compact and uniform structure. Passivity is a typical feature of metals such as iron (Fe), chromium (Cr), titanium (Ti), zirconium (Zr) and alloys like stainless steel. (Féron 2012)

The Pourbaix diagram can be used to predict the surface nature of a material under certain environmental and electrochemical conditions. The diagram shows the stability of chemical species as a function of potential and pH. Figure 2.6 presents Pourbaix diagrams for iron. In the immunity zone iron is stable and in the passivity zone it forms  $\text{Fe}_3\text{O}_4$  and  $\text{Fe}_2\text{O}_3$  oxides. The diagram also shows that corrosion can occur at low and high pH. (Pedferri 2018)

The Pourbaix diagram includes oxidation and reduction reactions of water as dashed lines. The oxidation of water takes place on line a and on line b the water is reduced. The difference between these lines is 1,23 V, which is the thermodynamic dissociation potential of water. Most of the corrosion reactions take place between these lines where water is stable. (Murtoimäki et al. 2019)



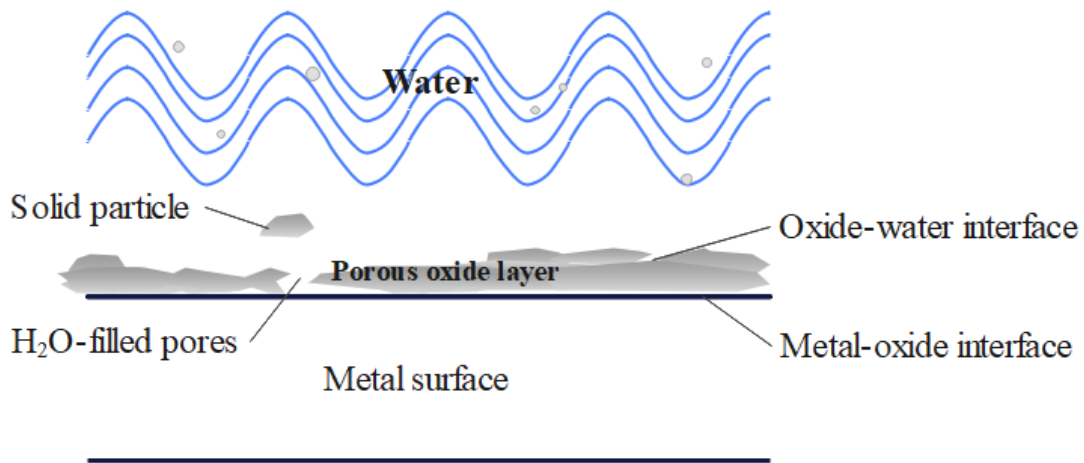
**Figure 2.6.** Pourbaix diagrams for iron at temperatures 25 °C (left) and 200 °C (right). (McCafferty 2010)

### 2.3.1 Flow-accelerated corrosion

Flow-accelerated corrosion (FAC) is an electrochemical corrosion process that occurs under both single and two-phase flow (wet steam) conditions. This corrosion process is strongly influenced by temperature, flow geometry, metal alloy composition and water chemistry. A liquid phase and a metal surface must be present for FAC damage to occur, although it does not cause mechanical removal. (Féron 2012)

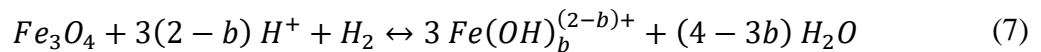
FAC affects carbon steel piping, U-tubes, and single-phase, subcooled feedwater- and wet steam lines. The formed thin protective layer of porous iron oxide, mostly magnetite  $\text{Fe}_3\text{O}_4$ , is dissolved at the oxide–water interface and substituted by new iron oxide from the metal–oxide interface, resulting in material removal and thinning. The FAC process is

demonstrated in Figure 2.7. (Kang et al. 2011) In other words, the metal corrodes to regain the oxide. Therefore, the loss or damage of the metal is continuous.



**Figure 2.7.** A simple model describing the phenomena occurring during FAC.

Magnetite ( $\text{Fe}_3\text{O}_4$ ) dissolution by FAC can be demonstrated with equation (7), where  $\text{Fe}(\text{OH})_b^{(2-b)+}$  represents the different ferrous iron species and  $b$  is 0, 1, 2 or 3. (Ahmed 2012)



Beside magnetite, FAC also releases other iron oxides and oxide hydroxides, such as goethite ( $\alpha\text{-FeOOH}$ ), lepidocrocite ( $\gamma\text{-FeOOH}$ ), maghemite ( $\gamma\text{-Fe}_2\text{O}_3$ ), and hematite ( $\alpha\text{-Fe}_2\text{O}_3$ ) by series of chemical reactions in the secondary circuit environment. These chemical reactions are collected in equations from (8) to (12) in Table 2.5. The reaction rates and environmental factors such as pH, temperature, the solubility of ferrous species, determine which phase(s) of iron oxide predominates in the circuit environment. The most common phases in the secondary side are lepidocrocite ( $\gamma\text{-FeOOH}$ ), magnetite ( $\text{Fe}_3\text{O}_4$ ) and hematite ( $\alpha\text{-Fe}_2\text{O}_3$ ). (Turner 2011)

**Table 2.5.** Iron oxide and oxide hydroxides chemical reactions. (Turner 2011)

| Chemical reaction |  |      |
|-------------------|--|------|
|                   | $3 Fe(OH)_2 \rightarrow Fe_3O_4 + H_2O + H_2$              | (8)  |
| Oxidation         | $2 Fe_3O_4 + \frac{1}{2} O_2 \rightarrow 3 \gamma-Fe_2O_3$ | (9)  |
| Hydrolysis        | $Fe^{2+} + H_2O \rightarrow FeOH^+ + H_2^+$                | (10) |
| Dehydration       | $2 \alpha-FeOOH \rightarrow Fe_2O_3 + H_2O$                | (11) |
| Transformation    | $\gamma-FeOOH + Fe^{2+} \rightarrow Fe_3O_4 + 2 H^+$       | (12) |

### 2.3.2 Corrosion related issues in steam generator

Steam generators have many corrosion problems: stress corrosion cracking (SCC), intergranular attack (IGA), wastage, pitting, and denting. The main corrosion problems affecting the VVER steam generator titanium stabilized austenitic steel tubing are pitting and SCC in the secondary circuit environment. They are associated with deposit accumulation in the tubes due to corrosion product transport into the SG. Corrosion damage of the outer tube surface occurs typically in the form of crevice corrosion at the tube support plates in hot leg and only a limited extent in the cold leg tube section. (Riznic 2017)

Deposit precursors are impurities released from the secondary circuit, which can be transported, dissolved, or deposited by the feedwater flow into the steam generators. These impurities are mainly (~ 90%) corrosion products, primarily magnetite. Sources of magnetite are in particular carbon steel-based materials, as described in the previous chapter. Other sources of impurities include for example condenser leaks, auxiliary feedwater, maintenance, feedwater chemistry additives and breakdown products. (Xie and Zhang 2016) A summary of the impurities is in Table 2.6.

**Table 2.6.** Impurity categories. (Varrin 1996)

| Ionic   | Particulate  | Soluble                                     | Gases   |
|---|--|---|---|
| Sodium<br>Carbonates<br>Chloride<br>Potassium<br>Sulfates<br>Aluminates<br>Iron hydroxides<br>Iron ions | Magnetite<br>Lepidocrocite<br>Maghemite<br>Hematite<br>Silicon dioxide<br>Apatites | Silicious acid<br>Organics<br>Organic Acids | Oxygen<br>Nitrogen<br>Hydrogen<br>Ammonia<br>Carbon Dioxide |

If the deposit precursors do not exit the SG with blow-down or steam, they can transform or decompose to simpler compounds or form deposits. Particulate impurities can accumulate, coalesce, or grow to form sludge. Some sludge adheres to the surface of the steam generator tubes at low flow velocity areas, while some floats in the SG. (Nishida et al. 2002) Ionic species, on the other hand, accumulate in crevices, especially within and underneath deposits. Soluble species and gases also react with the deposits, changing their chemical form and increasing the risk of corrosion. (Varrin 1996)

Impurities will go through a physicochemical changes like consolidation, hideout, precipitation, deposition, and hydrolysis. The most corrosion-prone materials in the secondary circuit are carbon and stainless steels. The corrosion processes of these materials are linked, since first the carbon steel in the feedwater pipes dissolves due to FAC and migrates into the steam generator and deposits on its various surfaces causing fouling. Fouling is defined by EPRI (2003) as “the deposition of corrosion products within the steam generator regardless of their ultimate impact on steam generator performance or integrity”. It can lead to the formation of localized corrosion. (Féron 2012)

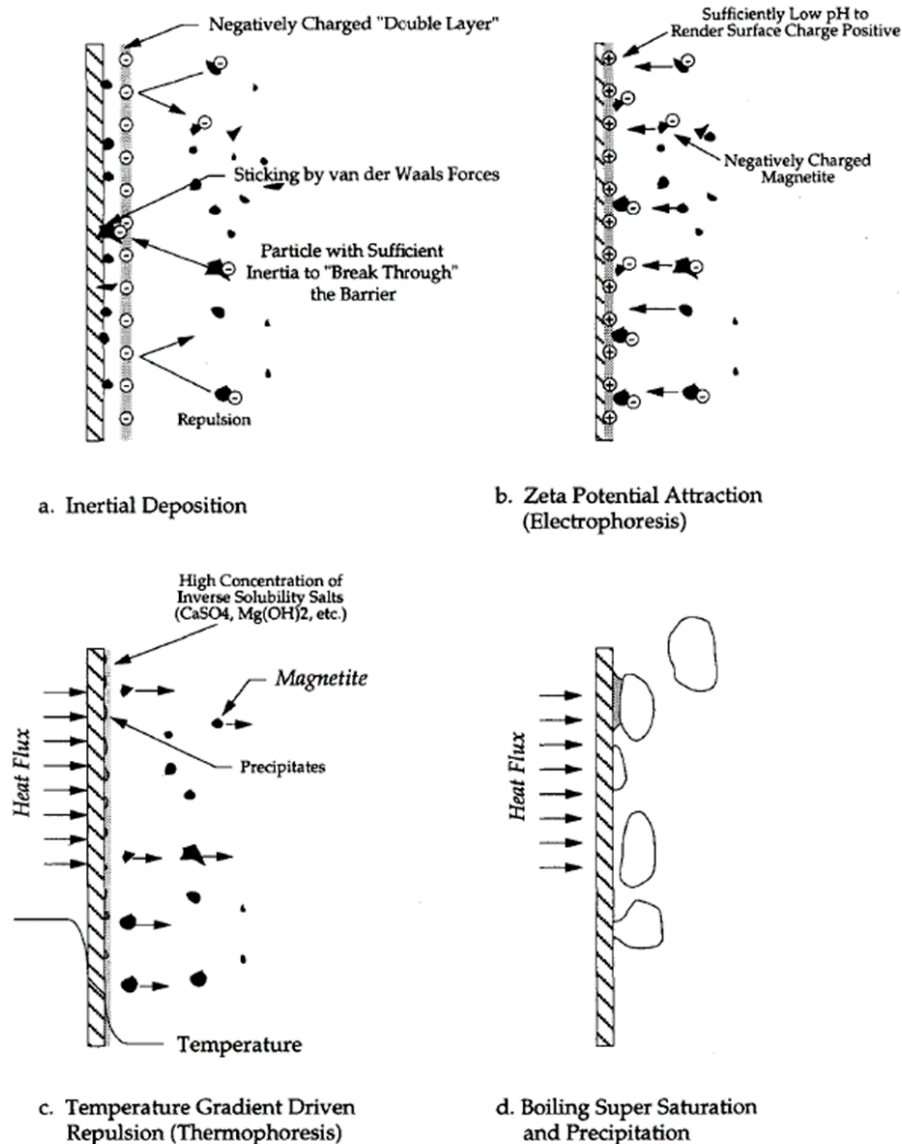
Fouling consists of three layers: a metal corrosion layer, an oxide layer, and a deposition layer. A metal corrosion layer forms on the bulk material, in which the elements diffuse and combine with oxygen. An oxide layer forms on top of the corrosion layer due to electrochemical reactions between the metal and the solution. The inner layer of the oxide layer is compact and is often thought to be part of the metal corrosion layer. The outer oxide



layer is loose. The third layer is formed by the deposition of non-volatile impurities in the circuit. (Xie and Zhang 2016)

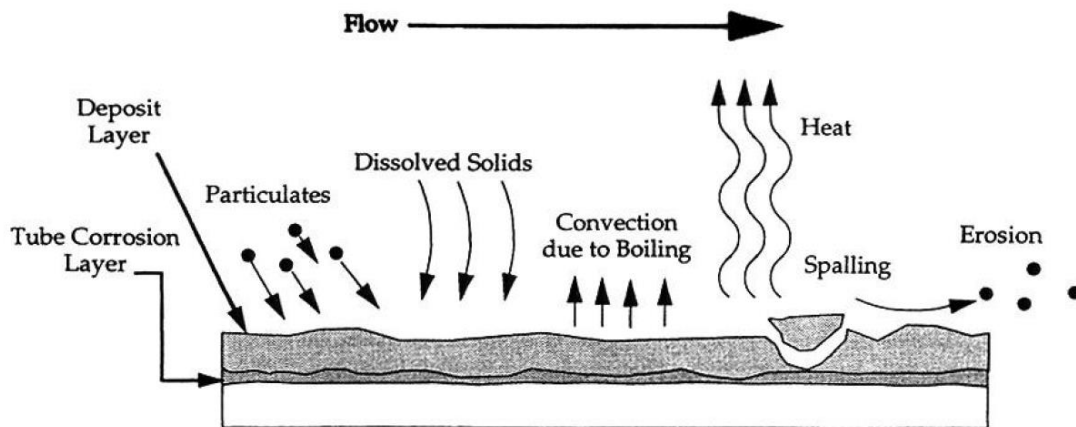
Whether fouling is a chemical or physical process (or both), it probably involves contributions from both processes. In the chemical process, oxides crystallize from solutions and in physical, particles attach to the surface. Chemical fouling is influenced by the precursor concentrations, the temperature, and the binding energies similarity between the resultant deposit and the surface. Influencing factors in the physical fouling are the particle size and concentration, the flow conditions, the temperature, the surface charges of the particles and the surfaces. Fouling occurs in several stages: incubation, initiation, growth, growth limiting stage, spalling and re-deposition. (Varrin 1996)

The fouling incubation phase takes place when the power plant is in a hot stand-by mode, with the aim of forming a protective passive film on the SG and pipe surfaces. There are several mechanisms for the initiation phase: inertial deposition, zeta potential attraction, thermophoresis and boiling supersaturation and precipitation. These deposition mechanisms are demonstrated in Figure 2.8. Among these mechanisms, inertial deposition and zeta potential deposition have the greatest influence on the precipitation of magnetite. (Melo et al. 1988) The effect of these two mechanisms is discussed in more detail in chapter 3.



**Figure 2.8.** Possible mechanisms of fouling initiation. (Varrin 1996)

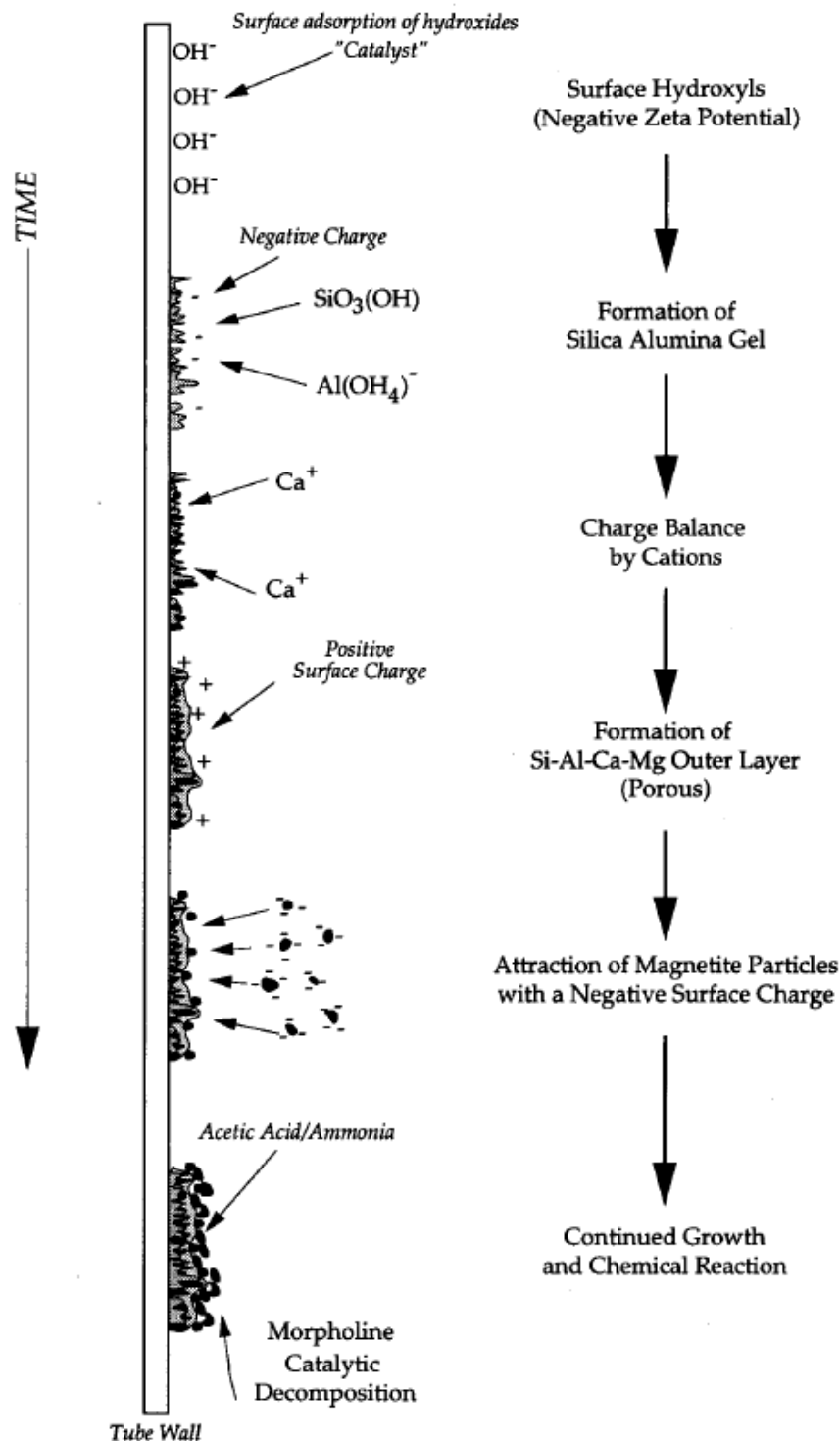
The remaining stages of fouling can be modelled with the Charlesworth model as in Figure 2.9. In this model, deposition involves physical and chemical phenomena, such as turbulent and boiling deposition, gravitational settling, and re-entrainment. During turbulent fluid motions, particulate species are transported and attached to the surface by the turbulence eddies. These species are either carried by feedwater flow or they grow from dissolved chemical precursors within the SG. Boiling deposition occurs due to evaporation of the water on the tube surfaces, which causes concentration and precipitation of the deposit precursors. In gravitational settling particles deposit on a horizontal surface due to the action of gravity. Re-entrainment liberates portions of existing deposits, and they might re-deposit. (Vepsäläinen 2010)



**Figure 2.9.** The Charlesworth fouling model. (Vepsäläinen 2010)

So-called chimneys and capillaries begin to form within the deposits by ripening or crystal growth. As a result, the feedwater is drawn into the deposit, carrying various chemical species. This kind of deposit build-up on the tube surface and in crevices at the intersections of the SG tube and tube-support plates (TSP) is known as “hideout”. (Green and Hetsroni 1995)

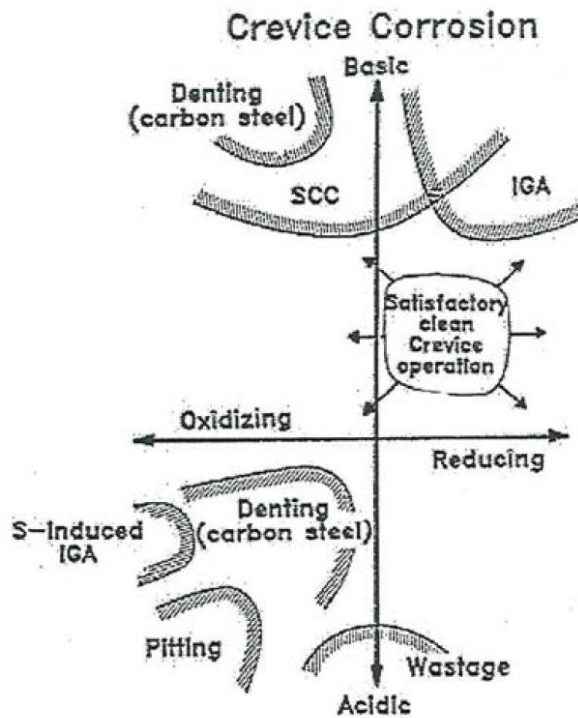
Hideout is driven by the evaporation of liquid within the pores of the deposit. With the cycle of fresh feedwater entering within the deposit and its evaporation, deposit grows as different compounds precipitate inside the deposits. Consolidation of the deposit is possible, if cementitious agents, such as silicates and aluminum, are carried with the fluid flow. The possible roles of silica ( $\text{SiO}_2$ ) and alumina ( $\gamma\text{-Al}_2\text{O}_3$ ) in magnetite deposition are presented in Figure 2.10. (Varrin 1996) Consolidation process is further explained in section 3.



**Figure 2.10.** Effect of silica ( $\text{SiO}_2$ ) and alumina ( $\gamma\text{-Al}_2\text{O}_3$ ) on the deposition and consolidation of magnetite. (Varrin 1996)

As impurities in the deposits increase and react with each other, the pH can become locally acidic or alkaline. This also affects the electrochemical potential (ECP) of the area. Extremely high or low local pH values can dissolve the oxide layers and accelerate different types of corrosion phenomena. Similarly, the local ECP affects strongly in the occurrence

and rate of the corrosion. (Odar and Nordmann 2010) Figure 2.11 illustrates different types of SG tube corrosion modes depending on the existing local chemistry conditions (pH and ECP).

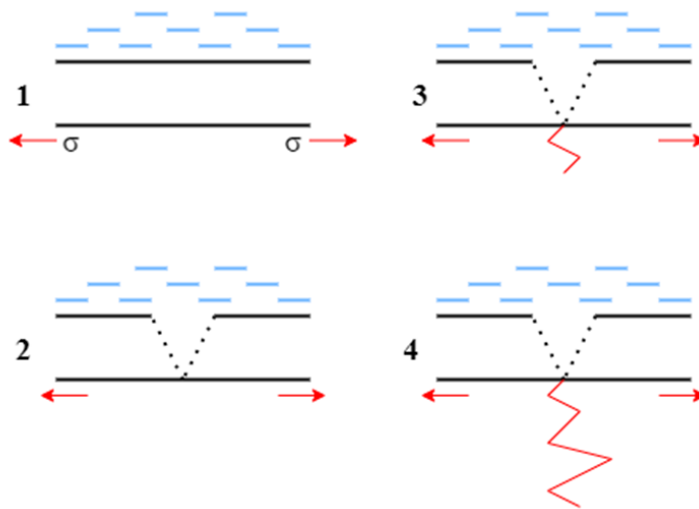


**Figure 2.11.** SG tube corrosion in dependence of environmental conditions. (Kang et al. 2011)

Mechanical or chemical damage to the passive film often leads to localized corrosion, such as pitting and crevice corrosion. If the film is not immediately re-passivated, the formed pit can grow and in worst case perforate the wall thickness. (WebCorr 2022)

The stress corrosion cracking (SCC) results from the conjoint action of the susceptible material, tensile stresses, and an aggressive environment containing corrosive impurities such as activators (usually chloride or sulphide ions) and oxidizers (oxygen and ions of trivalent iron). An aggressive environment can break the protective passive film locally, making the surface more susceptible to corrosion and enabling crack growth. For instance, for carbon steels, such an environment is near-neutral or weakly alkaline ( $\text{pH} < 11$ ). (Kang et al. 2011)

SCC process is divided into three stages: initiation, propagation, and failure. SCC typically initiates at pre-existing or corrosion-induced surface flaws. Surface discontinuity features may be caused by manufacturing (grooves, burrs) or created by corrosion processes (pits). (Khalifeh 2019) An example of the SCC process is presented in Figure 2.12 if it would initiate from a bottom of a corrosion pit.



**Figure 2.12.** Stages of the SCC process: **1)** The protective oxide layer breaks **2)** Formation of corrosion pit **3)** Initiation of SCC **4)** Propagation of SCC and possible failure. The arrows indicate the direction of applied stress,  $\sigma$ .

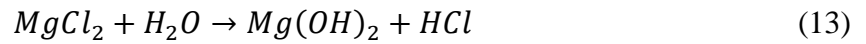
SCC propagation mechanisms can be classified in two models: dissolution based and mechanical fracture. Mechanical fracture is induced by interactions between the material and the environment such as adsorption of environmental species, surface reactions and surface films. (Jones 1992) Four major mechanisms are presented in Table 2.7, with two involving dissolution and two mechanical effects.

**Table 2.7.** Four major SCC mechanisms. (McCafferty)

| Classification     | Mechanism   |
|--------------------|---|
| Dissolution effect | <i>Anodic dissolution:</i> An active-path occurs as a result from a difference at the interface boundary, where compounds are formed<br><i>Film rupture:</i> Continuous re-passivation and film breakdown occurs in a cycle and continues until failure |
| Mechanical effect  | <i>Adsorption:</i> Specific chemical species adsorbs on the crack surface and lowers the fracture stress<br><i>Hydrogen embrittlement:</i> Hydrogen atoms are absorbed into the metal, embrittling it and eventually leading to metal fracture          |

Transgranular or intergranular stress corrosion cracking (TGSCC/IGSCC) of stainless steel can occur in SGs, if chloride concentration increases e.g. due to a condenser leak, which are typical for VVER plants. In a such situation, the hydrolysis of magnesium chloride ( $MgCl_2$ )

causes an acidic environment according to the reaction equation (13), because magnesium hydroxide, which has a very low solubility at high temperature, precipitates. (IAEA 2008)



All SG degradation problems, not only the corrosion but also the thermal efficiency issues, are related to the secondary side impurities and their deposition. These problems can be counteracted by keeping the SGs clean from corrosion products. (Odar and Nordmann 2010)

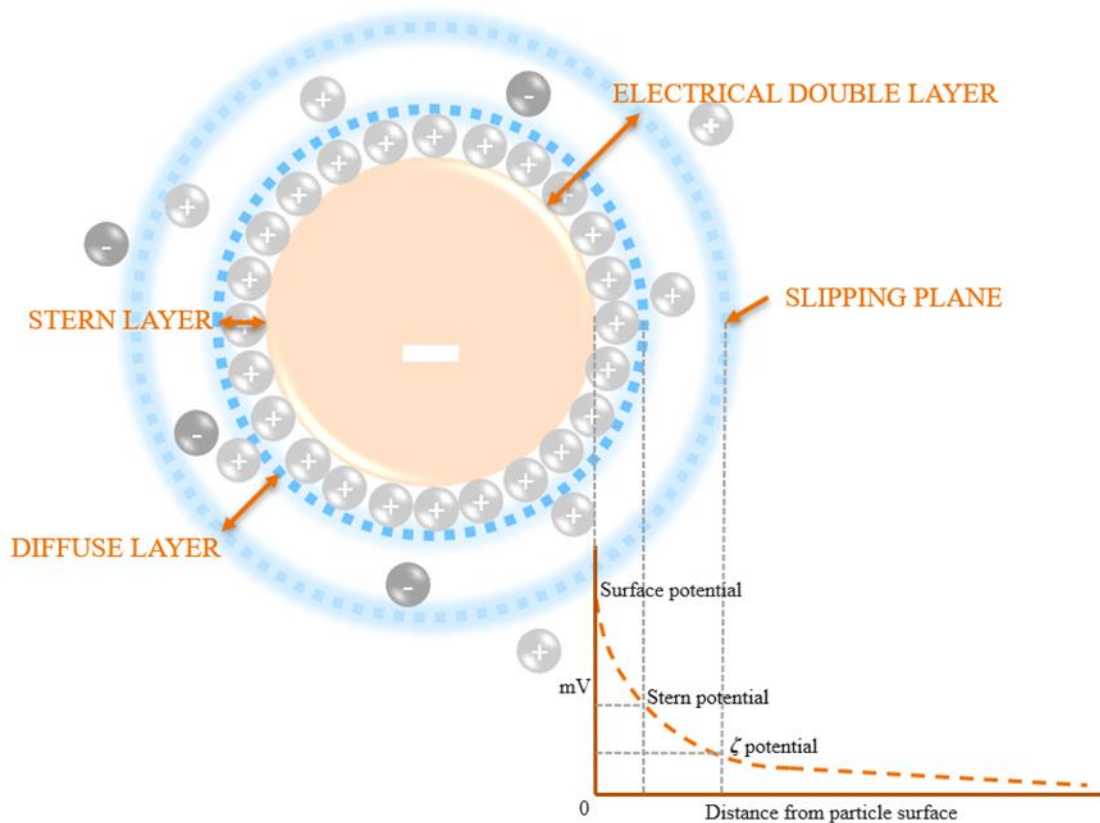
### **3 FACTORS AFFECTING MAGNETITE DEPOSITION AND FORMATION OF HARD DEPOSITS**

VTT has previously studied what affects the formation of deposits (Ikäläinen et al. 2020). It has been identified that different forces between particles and surfaces are involved, but the extent of their influence is still unclear.

The inertial deposition process can be understood from the surface forces between a colloidal particle and a wall. For simplification, the DLVO theory (named after Boris Derjaguin, Lev Landau, Evert Verwey and Theodoor Overbeek) is used, which only considers the London-van der Waals attraction and electrical double-layer repulsion. Van der Waals forces are weak forces between molecules due to either temporary or permanent dipoles that cause attraction between molecules. (Shaw 1992)

A double layer (DL), also called an electrical double layer (EDL), is a structure that appears on the surface of an object when it is exposed to a fluid. The EDL consists of surface charge on the particle, Stern layer, and a diffuse layer. This structure is presented in Figure 3.1. Usually, the charged ions on the surface of the particle are negative and ions in Stern layer are charged opposite to the surface and are attracted and attached to it. Diffuse layer contains free ions with a higher concentration of the counterions. The ions of the diffuse layer are affected by the electrostatic force of the charged particle. (Murtomäki et al. 2019)



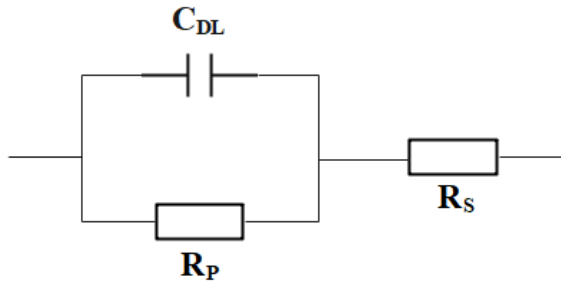


**Figure 3.1.** Electrical double layer and potential difference as a function of distance to charged particle surface.

The effect of zeta ( $\zeta$ ) potential on the deposition of magnetite in steam generators has already been researched at VTT (Ikäläinen et al. 2020). Zeta potential is the electrical potential in EDL at the slipping plane as seen in Figure 3.1. The zeta potential is used to as an indicator of the stability of the colloidal system. Particles in solution with high absolute  $\zeta$ -potential tend to repel each other, and the particles cannot merge. At the isoelectric point or point of zero charge (PZC), the zeta potential changes from negative to positive at a specific pH value ( $\text{pH}_{\text{IEP}}$ ). At this point the suspension has the lowest stability and has a high potential for aggregation and precipitation. Particles can also attract and deposit on the surface when the colloidal particles and the surface are oppositely charged. (Vidojkovic et al. 2011)

EDL is the origin of the potential difference across the interface, and the electrode potential. Corroding metal ions pass across the EDL to the solution and solution species enter the EDL to attack the metal surface and cause corrosion. EDL can be modeled with simple equivalent circuit as in Figure 3.2, which comprises of a double layer capacitance  $C_{\text{DL}}$  in parallel with a Faradaic resistance  $R_{\text{P}}$ , and a solution resistance  $R_{\text{S}}$  is in series with them. The resistance

in parallel with the capacitance, demonstrates opposition to charge transfer in EDL. (McCafferty 2010)



**Figure 3.2.** Simple equivalent circuit of EDL.

Slipping plane separates the fixed and mobile parts of the EDL. It is assumed that the slipping plane is close to the Stern plane, making the Stern layer the fixed part and all the diffuse layer mobile. Electrokinetic phenomena (EKP) are related to this mobile part and may be interpreted only in terms of the zeta potential or the charge density at the slipping plane. (Shaw 1992) There are several electrokinetic phenomena, but typically only four phenomena are used to study the electrical properties of the interface. These are electrophoresis, electro-osmosis, streaming potential, and sedimentation potential. Phenomena are based upon the charge difference between the diffusion layer and the solid surface. (Elimelech 2010) The most common EKPs are tabulated in Table 3.1.

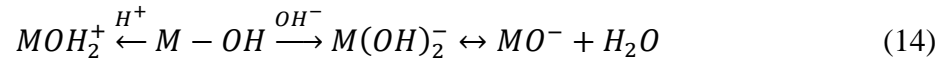
**Table 3.1.** Electrokinetic phenomena. (Lyklema 1995)

| Phenomena               | Driving force     | Moving phase | Result               |
|-------------------------|-------------------|--------------|----------------------|
| Electrophoresis         | Electric field    | Particles    | Particle translation |
| Electro-osmosis         | Electric field    | Liquid       | Liquid displacement  |
| Streaming potential     | Pressure gradient | Liquid       | Potential difference |
| Sedimentation potential | Gravity           | Particles    | Electric field       |

Electrophoresis, also known as zeta potential attraction and repulsion, is only considered because it is assumed to affect to the deposition of magnetite. In this model, particles in SG feedwater develop surface charges, when the particle is covered by an ionic layer. Surface charge can be obtained in three ways: ionization, adsorption, and hydration. This formed layer attracts oppositely charged ionic species to achieve electrical neutrality. (Hunter 1981)

During ionization, the surface groups of the particle dissociate. A positively charged surface is caused if the groups are alkaline, while a negative surface is caused by dissociation of

acidic groups. Dissociations can be regarded as adsorption reactions, and they might lead to hydration. Surface charge of a metal oxide (M) develops in aqueous solutions, when the surface is hydrated, and the surface hydroxyl groups dissociate as demonstrated in equation (14). (Burrill 1977)



Zeta-potential deposition consists of two stages. First, the particle is transported close to the surface by inertial forces, eddies, turbulence, or diffusion. Then it attaches to the surface by electrostatic forces followed by adhesion. Adhesion may occur as Van der Waals attraction or if the particle can overcome repulsive electrostatic forces. Magnetite deposition is attachment limited, because the surface and the particle are similarly charged and only fraction of the particles actually attach the surface. (Varrin 1996)

Deposition consolidation, also known as hardening, is a process in which the deposit chemically bonds to a heat transfer surface or to an existing deposit, thus preventing the deposit from being removed by the fluid. The mechanisms of hardening are Ostwald ripening, dissolution and re-precipitation of corrosion products, and boiling-induced precipitation of dissolved species. (EPRI 2002)

The smaller particles or crystals dissolve and re-precipitate on the surface of the larger particles in the Ostwald ripening process. Dissolution and re-precipitation, leading to deposit hardening, is enhanced in the temperature gradient. In temperature gradient, the material shifts from a higher solubility region to a lower solubility region, reducing porosity and increasing the strength of the deposit. A third proposed mechanism for consolidation is boiling-induced precipitation in hideouts. As water evaporates from the heat transfer surface through the pores of the deposit, residues of dissolved species and very small particles remain, acting as cement for larger particles. (Odar and Nordmann 2010) These cementing species include not only alumina and silica, but also hardness species such as calcium and magnesium. The hardness species occur either as ions ( $Ca^{2+}$ ,  $Mg^{2+}$ ) or as compounds ( $CaSO_4$ ,  $MgSO_4$ ). These species can further combine to form a zeolite-like compounds in deposits. (Varrin 1996)

## **4 RESEARCH METHODS**

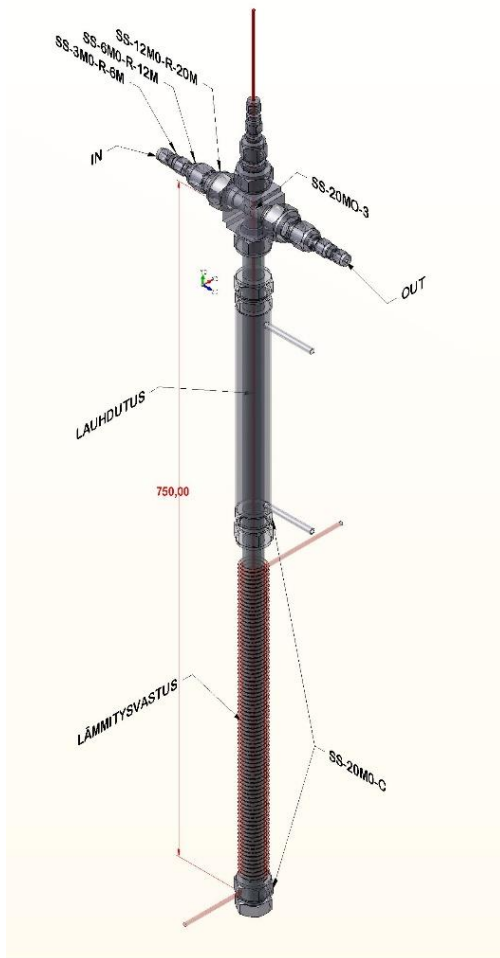
Two experimental setups were developed for the studies related to magnetite precipitation and hardening in secondary circuit of nuclear power plants.

### **4.1 High-pressure and temperature magnetite cell**

This experimental setup was developed for studying the factors influencing the deposition and hardening of magnetite on the metal surface under secondary circuit conditions.

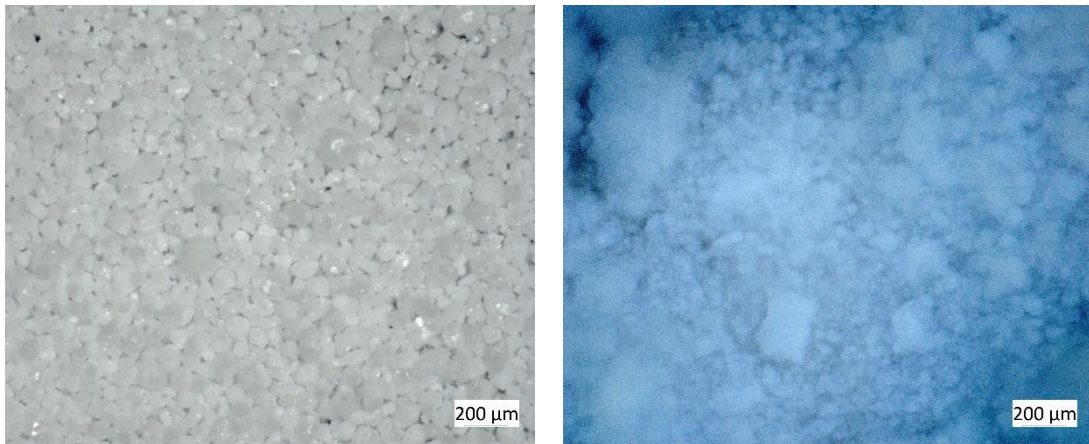
This experimental system consists of a straight pipe, a heating resistor wrapped around the pipe, a cooling system and temperature monitoring. The pipe is made of stainless steel (AISI 316L) with an outer diameter of 20 mm and a wall thickness of 2 mm. A schematic description of the experimental system is shown in Figure 4.1. Magnetite powder is inserted, and alumina and silica dissolved in water are fed into the system. Before adding ammonia, the system is nitrogen bubbled for 10 minutes to remove oxygen. Ammonia is added so that the theoretical pH is 9,6 and hydrazine is used for as a precaution to remove the residual oxygen. The system is heated and boiling initiates at the bottom of the pipe. The water vapor rises upwards and condenses at the top on the cooling side. The duration of a single experiment is three weeks.

In the first six experiments the water temperature was set at 250 °C and in the last two at 275 °C. Before starting each experiment, each pipe was pressure tested. By performing this test, it was determined that maintaining the water temperature at 250 °C required 30% of the power of the heating resistor and at 275 °C required 35%. The heating resistor has a maximum power capacity of 1 kW.



**Figure 4.1.** Experimental setup – High-temperature and high-pressure magnetite cell.

The substances used in the experiments were magnetite, silica, and  $\gamma$ -alumina. The magnetite powder with high purity (99,9%) and a maximum particle size of 50 micron is provided by Goodfellow<sup>®</sup>, and silica and  $\gamma$ -alumina are from Merck<sup>®</sup>. The particle size of the alumina or silica was determined by microscope. The particle size of the alumina and silica was determined by microscope. The particle size of alumina ranged from a few microns to several hundred microns. However, the silica was too amorphous to provide exact particle size. Magnifications of alumina and silica powders taken with the Zeiss Axio Zoom V16 microscope are presented in Figure 4.2.



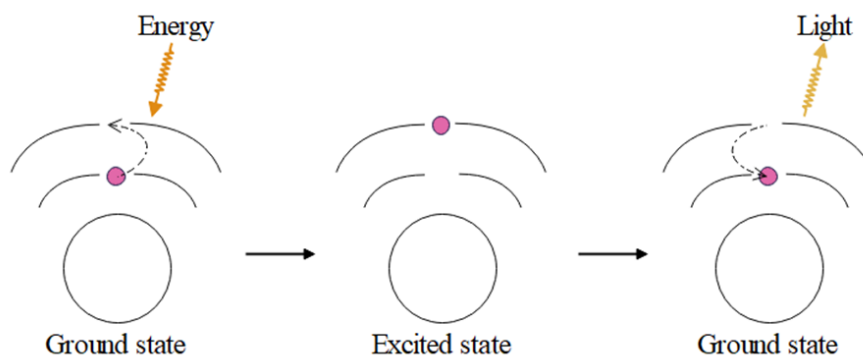
**Figure 4.2.** Microscopic 56X magnifications of alumina (left) and silica (right) powders.

For two experiments, magnetite powder from the Loviisa NPP was used instead of the commercial magnetite. The substances and their quantities used in the experiments are given in Table 4.1. The cells in the table are shaded grey, where Loviisa magnetite was utilized.

**Table 4.1.** The chemicals applied in each pipe cell experiment.

|                                      | 1     | 2     | 3     | 4     | 5     | 6     | 7     | 8     |
|--------------------------------------|-------|-------|-------|-------|-------|-------|-------|-------|
| Fe <sub>3</sub> O <sub>4</sub> [g]   | 0,800 | 0,801 | 0,801 | 0,807 | 0,819 |       | 0,808 | 0,805 |
| NH <sub>3</sub> [μl]                 | 2,1   | 2,1   | 2,1   | 2,1   | 2,1   | 2,1   | 2,1   | 2,1   |
| N <sub>2</sub> H <sub>4</sub> [μl]   | 15,4  | 15,4  | 15,4  | 15,4  | 15,4  | 15,4  | 15,4  | 15,4  |
| SiO <sub>2</sub> [g]                 |       | 0,176 | 0,176 |       | 0,176 | 0,462 | 0,176 | 0,176 |
| γ-Al <sub>2</sub> O <sub>3</sub> [g] |       | 0,312 |       | 0,313 | 0,314 | 0,834 | 0,314 | 0,317 |

The elemental content of magnetite powder from the Loviisa NPP was determined by Inductively Coupled Plasma-Optical Emission Spectrometry (ICP-OES). The principle of ICP-OES is based on the absorption of energy by an atom or ion to transfer electrons from the ground state to the excited state, so that excited atoms or ions release light at certain wavelengths as their electrons move back to lower energy level. The wavelength of the emitted light indicates what kind of element it is. (Agilent 2022) The principle of ICP-OES is demonstrated in Figure 4.3.



**Figure 4.3.** An atom occupying absorbed energy to boost its electron to an orbital with a higher energy, and it returning to its ground state while emitting a photon. (NASA 2013)

Three samples were dissolved in concentrated acid solutions (HNO<sub>3</sub>, HCl and HF) at different dilutions (1/2, 1/10 and 1/100). Multisubstrate standards by Inorganic Ventures and SPEX, were used as calibration and measurement controls. The average elemental concentrations of the magnetite powder are calculated from the measured elemental concentrations and known dilution factors of the sample solutions. Table 4.2 shows the average elemental concentrations of magnetite powder from Loviisa NPP.

**Table 4.2.** Average elemental concentrations [mg/kg] of magnetite powder from Loviisa NPP.

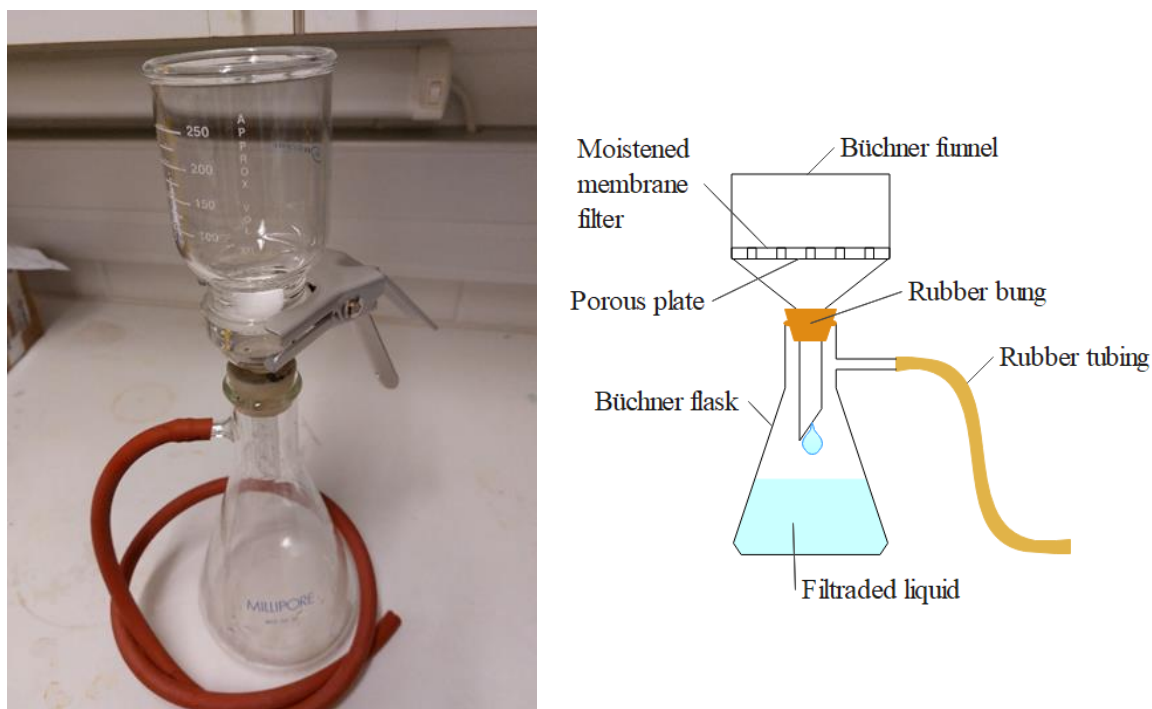
|           |           |           |           |           |           |           |           |           |           |           |
|-----------|-----------|-----------|-----------|-----------|-----------|-----------|-----------|-----------|-----------|-----------|
| <b>Ag</b> | <b>Al</b> | <b>B</b>  | <b>Ba</b> | <b>Ca</b> | <b>Cd</b> | <b>Co</b> | <b>Cr</b> | <b>Cu</b> | <b>Fe</b> | <b>K</b>  |
| 2,55      | 628       | 612       | 0,617     | 5,62      | 2,40      | 106       | 844       | 2948      | 812812    | 6,04      |
| <b>Li</b> | <b>Mg</b> | <b>Mn</b> | <b>Mo</b> | <b>Na</b> | <b>Nb</b> | <b>Ni</b> | <b>P</b>  | <b>Pb</b> | <b>Re</b> | <b>S</b>  |
| 0,541     | 74,0      | 5004      | 73,4      | 43,4      | 0,01      | 1342      | 116       | 273       | 75,5      | 71,9      |
| <b>Sb</b> | <b>Si</b> | <b>Sn</b> | <b>Sr</b> | <b>Ta</b> | <b>Ti</b> | <b>U</b>  | <b>V</b>  | <b>W</b>  | <b>Zn</b> | <b>Zr</b> |
| 45,7      | 187,1     | 0,113     | 0,011     | 0,098     | 0,310     | 0,538     | 0,053     | 0,069     | 1,31      | 0,108     |

Magnetite powder contains several different elements, including silver (Ag), aluminum (Al), cobalt (Co), chromium (Cr), copper (Cu), iron (Fe), magnesium (Mg), titanium (Ti) and uranium (U). The elements in the magnetite powder indicate that the plant has had leaks between circuits and in the condenser. Also, substances dissolved by FAC from tube materials can be identified. The substances of most interest in terms of magnetite deposit hardening are magnesium, calcium, alumina, and silica.

When the experiment is finished, the equipment is switched off and left to cool down for about an hour to be able to disassemble the setup. A beaker is placed under the pipe so that all the liquid and loose material escaping from it can be recovered when the pipe is opened.

The pH of the mixture collected in the beaker is measured. The pH meter is calibrated using buffer solutions with pH 7 and 10, since the theoretical pH of the pipe experiments was 9,6.

Magnetite, alumina, and silica can be separated from the recovered liquid by suction filtration. Equipment for suction filtration presented in Figure 4.4 include a Büchner funnel, a suction bottle, a porous plate, and the membrane filter. The membrane filter with a 47 mm diameter and 0,47  $\mu\text{m}$  pore size is placed on a petri dish and dried in an oven. The combined mass of the dry filter and dish is weighed. Once the device is assembled, the mixture can be poured into the funnel, whereby water is absorbed through the membrane filter and the porous plate into the bottle by vacuum suction and the magnetite and other chemicals remains on top of the filter. The membrane filter with the filtration is transferred to a petri dish and oven for drying to obtain the dry mass of the magnetite. The mass difference indicates how much material is in the filter and how much is left on the inner surfaces of the pipe. An overview and pre-defined magnifications of the filtrations were taken with a Zeiss Axio Zoom V16 microscope.



**Figure 4.4.** Suction filtration equipment.

Once the pipe is dry, it is sawed in half vertically to allow visual inspection of the inner surface of the pipe and to select the four most interesting looking sections for SEM imaging from different regions of the pipe cell. The pictures of the inner surfaces of the pipes are in Appendix I .



#### 4.1.1 Heat transfer calculation

During the experiments, measurement data is acquired from the temperature of the pipe surface, the pressure and temperature of the water vapor and the temperature of the condensate. The temperature of the surrounding environment of the experimental setup was also measured throughout the duration of the experiments.

The temperature of the outer surface of the pipe was measured at two different points under the resistor and the water vapor temperature measurement is located approximately halfway between these two points inside the pipe. The average of the outer surface temperatures is obtained in order to compare the temperature of the pipe surface with the temperature of the water vapor in the pipe.

Conduction occurs through the medium and whereas convection is caused by temperature differences between the surface and the moving fluid. (Bergman and Incropera 2011) Thus, according to these two mechanisms of heat transfer, heat is conducted in the pipe wall and the surrounding insulation, whilst heat is conveyed from the surfaces to water or air.

The heat transfer rate may be expressed as the ratio of the overall temperature difference  $\Delta T$  [°C] to the total thermal resistance  $R_{tot}$  [°C/W] as in equation (15). Depending on the nature of the heat transfer, it can be represented either as conduction in hollow cylinder in equation (16) or convection in equation (17), or as their sum in equation (18) by applying equations (15), (16) and (17) (Bergman and Incropera 2011):

$$q = \frac{\Delta T}{R_{tot}} \rightarrow R_{tot} = \frac{\Delta T}{q} \quad (15)$$

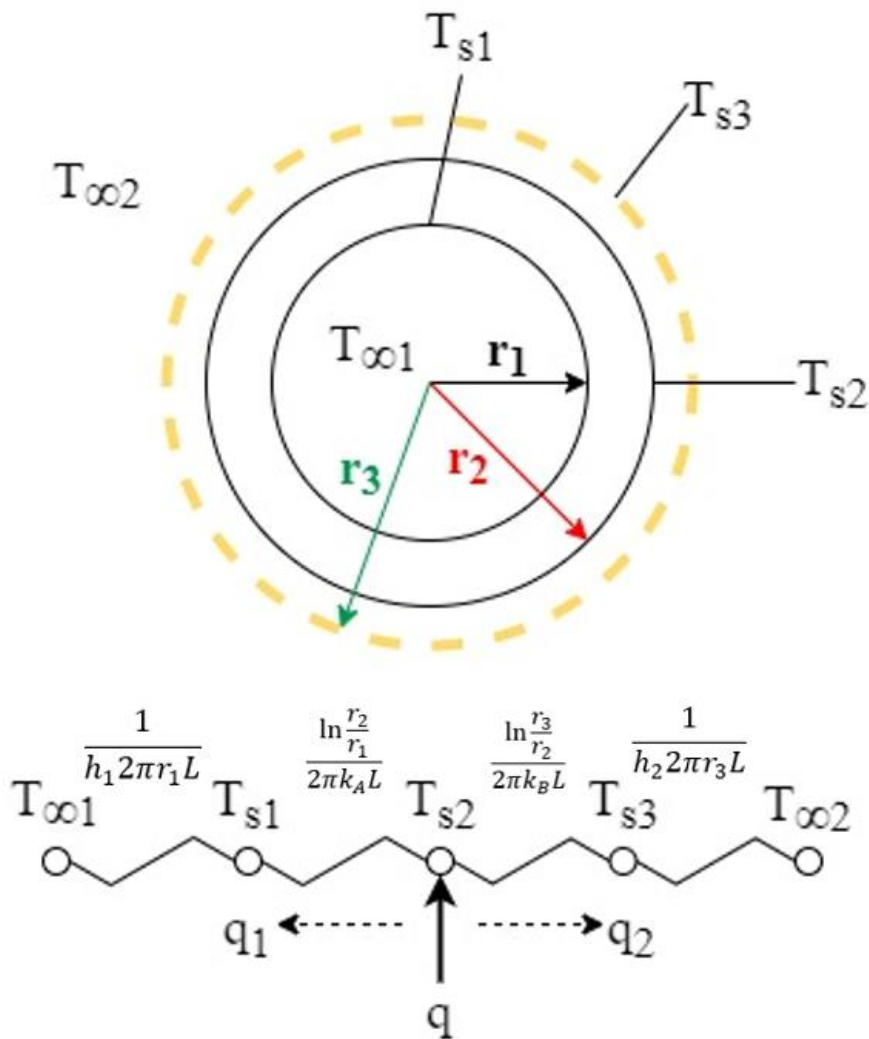
$$q = \frac{2k\pi L\Delta T}{\ln \frac{r_o}{r_i}} \quad (16)$$

$$q = hA\Delta T \quad (17)$$

$$q = \frac{\Delta T}{\frac{\ln \frac{r_o}{r_i}}{2\pi kL} + \frac{1}{2\pi r_x hL}} \quad (18)$$

where  $q$  is heat rate of the resistor around the pipe [W],  $r$  is radius [m],  $k$  is thermal conductivity [W/m°C],  $h$  is convective heat transfer coefficient [W/m<sup>2</sup>°C] and  $L$  is length of the pipe [m].

Heat transfer can be modelled using an equivalent thermal circuit, which makes it easier to understand and quantify the phases of heat transfer. (Bergman and Incropera 2011) The thermal circuit of the experimental setup is given in Figure 4.5, with the different thermal resistances of the phases.



**Figure 4.5.** Heat transfer through the experimental setup and the thermal circuit of the setup, where  $T_{\infty 1}$  is the temperature of the water vapor [ $^{\circ}\text{C}$ ],  $T_{s1}$  is the temperature of the inner pipe surface [ $^{\circ}\text{C}$ ],  $T_{s2}$  is the average temperature of outer pipe surface [ $^{\circ}\text{C}$ ],  $T_{s3}$  is the temperature of insulation surface [ $^{\circ}\text{C}$ ] and  $T_{\infty 2}$  is the temperature of the environment [ $^{\circ}\text{C}$ ].

The convective heat transfer coefficient  $h_2$  from the insulation to the air was estimated using the heat transfer coefficient software for natural convection, by assuming a maximum insulation surface temperature of  $50^{\circ}\text{C}$ . Typical thermal conductivity values are used for 316L stainless steel  $k_A$  and mineral wool insulation  $k_B$ . Table 4.3 contains the dimensions of the magnetite pipe cell experiment and the values needed to determine the heat transfer.

**Table 4.3.** Geometry of the magnetite pipe cell experiment and heat transfer constants.

| $L$ [m] | $r_1$ [m] | $r_2$ [m] | $r_3$ [m] | $q$ [W]   | $h_2$ [W/m <sup>2</sup> °C] | $k_A$ [W/m°C] | $k_B$ [W/m°C] |
|---------|-----------|-----------|-----------|-----------|-----------------------------|---------------|---------------|
| 0,4     | 0,008     | 0,01      | 0,05      | 300 / 350 | 5                           | 15            | 0,05          |

The water vapor  $T_{\infty 1}$ , pipe surface  $T_{s2}$  and environment  $T_{\infty 2}$  temperatures are obtained from the measurement data. When the heating resistor is on, its heat is distributed towards the pipe and the insulation as shown in Figure 4.5. Since the convective heat transfer coefficient of water vapor is not known, the heat transfer is first determined from the surface of the pipe towards the environment with equation (18).

The energy balance of the heating resistor in equation (19) is the basis for determining the heat rates  $q_1$  and  $q_2$  towards the pipe and insulation. Following this, equation (18) can be reapplied to determine the temperature of the inner surface of the pipe and the outer surface of the insulation. However, when determining heat transfer through a surface, one must consider which thermal resistances to utilize.

$$q = q_1 + q_2 \quad (19)$$

All the collected data from the experiments is analysed by Microsoft office Excel spreadsheet and heat transfer charts are created from the data.

#### 4.1.2 Ex-situ characterization with scanning electron microscope

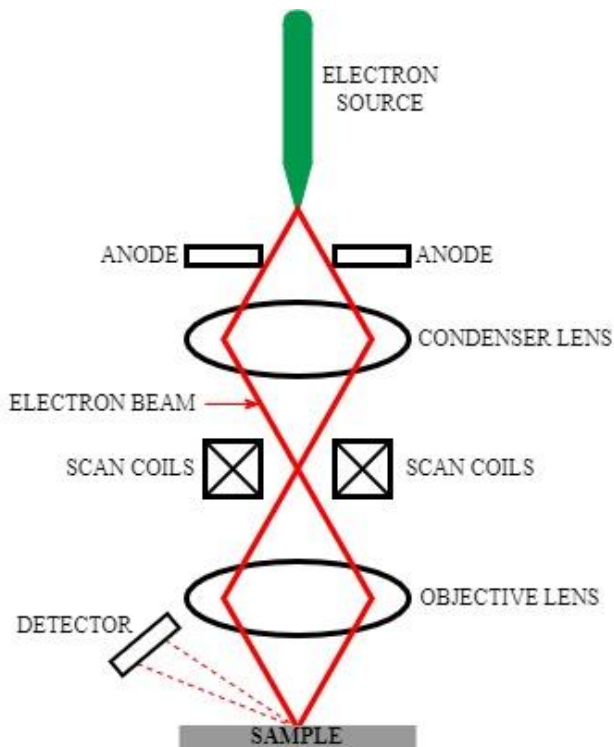
The scanning electron microscope (SEM) uses a focused beam of high-energy electrons to generate images of the solid sample. The signals deriving from the sample reveal information about the sample's topography and chemical composition. These signals typically consist of secondary electrons (SE), reflected or back-scattered electrons (BSE) and X-rays. (Nanakoudis 2019)

SE are used to form an image of the surface of a sample and to view its topography. Image magnification from 20x to 2 000 000x and resolution up to 1 nm are possible with SE analysis. BSE provides information on the elemental distribution of a sample when electrons are scattered differently from elements of different masses. This can be seen in the image as contrast differences, meaning that the brighter BSE intensity correlates with a higher average atomic number  $Z$  in the sample, and the average  $Z$  is lower in the darker regions. (Top Analytica Oy Ab 2021)

The imaging process also generates X-rays, enabling the analysis of elemental concentrations in the sample using energy dispersive spectrometry (EDS). The EDS analyzer provides an X-ray spectrum of either selected points in the image or the entire image area. EDS can detect major and minor elements from the sample. Major element concentration is higher than 10 wt% and minor concentrations are between 1 and 10 wt%. Element is not detected, if its concentration is below 0,1 wt%. The EDS spectrum is presented with X-ray counts as function of energy [keV]. Energy peaks correspond to the various elements in the sample, but many elements yield multiple peaks, and these peaks can be close to a peak of another element. For example, iron commonly shows strong  $K_{\alpha}$  and  $K_{\beta}$  peaks. (Makhlouf and Aliofkhazraei 2016)

EDS can also be used to generate an elemental map. Unlike BSE images, which only show average  $Z$  in contrast, element maps show the spatial distribution of each element of interest. Elemental maps are often colored to make it easier to detect subtle variations in the elements. SEM-EDS is a good method to analyze elements related to corrosion. (Top Analytica Oy Ab 2021)

Essential components for SEM are electron source (“gun”), lenses, different detectors for all signals of interest and display devices. It also requires power supply, vacuum and cooling systems, and a room free of ambient magnetic and electric fields. (Swapp 2017) A schematic diagram of SEM’s operation is shown in Figure 4.6.



**Figure 4.6.** A schematic diagram of scanning electron microscope.

SEM samples can be about 5 cm long and 1 cm high to fit on the sample stage. Samples must be conductive at the surface and withstand the vacuum conditions and the energy of the SEM gun. A thin film of a conductive material such as gold, carbon or platinum is sputtered onto the surface of the non-conductive samples. Powdery samples can also be imaged by SEM when cast on a button using either a conductive SEM resin or epoxy resin as seen in Figure 4.7. The button surface to be imaged is ground and polished ultra-smooth. The surface of the epoxy button is sputtered to enable SEM imaging. (Thermo Fisher 2022)



**Figure 4.7.** Magnetite powder from the Loviisa NPP cast in conductive SEM resin (left) and epoxy resin (right).

For this thesis, the Zeiss Merlin scanning electron microscope is used to acquire images of the samples from the pipe cell experiments. An accelerating voltage of 20 kV is used for the electron beam and the SE detector is used for the imaging at different magnifications.

Once a good quality desired magnification of the sample has been obtained by SEM, the elemental spectrum or map of the area in question can be obtained by x-ray acquisition and analysis software Pathfinder. An electron image of the current microscope location on the sample is acquired from SEM using the software. Since the image can shift during the acquisition process due to the movement of the stage, drift compensation is applied with an automatic interval. Spectral imaging (SI) mode is used to acquire elemental maps of the imaged area. While defining the SI settings, a few aspects should be considered before acquiring the data: map resolution, energy range and termination. The resolution of the map affects the acquisition time, and due to the high number of samples, it is desirable to keep the acquisition time reasonable. Noise peak can be eliminated from the low energy region and lighter species are easier to detect when the energy range is set. The acquisition is terminated, when the average total X-ray counts in a pixel for all maps reaches the set value of 100. The features of the image and the SI acquisition affecting the elemental map are given in Table 4.4.

**Table 4.4.** Settings for electron image and elemental map acquisition.

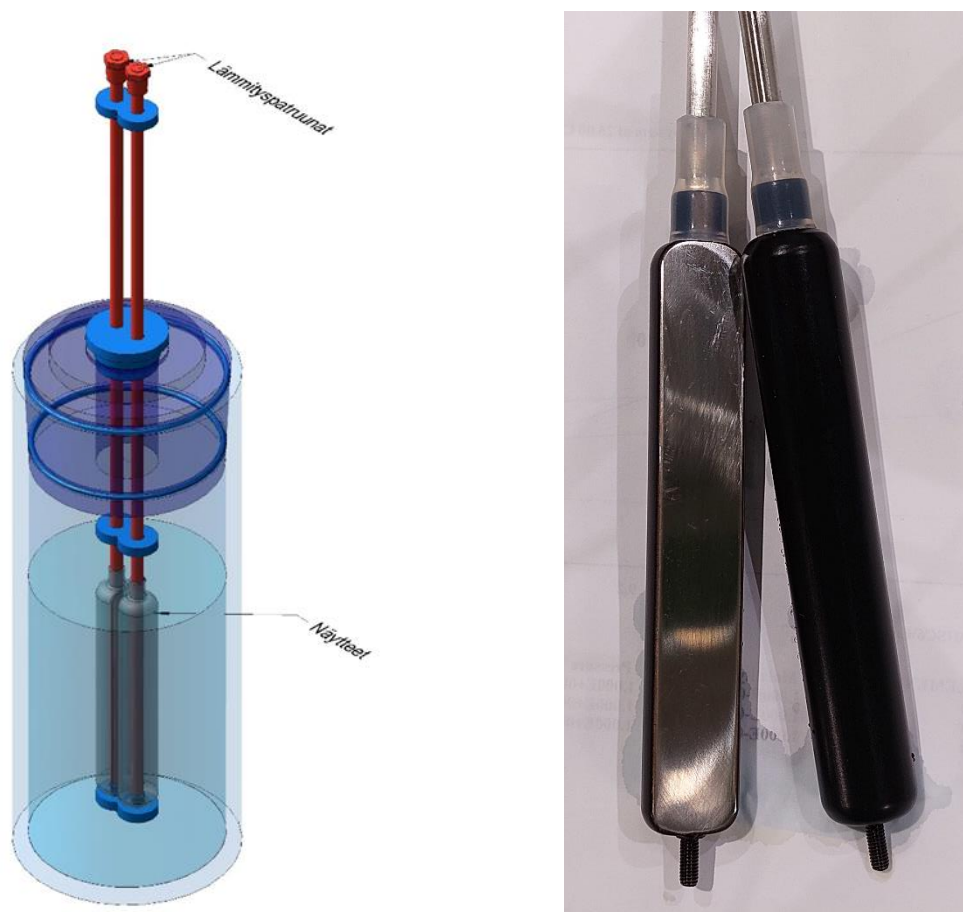
| Feature                  | Image     | SI       |
|--------------------------|-----------|----------|
| Resolution [-]           | 2048×1536 | 512×384  |
| Frame time [s]           | 10        | 10       |
| Number of frames [-]     | 2         | Infinite |
| Low energy cutoff [eV]   |           | 150      |
| High energy cutoff [keV] |           | 20       |

## 4.2 Experimental setup for in-situ monitoring of deposit formation

This experimental setup was developed for the visual monitoring of deposit formation. The experiments conducted with this setup were significantly faster compared to those with the pipe cell.

Two Inconel heating resistors are placed inside PFA-coated stainless steel (AISI 316) metal blocks and placed side by side so that the opposite inner surfaces are grinded clean and smooth with waterproof sandpaper of 1200 grit and 15  $\mu\text{m}$  grain size. The purpose of the PFA coating is to protect the outer surface so that the precipitation only occurs on the unprotected inner surface and limit the surface area of the electrodes used in EIS measurement. The metal blocks are placed in an airtight glass jar with 2,2 litres of water and

the desired water chemistry. This test system is shown in Figure 4.8. The resistors are switched on and the impedance response of the system is recorded in function of time during non-boiling and boiling conditions.



**Figure 4.8.** Experimental setup – In-situ monitoring of deposit formation.

A magnetic stirrer and a gas line for nitrogen bubbling are also installed inside the glass jar to mix the chemicals in the water efficiently and remove the oxygen. The mentioned setup is placed in a larger water container with continuous water flow in order to provide cooling for the system. The mentioned setup is placed in a larger water container with a continuous water flow in order to provide cooling for the system.

Table 4.5 contains data from all the experiments conducted on this experimental setup. It shows the different chemical species applied in each experiment, their quantities, and the water temperature at the start of the experiment. The power of the heating resistors was adjusted by relative power control, where the percentage in the table indicates the proportion of maximum power. A setpoint of 90 °C was set for the water in the glass jar, so that the

heating resistors regulate their own power output to maintain the water temperature constant when it reaches the set value.

**Table 4.5.** Experiment data.

| No. | Chemical                       | [g] | Power [%] | Water [°C] | Repetitions |
|-----|--------------------------------|-----|-----------|------------|-------------|
| 1   | CaSO <sub>4</sub>              | 5,5 | 60        | 60         | 19/100      |
| 2   | -                              | -   | 60        | 60         | 2/2         |
| 3   | CaSO <sub>4</sub>              | 4,5 | 50        | 60         | 87/100      |
| 4   | -                              | -   | 15        | 50         | 2/2         |
| 5   | -                              | -   | 50        | 60         | 2/2         |
| 6   | CaSO <sub>4</sub>              | 10  | 15        | 50         | 2/2         |
| 7   | CaSO <sub>4</sub>              | 10  | 40        | 60         | 15/100      |
| 8   | CaSO <sub>4</sub>              | 10  | 20        | 50         | 2/2         |
| 9   | CaCO <sub>3</sub>              | 0,7 | 20        | 50         | 2/2         |
| 10  | CaCO <sub>3</sub>              | 0,7 | 40        | 70         | 17/100      |
| 11  | CaCO <sub>3</sub>              | 0,7 | 25        | 50         | 1           |
| 12  | CaSO <sub>4</sub>              | 10  | 20        | 70         | 1           |
| 13  | CaSO <sub>4</sub>              | 10  | 50        | 90         | 117/120     |
| 14  | Fe <sub>3</sub> O <sub>4</sub> | 2   | 50        | 90         | 13/120      |

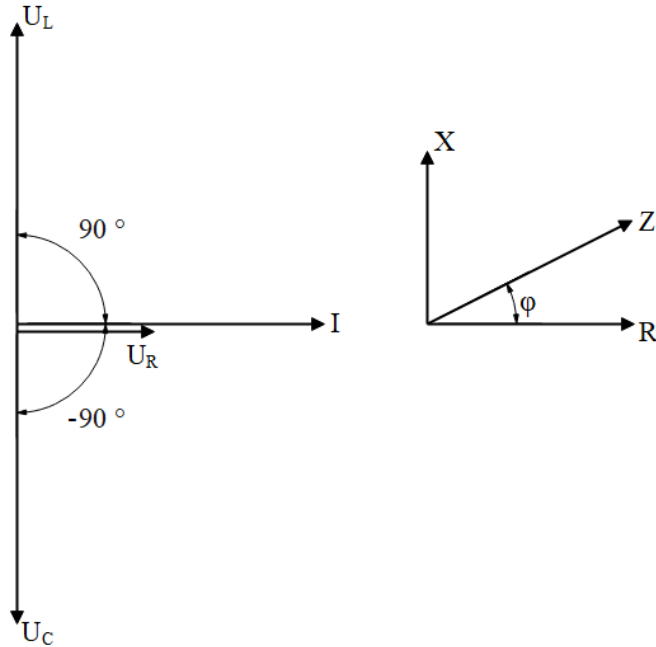
#### 4.2.1 Electrochemical Impedance Spectroscopy

Electrochemical impedance spectroscopy (EIS) is an electrochemical measurement technique. In EIS a small sinusoidal alternating current or potential perturbation is applied at a pre-determined frequency range and the resulting impedance response is recorded. The results obtained in EIS enables determining detailed information on the electrochemical processes of the studied electrochemical system.

Since current  $I$  and voltage  $U$  have a phase angle  $\varphi$  in an AC circuit, they are represented by complex numbers. Thus, their ratio, the impedance  $Z$ , is also a complex number, i.e. the impedance has a real part resistance  $R$ , and an imaginary part reactance  $X$ . Reactance is the opposition to alternating current by inductance  $L$  or capacitance  $C$ . Reactance can be either inductive  $X_L$  (positive) or capacitive  $X_C$  (negative). (McCafferty 2010) Figure 4.9 shows a phasor diagram of inductive, capacitive, and resistive voltage ( $U_L$ ,  $U_C$ ,  $U_R$ ) with respect to current  $I$ . The adjacent complex plane, known as the impedance triangle, shows the relation



of the resistance  $R$  and reactance  $X$  on the impedance  $Z$ , and the phase angle  $\varphi$  between them depends on whether the voltage leads or lags the current. (AspenCore 2022)



**Figure 4.9.** Phasor diagram and impedance triangle.

The potential  $E$  [V] is used instead of the voltage  $U$  [V] in the electrochemical experiments performed in the framework of this thesis, henceforth only the variable  $E$  is used from now on in equations. A sinusoidal potential  $E$  and current  $I$  can be expressed as seen in equations (20) and (21). The second form of the equation is in polar form. (Bard and Faulkner 2001)

$$E = E_0 \sin(\omega t) = E_0 e^{j\omega t} \quad (20)$$

$$I = I_0 \sin(\omega t - \varphi) = I_0 e^{j\omega t - j\varphi} \quad (21)$$

where  $E_0$  is peak potential [V],  $I_0$  is peak current [A],  $\omega$  is angular frequency [Hz],  $t$  is time [s],  $j$  is imaginary unit [-], and  $\varphi$  is phase angle [°].

Phasors rotate in a positive anti-clockwise in specific angular velocity also known as angular frequency  $\omega$ . Phasor  $E$  is usually used as a reference signal in horizontal axis, and the phase angle is measured respect to it. The current lags the potential, therefore the phase angle is negative in this case. (McCafferty 2010)

Ohm's law states that  $U = RI$  when the phase angle is  $0^\circ$  as seen from the Figure 4.9, so the resistive impedance  $Z_R$  is the resistance  $R$  itself. The determination of the capacitive impedance  $Z_C$  is provided below in equations (22) to (25). (Bard and Faulkner 2001)

$$E(t) = \frac{1}{C} Q(t) \quad (22)$$

$$Q(t) = I(t)t \quad (23)$$

$$\frac{dE(t)}{dt} = \frac{I(t)}{C} \quad (24)$$

$$Z_c = \frac{E(t)}{I(t)} = \frac{1}{j\omega C} \quad (25)$$

where  $Q$  is electric charge [C] and  $C$  is capacitance [F].

Euler's formula in equation (26) gives a trigonometric form for impedance when using the polar forms of potential and current from equations (20) and (21). This trigonometric form clearly shows the real and imaginary parts of impedance. This can be further represented by the resistance  $R$  and reactance  $X$ . In electrochemistry, the imaginary part of the impedance is usually always capacitive and therefore negative. (Bard and Faulkner 2001) All these equation forms are in equation (27).

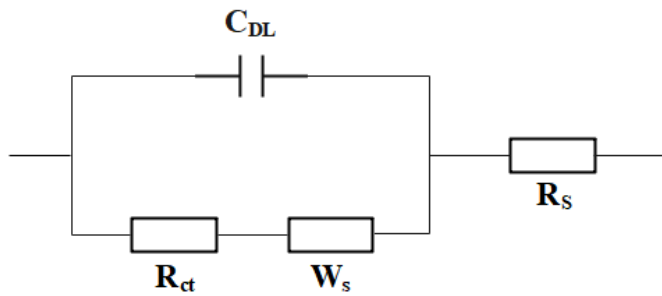
$$e^{j\varphi} = \cos\varphi + j\sin\varphi \quad (26)$$

$$Z = \frac{E}{I} = Z_0 e^{j\varphi} = Z_0 (\cos\varphi + j\sin\varphi) = R - jX = R - \frac{1}{j\omega C} = Z' - jZ'' \quad (27)$$

The impedance measurement result is presented visually as either a Nyquist plot or a Bode plot. In Nyquist, the imaginary part of the impedance  $Z''$  is on the y-axis and the real part  $Z'$  is on the x-axis. In Bode, the impedance value and phase angle are presented as a function of logarithmic scale of the frequency. (PalmSens 2022)

Randle's circuit can be used to demonstrate the electrochemical processes in a simplified manner. In its simplest form, it expresses the interaction between the electrode surface and the electrolyte. It models the electrochemical system with an equivalent circuit and therefore does not necessarily apply to real systems. The components of the Randle's circuit are the

solution resistance  $R_s$ , the double layer capacitance  $C_{dl}$ , the charge transfer resistance  $R_{ct}$  and the Warburg impedance  $W_s$ . The Warburg impedance expresses the diffusion at the electrode-electrolyte interface. These components form an equivalent circuit as follows: the solution resistance is in series with the charge transfer resistance and diffusion impedance, and the double layer capacitor is in parallel with the others. (PalmSens 2022) The Figure 4.10 below presents the circuit described earlier.



**Figure 4.10.** Randle's circuit with Warburg impedance  $W_s$ .

The circuit can be further simplified as in Figure 3.2 by excluding the Warburg element. Therefore, a mathematical representation of the total impedance can be achieved. By dividing the equivalent circuit into smaller parts, the components  $C_{dl}$  and  $R_{ct}$  in parallel form the impedance  $Z_P$  and adding the value of the series resistance  $R_s$  results in the total impedance. Capacitance is considered as capacitive reactance  $X_C$  in order to apply the rule of resistances in parallel in equation (28). The  $Z_P$  term is expanded by  $(1-j\omega C_{dl}R_{ct})$  to separate the real and imaginary parts of the impedance into separate terms in the total impedance equation (29). (McCafferty 2010)

$$Z_P = \frac{1}{R_{ct}} + \frac{1}{X_C} = \frac{1}{R_{ct}} + j\omega C_{dl} = \frac{R_{ct}}{1 + j\omega C_{dl}R_{ct}} \quad (28)$$

$$Z = R_s + \frac{R_{ct}}{1 + \omega^2 C_{dl}^2 R_{ct}^2} - j \frac{\omega R_{ct}^2 C_{dl}}{1 + \omega^2 C_{dl}^2 R_{ct}^2} \quad (29)$$

In this thesis, the Autolab PGSTAT302F -potentiostat is used to measure the electrochemical impedance. Autolab's data acquisition and analysis software NOVA acquires data points throughout the experiment. The open circuit potential (OCP) for the experiment is determined using the NOVA OCP-command. This potential is measured for 120 seconds, and the average potential is used as the reference potential for the experiment. During rest of the experiment this potential is perturbed by 30 mV amplitude within 1 mHz to 100 kHz frequency range.

Publication-ready graphs, Nyquist and Bode plots, are produced by performing data analysis with Zview<sup>®</sup> software from Scribner. The following phenomena may be seen in the plots at different frequency ranges:

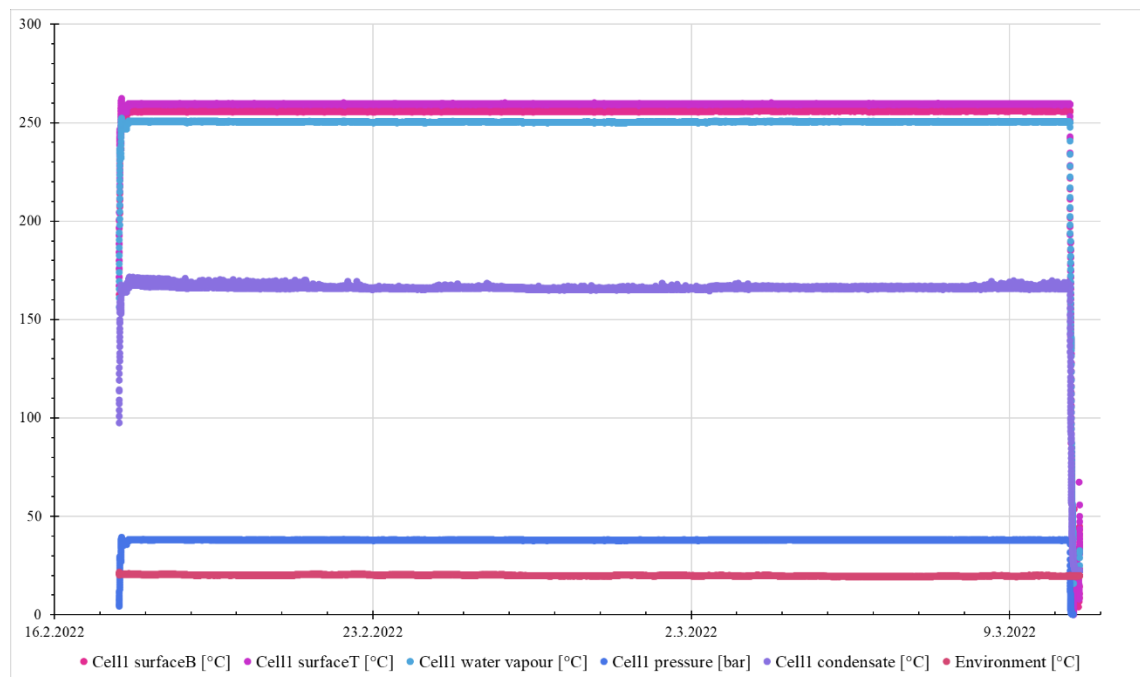
- ~ 10 kHz, solution resistance
- ~ 1 kHz, capacitance of the double layer
- 1-100 Hz, charge transfer
- < 1 Hz, diffusion and adsorption
- $f \rightarrow 0$  Hz, charge transfer or polarisation resistance (Aalto yliopisto 2015)

## 5 RESULTS AND CONCLUSIONS

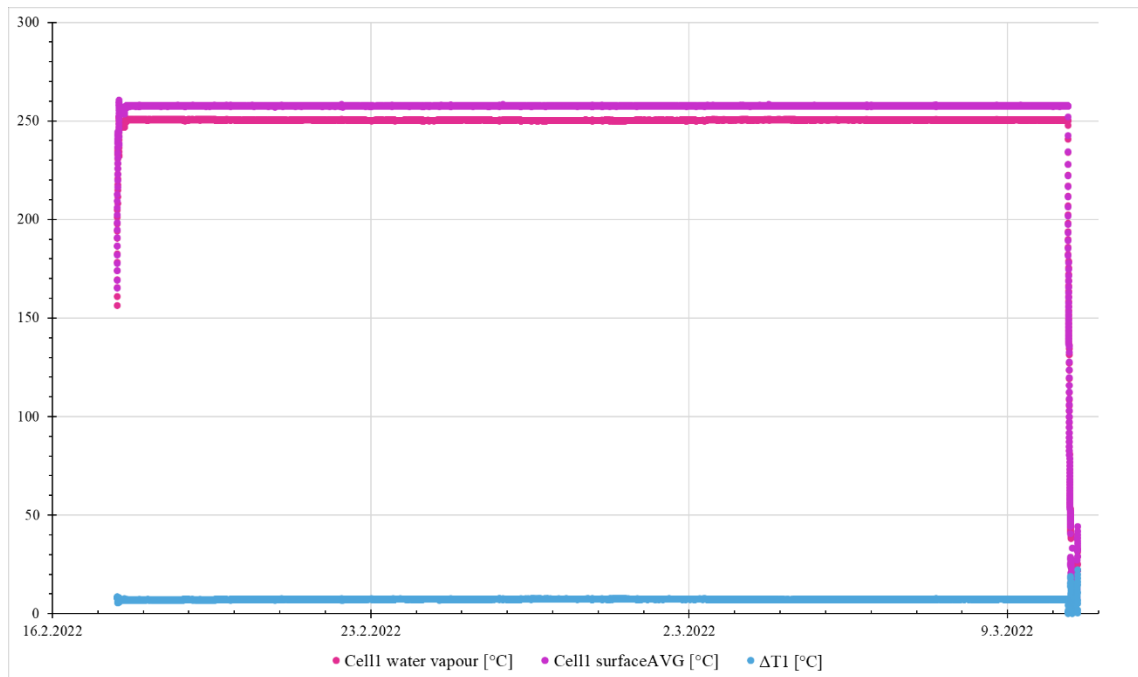
Different results were obtained from two different experimental setups. The results of the magnetite pipe cell experiment deal with a combination of mass, heat transfer and visual characteristics. The results of the second experimental setup, the laboratory equipment, were already visually inspected during the experiments, and after the experiments were completed, the electrochemical properties of the experiments were examined from the recorded graphs.

### 5.1 Heat transfer in the magnetite pipe cell

The temperature and pressure measurements of the first pipe cell experiment are presented in Figure 5.1. The temperature difference between the two measurement points of the surface of the pipe is relatively small, hence the use of the average value is feasible. The temperature of the water vapor is in the same range as the surface temperature, but there is a subtle difference. Therefore, the temperature difference of approximately 7 °C between the average pipe surface and the water vapour is presented in Figure 5.2. The rest of the measurement charts of the experiments are given in Appendix II .



**Figure 5.1.** Temperature and pressure measurements from the first pipe cell experiment as a function of time.



**Figure 5.2.** Comparison of the pipe outer surface and water temperatures of the first pipe cell experiment.

The values in Table 5.1 are averages over the experiment measurement period without transient conditions, and the convective heat transfer coefficient  $h_1$  for water vapor has been calculated based on these average values from equation (18).

**Table 5.1.** Heat transfer results.

| No. | $T_{\infty 1}$<br>[°C] | $T_{s2}$<br>[°C] | $T_{\infty 2}$<br>[°C] | $q_1$<br>[W] | $q_2$<br>[W] | $T_{s1}$<br>[°C] | $T_{s3}$<br>[°C] | $h_1$<br>[W/m <sup>2</sup> °C] |
|-----|------------------------|------------------|------------------------|--------------|--------------|------------------|------------------|--------------------------------|
| 1   | 250,35                 | 257,61           | 19,95                  | 283,49       | 16,51        | 255,94           | 46,22            | 2 525,77                       |
| 2   | 250,38                 | 257,34           |                        | 283,51       | 16,49        | 255,66           | 46,19            | 2 667,66                       |
| 3   | 250,67                 | 257,12           | 19,43                  | 283,49       | 16,51        | 255,44           | 45,70            | 2 956,22                       |
| 4   | 250,39                 | 256,45           |                        | 283,54       | 16,46        | 254,77           | 45,63            | 3 214,53                       |
| 5   | 250,67                 | 257,17           | 19,20                  | 283,47       | 16,53        | 255,50           | 45,50            | 2 922,04                       |
| 6   | 250,37                 | 255,12           |                        | 283,62       | 16,38        | 253,44           | 45,27            | 4 597,13                       |
| 7   | 274,83                 | 300,40           | 19,12                  | 330,47       | 19,53        | 298,44           | 50,20            | 696,03                         |
| 8   | 274,55                 | 282,14           |                        | 331,73       | 18,27        | 280,17           | 48,19            | 2 933,70                       |

From the Table 5.1 it can be noticed that the temperature difference between the outer and inner surface of the pipe is only about 2 °C, regardless of the experiment, meaning that the previous comparison of the water vapor temperature with the outer surface is a fair approximation of the heat transfer through the pipe wall.

The thermal resistance  $R_{th}$  through the pipe wall and the insulation was determined by two different methods to compare the heat losses of the experiments. With a higher value of thermal resistance, the less heat is conducted. The values of the two different determination methods are given in Table 5.2.

**Table 5.2.** Thermal resistances [°C/W] for pipe and insulation by two different methods.









|            | $R_{th} = \frac{\ln \frac{r_2}{r_1}}{2\pi Lk}$ | $R_{th} = \frac{\Delta T}{q}$ |
|------------|--|-------------------------------|
| Insulation | 11,03  | 12,81                         |
| Pipe       | 0,0059191                                      | 0,0059196                     |

As the table above states that the insulation resisted the heat transfer, and the heat was transferred through the pipe wall without much resistance. Depending on the method of calculation, there is a slight difference in the values of the thermal resistance of the insulation, although the values are nevertheless within the same range. Regardless of the calculation method used for the thermal resistance of the pipe wall, the values are basically the same.

## 5.2 Gravimetric measurement

Table 5.3 provides the measured pH values and the filtrations overviews. All images of the filtrations can be found in Appendix III . The masses in the table indicate how much loose material was in the pipe and how much of it is adhered to the inner surfaces of the pipe.

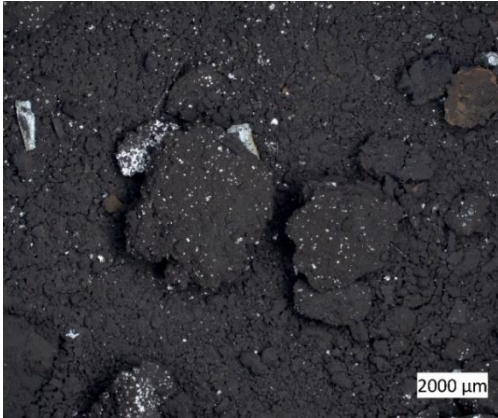
**Table 5.3.** Results of the substances used in the pipe cell experiments.

| No. | Measured pH | Filtration  | Filter |      | Pipe  |      |
|-----|-------------|---|--------|------|-------|------|
|     |             |   | [g]    | [%]  | [g]   | [%]  |
| 1   | 10,02       |    | 0,598  | 74,8 | 0,202 | 25,2 |
| 2   | 8,43        |    | 0,940  | 72,9 | 0,350 | 27,1 |
| 3   | 9,21        |    | 0,595  | 61,0 | 0,381 | 39,0 |
| 4   | 9,68        |   | 0,717  | 64,0 | 0,403 | 36,0 |
| 5   | 9,18        |  | 0,931  | 71,0 | 0,381 | 29,0 |
| 6   | 7,71        |  | 0,751  | 57,9 | 0,546 | 42,1 |
| 7   | 9,58        |  | 1,018  | 78,4 | 0,281 | 21,6 |
| 8   | 9,66        |  | 0,808  | 62,2 | 0,492 | 37,8 |

The figures in the table above show that the used substances have partially agglomerated during the pipe cell experiments. However, the big lumps are quite porous and broke easily when handling the filtrations.

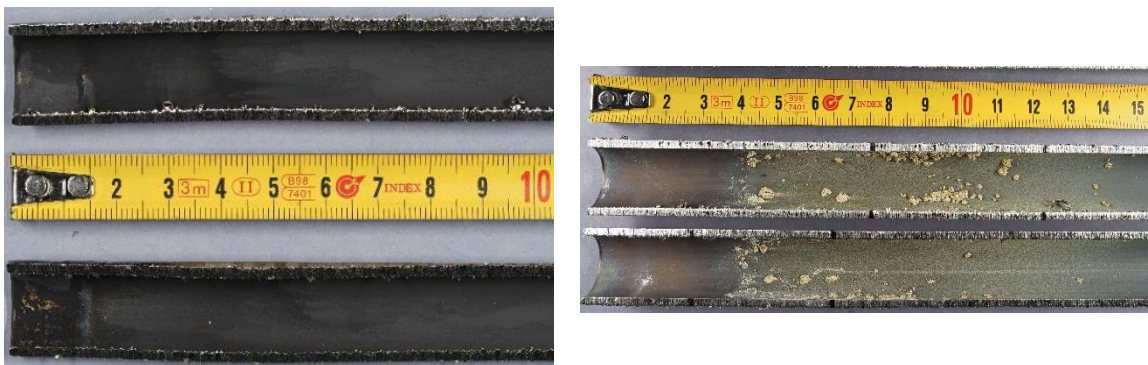


The transition from magnetite to hematite is affected by redox and hydrothermal conditions as discussed in subsection 2.3. While examining the filtration from the fourth pipe experiment, small amounts of reddish tones were detected as seen in Figure 5.3. This suggests the formation of hematite, which in turn indicates that oxygen was present in the pipe during the experiment, despite the deoxygenation methods used.



**Figure 5.3.** 8X magnification of the filtration from the fourth pipe cell experiment.

The masses and percentages in the table indicate that most of the substances come out of the pipe, but there are still enough remaining substances on the inner surface of the pipe to allow different flow patterns and deposits to be distinguished by eye. The deposits have also hardened and adhered to the surface if they have not been removed during the sawing process. Figure 5.4 below demonstrates the flow patterns and hardened deposits on the inner surface of the pipe.



**Figure 5.4.** Distinct flow patterns in the first magnetite pipe cell (left) and hardened alumina-silica deposits on the inner surface of the sixth cell (right).

In the sixth, seventh and eighth experiments, clearly visible hardened deposits were formed on the inner surface of the pipe. In the sixth experiment, higher concentrations of alumina and silica were applied, and no magnetite was used. This higher amount of hardness species probably contributed to their agglomeration and deposit hardening. The amount of

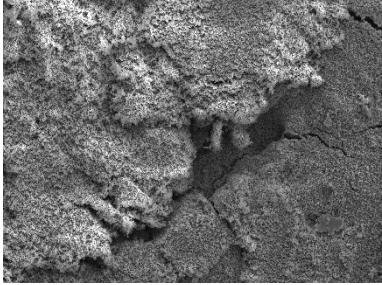
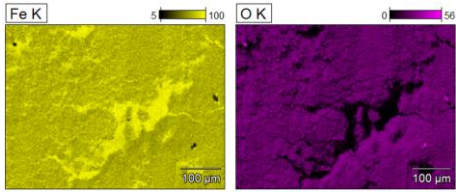
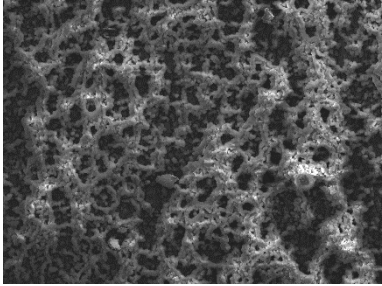
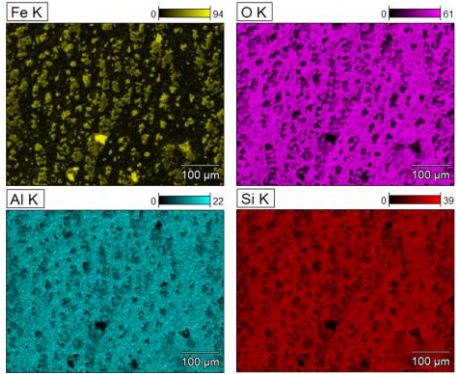
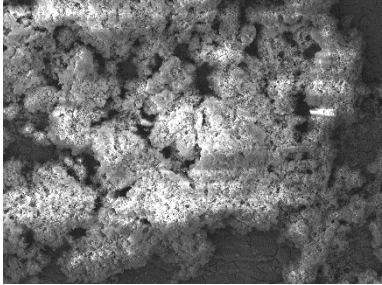
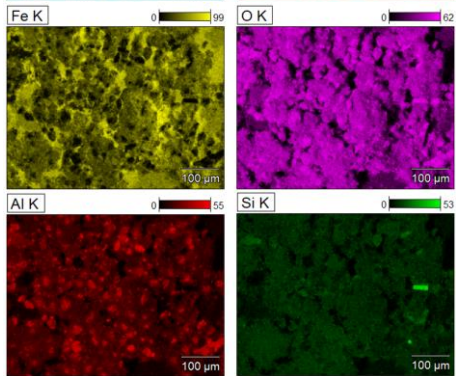
substances on the surface of the pipe in the seventh and eighth experiments does not differ much from the lower temperature experiments, but hardened deposits were observed, suggesting that temperature has a significant effect on agglomeration and solidification.

### **5.3 SEM and EDS results**

All samples were imaged at 200X and 750X magnifications with SEM. The surface differences of the pipe cell experiments were observed at 200X magnification and their equivalent EDS maps achieved the highest possible accuracy with this magnification and settings. An overview of the interesting area in the SEM buttons was taken at 200X magnification and the EDS map at 750X, so that the small subtle differences could be detected. All the SEM images of the pipe samples and buttons with corresponding EDS maps are presented in Appendix IV.

Table 5.4 contains SEM images and EDS maps of the three pipe cell experiments with different experimental conditions regarding substances and temperature. The first experiment served as a reference, as only magnetite and pH-control chemicals have been used. The topography of this pipe is quite flat and simple compared to other experiments. With the addition of cementitious factors, alumina and silica, different microscopic lumps and patterns were formed on the surface of the pipes. As the temperature was increased, the lumps became both larger and appeared more compact.

**Table 5.4.** SEM images and elemental maps of the three pipe cell samples with microscopic differences.

| No. | SEM image   | EDS map  |
|-----|---|--|
| 1   |    |    |
| 2   |   |   |
| 8   |  |  |

The main difference in the SEM buttons is in the regions formed by alumina and silica as seen in Table 5.5, since the first four experiments used unfiltered alumina and the remaining ones filtered. The noticeable feature is that the filtered alumina together with the silica has not only formed large isolated dense areas but are also more or less dominant substances in the sample. It is also interesting that magnetites, alumina, and silica did not really mix with each other in any of the experiments, instead they seem to have their own clear regions in elemental maps. Carbon (C) was taken into account in the maps of the SEM buttons, as it was the major component of the casting resin and appears as black areas in the SEM images.

**Table 5.5.** SI acquisition from different filtration castings.


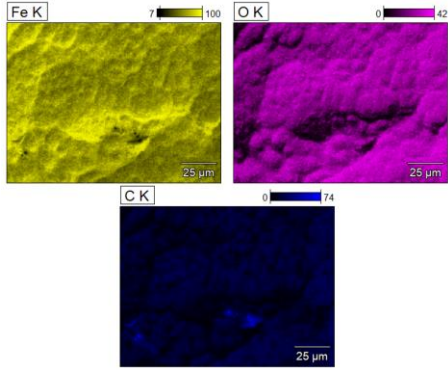
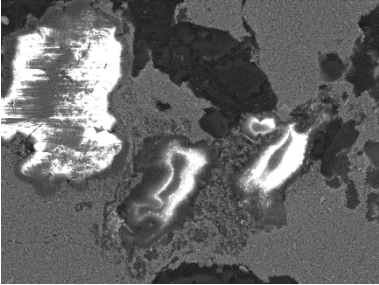
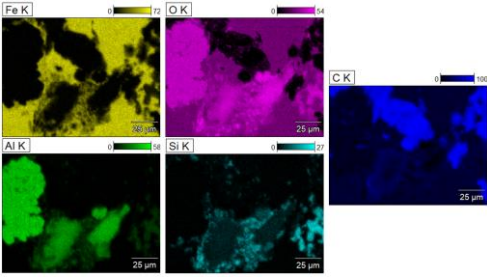
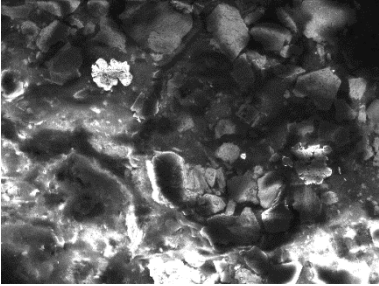
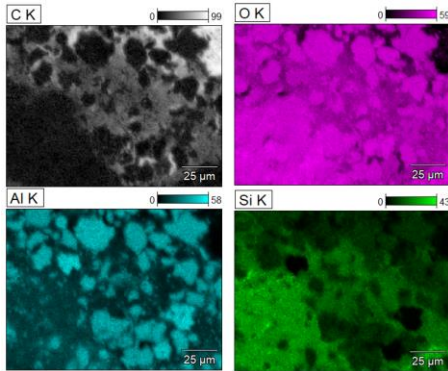
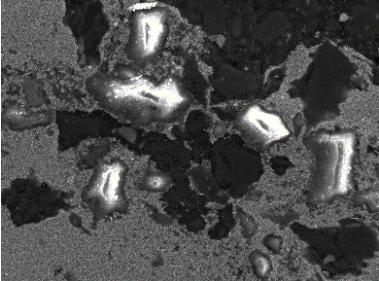
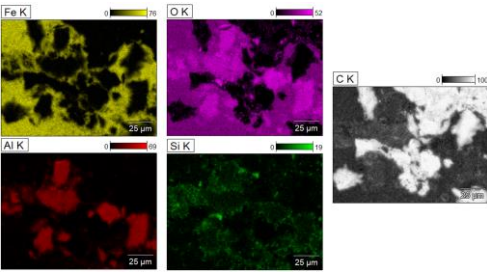
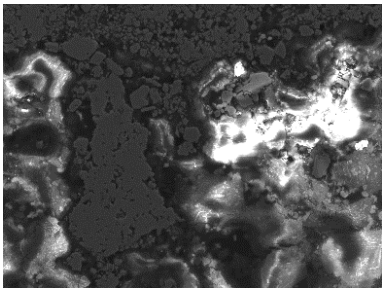
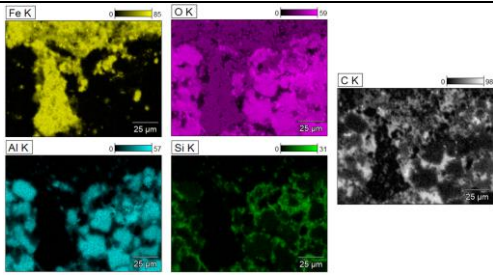
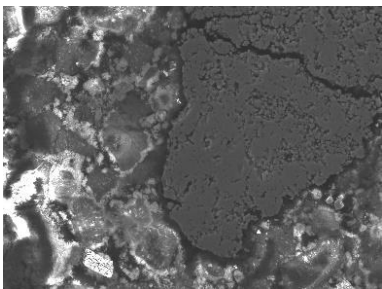
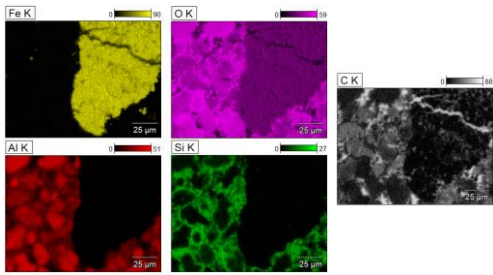
| No. | SEM image   | EDS map  |
|-----|---|--|
| 1   |    |    |
| 2   |   |   |
| 6   |  |  |
| 8   |  |  |

Table 5.6 provides SEM button images and corresponding elemental maps for the 5<sup>th</sup> and 7<sup>th</sup> pipe cell experiments performed with the magnetite powder from the Loviisa NPP. Despite the different water temperatures between these two experiments, there are no major differences in the SEM button images or elemental maps.

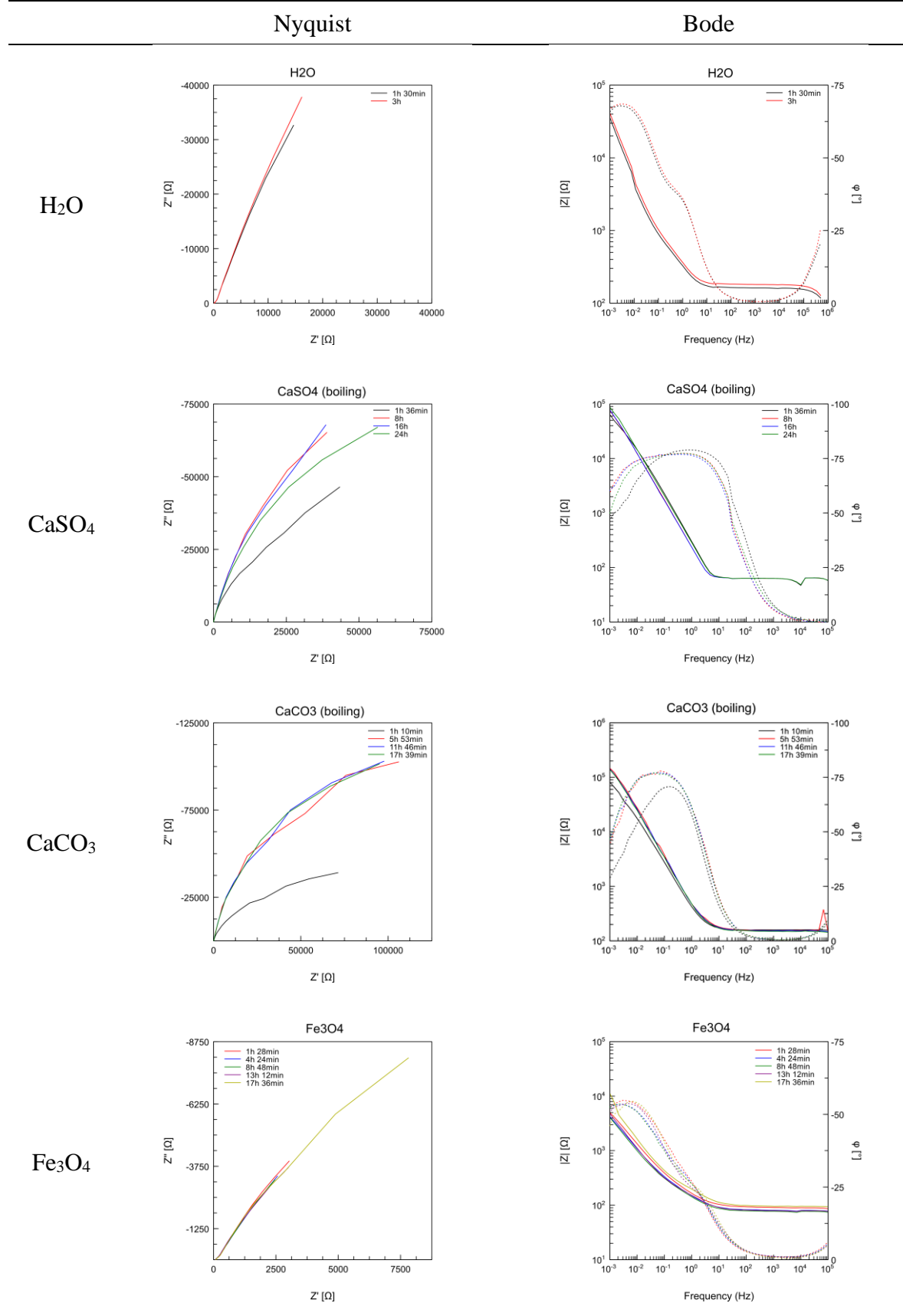
**Table 5.6.** SEM images and EDS maps of the filtrations from the pipe experiments using Loviisa magnetite.

| No. | SEM   | EDS  |
|-----|---|--|
| 5   |  |  |
| 7   |  |  |

When comparing the visual characteristics of the Loviisa magnetite powder with the commercial Goodfellow<sup>®</sup> magnetite between the experiments, it can be seen that the commercial magnetite is smaller and more powdery.

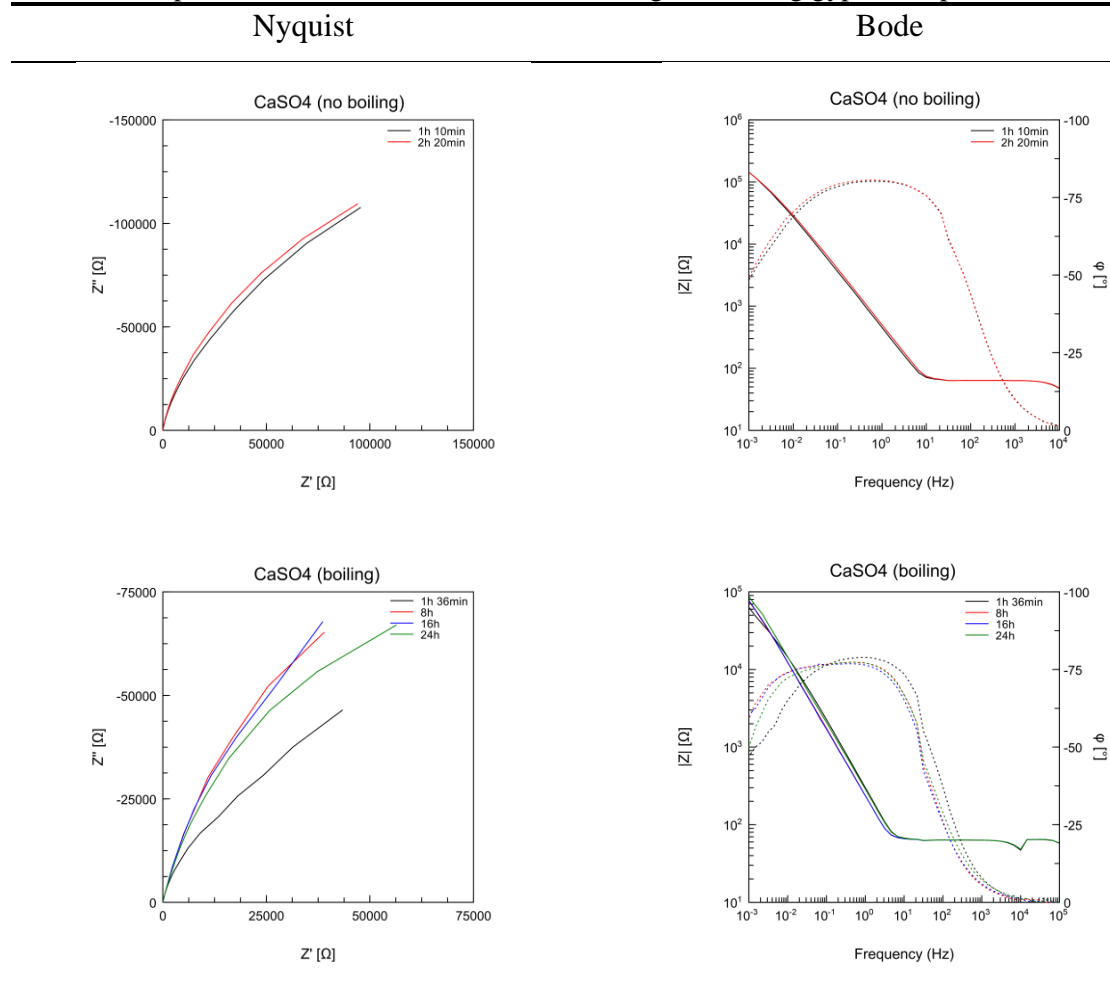
#### 5.4 EIS results and equivalent circuit analysis

The Nyquist and Bode plots of the experiments present the formed oxide layer, and in a few cases also the electrical double layer is detected. Table 5.7 shows the plots in four different experimental environments, although under the same condition, boiling.

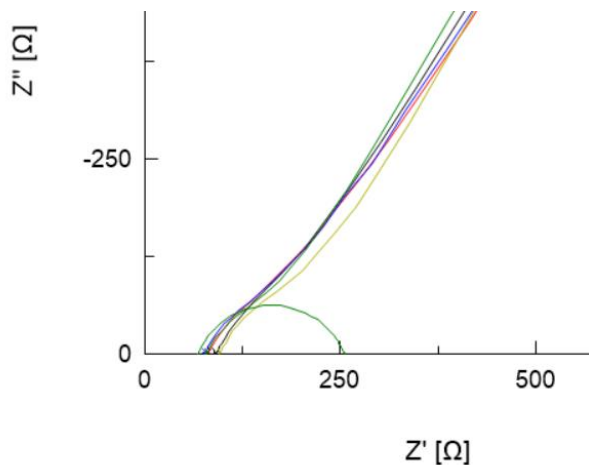
**Table 5.7.** Nyquist and Bode plots in four different experimental environments.

The comparison of the impedance measurements of the non-boiling and boiling gypsum experiments in Table 5.8 shows that there are no major differences. The non-boiling process has greater impedance values in the real and imaginary parts in the Nyquist plot. The curves between the processes have very similar shape in the Bode plots with small subtle movements on the angle and impedance values.

**Table 5.8.** Impedance measurements of the non-boiling and boiling gypsum experiments.

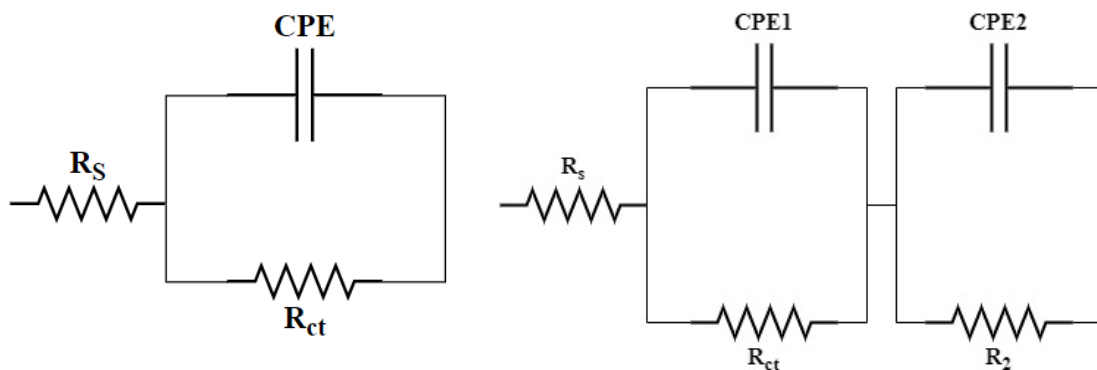


All the Bode plots of gypsum show a small offset exactly at 10 kHz, regardless of the condition of the experiment. As it did not occur in other environments, it was interpreted as a device artifact. A small semicircle is seen in the Nyquist plot of pure water and magnetite at the beginning, indicating the detection of an electrical double layer. A close-up of this observation is shown in Figure 5.5. The Nyquist and Bode plots for all experiments are presented in Appendix V.



**Figure 5.5.** The Nyquist plot of magnetite. Green semicircle is for visualisation.

Equivalent circuits can be created from the graphs using instant fit or user-defined models. The formed oxide layer on the metal surface and the detected EDL can be modelled as equivalent circuits as shown in Figure 5.6.



**Figure 5.6.** The simple equivalent circuit on the left represents the formed oxide layer and, on the right, the EDL components are added to the circuit.

The solution resistance  $R_s$  is determined from the Nyquist plot at the point where the curve would intersect with the x-axis. The values of the charge transfer resistance  $R_{ct}$  and the migration resistance of current carriers in the film  $R_2$  are obtained by imagining the curve as a semicircle and using that diameter as the value. CPE consist of two parameters: CPE-T and CPE-P. The typical starting value for the CPE-T is  $10^{-5}$  and for the CPE-T 0,75 since it ranges from 0,5 to 1.

Using these assumptions, a simulation can be done with Zview<sup>®</sup> to see how suitable the fit is. The fit can then be further fitted to the original data with a margin of error less than 10%. Once the fit is satisfactory, the values of the CPE parameters can be used to determine the double layer capacitance of the experiment by equation (30). The results of the fitting of the experiments are shown in Table 5.9. The grey cells in the table are the values for the detected



electrical double layer. Since several measurements have been recorded in the experiment, the fit has been generalized based on the measurements.

$$C = (CPE-T)^{1/CPE-P} \quad (30)$$

**Table 5.9.** Results of EIS from equivalent circuits by fitting.

| No. | $R_s$ [ $\Omega$ ] | CPE-T                   | CPE-P   | $C$ [ $\mu$ F] | $R_{ct} / R_2$ [ $\Omega$ ] |
|-----|--------------------|-------------------------|---------|----------------|-----------------------------|
| 1   | 52,58              | $6,234 \times 10^{-4}$  | 0,74295 | 48,507         | 29 000                      |
| 2   | 161,3              | $1,717 \times 10^{-3}$  | 0,63307 | 42,857         | 1 157                       |
|     |                    | $3,795 \times 10^{-3}$  | 0,97839 | 3 355,391      | 75 458                      |
| 3   | 13,87              | $6,420 \times 10^{-4}$  | 0,84477 | 166,305        | 217 540                     |
| 4   | 936                | $3,7366 \times 10^{-4}$ | 0,85766 | 100,840        | 123 170                     |
| 5   | 503,4              | $9,6994 \times 10^{-4}$ | 0,84524 | 272,289        | 107 020                     |
| 6   | 43,83              | $3,6213 \times 10^{-4}$ | 0,82699 | 69,018         | 271 720                     |
| 7   | 54,94              | $7,1492 \times 10^{-4}$ | 0,84035 | 180,563        | 191 730                     |
| 8   | 54,09              | $4,5669 \times 10^{-4}$ | 0,8481  | 115,170        | 302 040                     |
| 9   | 226,5              | $3,6568 \times 10^{-4}$ | 0,83484 | 76,413         | 88 923                      |
| 10  | 152,3              | $4,499 \times 10^{-4}$  | 0,86211 | 131,159        | 284 640                     |
| 11  | 194,5              | $4,1127 \times 10^{-4}$ | 0,88025 | 142,399        | 173 770                     |
| 12  | 70,37              | $6,113 \times 10^{-5}$  | 0,84103 | 9,767          | 290 900                     |
| 13  | 74,35              | $1,1507 \times 10^{-4}$ | 0,79672 | 11,374         | 415 700                     |
| 14  | 76,13              | $5,235 \times 10^{-3}$  | 0,54337 | 63,383         | 176,4                       |
|     |                    | $7,7247 \times 10^{-3}$ | 0,7292  | 1 269,149      | 19 971                      |

## 5.5 Error analysis

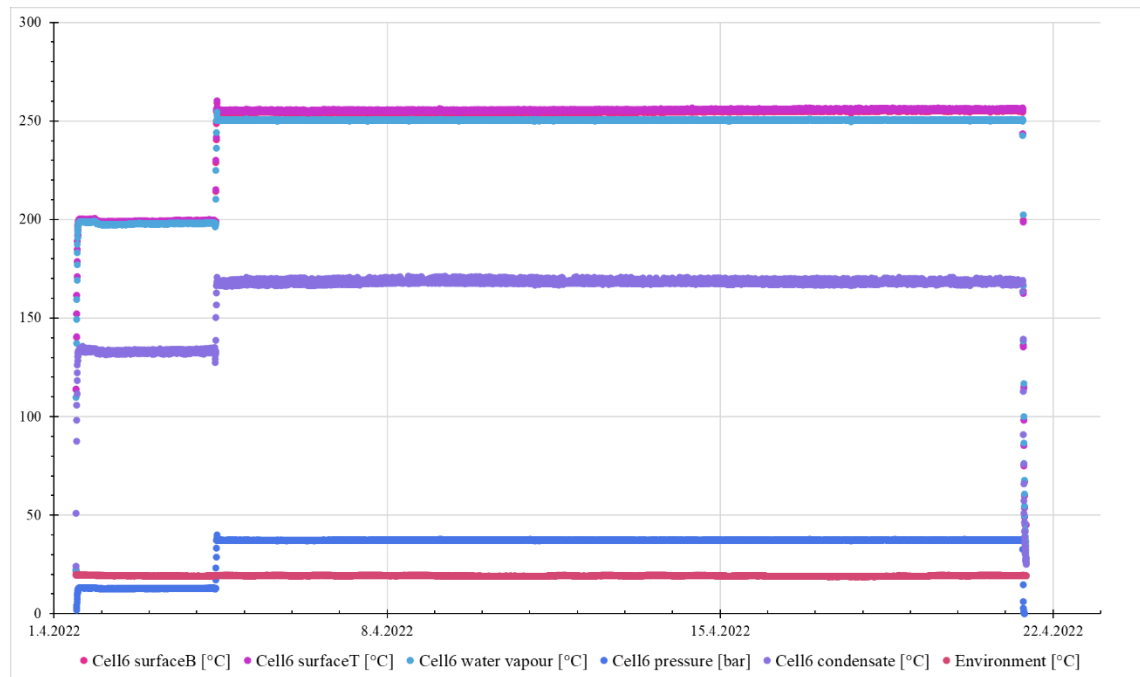
The experimental setups used in this thesis are, as their name suggests, experimental, so there may be various errors or other unknown factors that influence the outcome of the experiments.

### 5.5.1 Heat transfer

Various assumptions were made regarding the calculation of heat transfer. Despite having data throughout the experiment, only the steady state part of the data was used, and therefore the heat transfer did not take transient conditions into account. Also, averages were taken of both the measured and calculated heat transfer results to determine the convective heat

transfer coefficient from the pipe to the water vapor. Thus, these determined values are only indications and could vary at different times.

The measurement data for magnetite pipe cell 6 differs from the other experiments as the pipe was not insulated at the beginning of the experiment. This can be seen in the measurement data chart in Figure 5.7.



**Figure 5.7.** Measurement data of the sixth magnetite pipe cell.

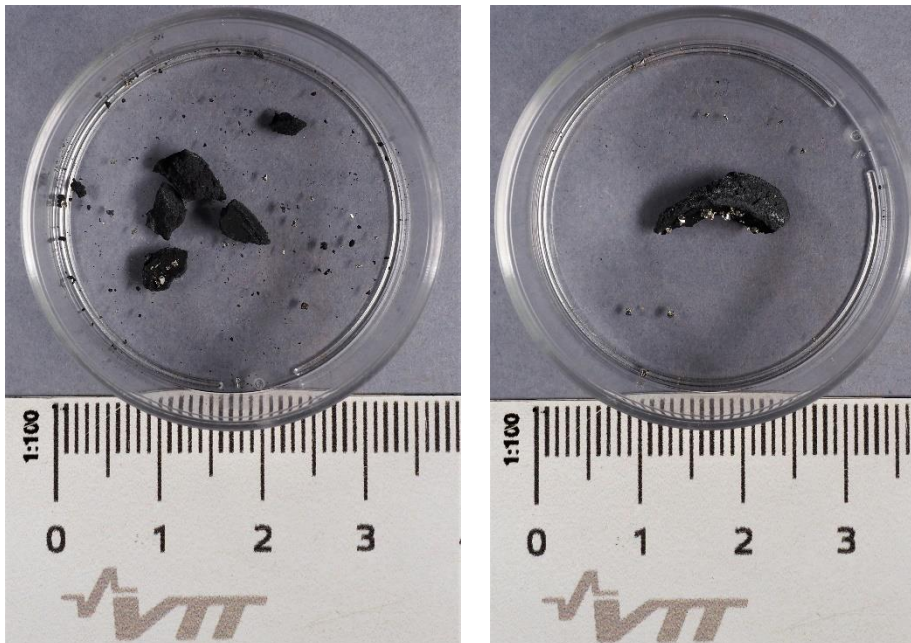
Due to the lack of insulation, the water vapor pressure and temperature of the experiment did not reach the desired level. Although the experiment reached a steady state without insulation, the data during this period is excluded from the heat transfer calculations, in order to have comparable heat transfer results among all of the experiments.

The temperature of 250 °C was chosen for pipe cell experiments from 1 to 6 on the basis that it roughly corresponds to the average temperature of the inlet feedwater and the outlet steam of the steam generator. However, the local conditions at the deposition sites can be significantly different from the overall conditions in the steam generator, so for the last two experiments the temperature was increased to 275 °C. This increase in temperature had a major impact on the formation of hardened magnetite deposits, as in previous experiments such visible lumps had barely formed at all on the inner surface of the pipes. The formed and hardened magnetite deposits can be seen in Figure 5.8 of the eighth pipe cell experiment.



**Figure 5.8.** Deposited and hardened magnetite from the 8<sup>th</sup> pipe cell experiment.

A couple of the lumps were not adhered tightly enough to the surface of the pipe, so they became detached during the sawing process, but the lumps remained intact. The average size of the lumps is 1 cm as can be seen in Figure 5.9.



**Figure 5.9.** The detached magnetite deposits from the 8<sup>th</sup> pipe cell.

### 5.5.2 SEM and EDS

The four most interesting parts of each pipe are selected visually and from these pieces the most interesting parts are imaged by SEM, meaning that only a fraction of the pipe is actually imaged. However, it should be noted that these four pieces are selected from different sites so that they represent different regions of the pipe experiment.

Both SEM imaging and EDS in particular were hampered by the curvature of the pipe specimens. The SEM image did not focus properly if the imaged area was too close to the

vertical outer edges, because the SE detector is positioned above the imaging platform at an inclined angle. The EDS detector is located on the other side of the chamber in the same way as the SE and requires a good view of the imaging surface. If the store rate of the sample is small, the elemental map of the sample will not be very accurate, because the EDS detector cannot detect and store enough X-rays in the sample spectrum.

Other species were also detected by EDS, but their maps were not accurate, more like dots here and there. Most of these species, such as Cr, Ni, Cu and Mo, were part of the chemical composition of the pipe material. They were also not among the possible contributors to deposit formation and hardening and were therefore excluded.

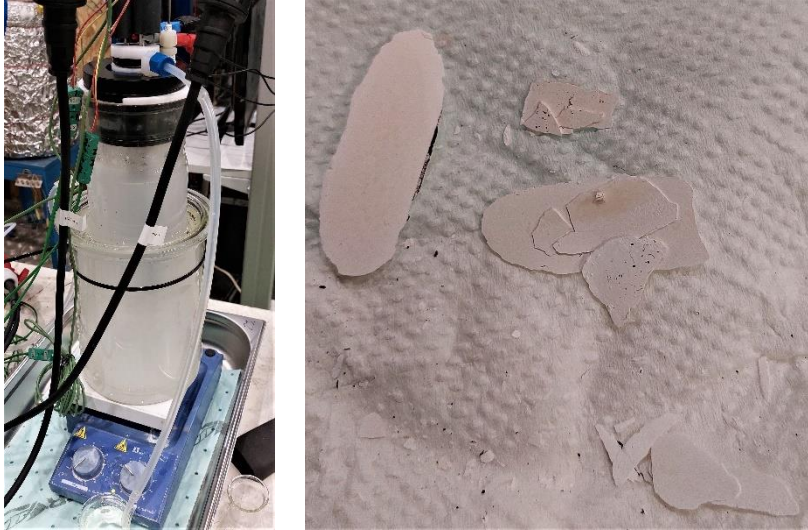
When imaging SEM buttons that contained alumina and/or silica, it was sometimes difficult to have a good image quality, as many times the areas were overexposed. As a result, SEM images may not be equally accurate at every pixel and not all the smallest differences could be detected from the images. This was not found to have an effect on the accuracy of the EDS elemental maps. Epoxy buttons also had their own difficulties, as it seemed that not all areas were conductive enough for imaging, even though they had been sputtered with platinum.

### **5.5.3 In-situ deposit monitoring setup**

This experimental setup had many different parameters affecting the environment and the duration of the experiment. When the cooling water container was full, its water level was approximately midway up to the metal blocks inside the glass jar. As a result, the lower part of the metal blocks did not heat up enough and the water did not boil, while the upper part was covered with visible bubbles caused by boiling. The water level in the cooling container was lowered below the metal blocks to ensure uniform boiling over the entire surface.

The amount of calcium sulphate ( $\text{CaSO}_4$ , gypsum) added to the jar was considerably more than 2 litres of water would dissolve, resulting in a saturated solution. However, phenomena such as boiling or partial deposition could not be visually observed as the solution became quite turbid as presented in Figure 5.10. Gypsum deposited on the metal surface, but it would not adhere for long, instead it would always pop off after a while. This popping was clearly due to the intense boiling between the surfaces and the bubbles that formed on the surface. Furthermore, the deposition was never uniform over the entire surface, rather it was

concentrated in the upper and lower parts of the metal block. The deposition and popping off was continuous which led to the floating gypsum flakes in the solution, as well as to a clearer solution. Some of the gypsum flakes were recovered intact at the end of the experiment, as seen in Figure 5.10, while others dissolved back into the water.



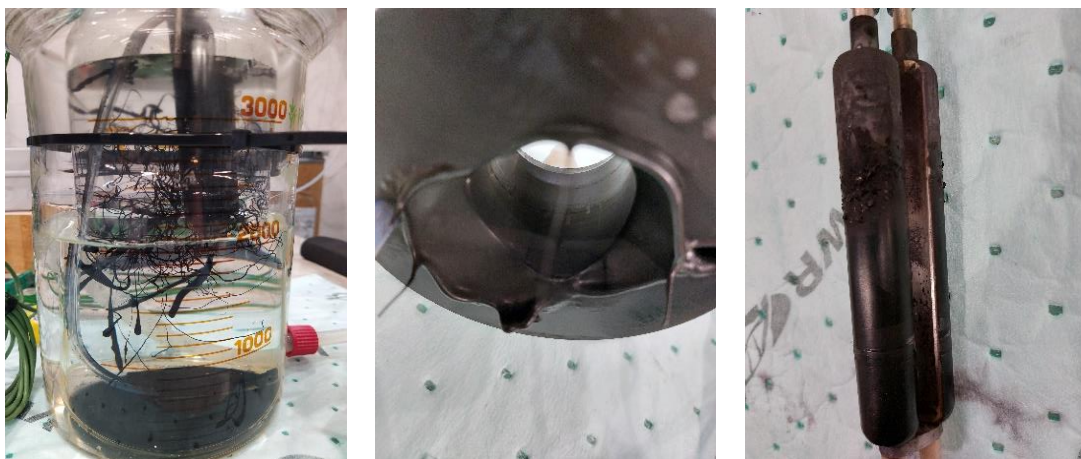
**Figure 5.10.** Saturated turbid solution and the formed gypsum flakes.

Since the area was probably too large for the formation of a uniform deposit, the surface area was reduced by lining the metal blocks with Teflon tape. This resulted in an area of about 1x1 cm in the center of the metal blocks. As the metal blocks heated up, the tape was partially burnt onto the PFA-coating. However, the tape could not withstand the duration of the experiment, thus water and the used substances got between the tape and the metal surface. The conditions in the gap were favorable for the initiation of pitting corrosion. The results of these phenomena can be seen in Figure 5.11.



**Figure 5.11.** Metal blocks lined with Teflon tape to reduce surface area (up) and pitting corrosion on the metal surface as a result of heavy boiling between the tape and the metal surface (down).

Since no uniform deposit was formed on the surfaces with either of the surface areas, it was not detectable in the impedance measurements. Only one experiment was conducted with magnetite since the experimental setup broke down during this experiment. The melting of the PFA coating and the POM plastic lid was probably the sum of several individual events: the intensity of the nitrogen bubbling, the amount of cooling water, the power, the temperatures, and the substances used. Hydrofluoric acid (HF) may have formed in the glass jar because of the melting of the PFA-coating and potentially its chemical reaction with the water. HF is toxic and corrosive, so utmost caution had to be taken when dismantling the experimental setup. Failure of the experimental setup and its melted parts are presented in Figure 5.12.



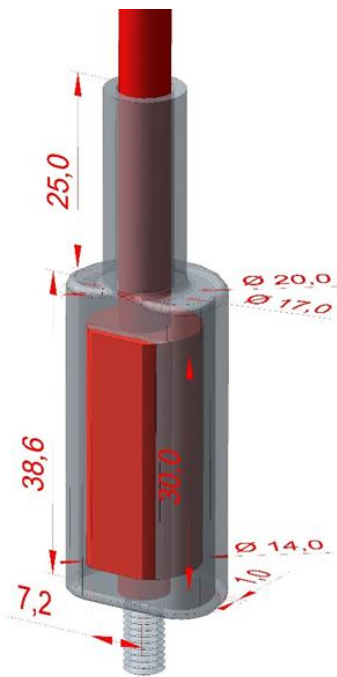
**Figure 5.12.** Failure and meltdown of the experimental setup.

## 6 FUTURE CONSIDERATIONS

Based on the experiments performed in this thesis, further research on the deposition and hardening of magnetite with the existing or new experimental setups has been discussed within the research team.

A new version or further experiments on the pipe cells have not yet been officially planned, but ideas have been expressed. To better simulate the VVER steam generator design, one option would be to place the pipe in a horizontal position. However, this arrangement would require considerably more space than the vertical version used. Since the temperature was found to have a major effect on the formation of the hardened deposits, it would be beneficial if the effect of the different temperatures on the deposition could be studied in a single experiment. For example, this could be achieved by having several heating resistors in series around the pipe with different power levels, so that the temperature inside the pipe would change depending on the section. Experimentation with other hardening species such as magnesium (Mg) and calcium (Ca) would also be preferable. Also, EDS analyses could be further refined by another X-ray based method (e.g. XRD) to obtain information on the crystal structure.

Following the destruction of the laboratory experiment, a new version of this experimental setup is under development. The new version has only one 30 mm long metal block with a 14 mm diameter, with a heating resistor inserted inside. The sample is encased in a thin-walled tube, which acts as a thermal chamber and creates an air gap around the sample. The casing will be coated, and the coating should be more durable as no boiling should occur there. Deposit formation should occur on the bare flat 7x30 mm surface of the sample.



**Figure 6.1.** Layout of the new version of the experimental setup for deposition formation monitoring.

It would be a good addition to combine this experimental setup with a similar data measurement as the one used in the pipe cell experiments. This would allow a more detailed monitoring of several properties (the water, sample surface and heating resistor temperatures). To avoid equipment failure, some extra safety precautions should be considered. An alternative option could be to use some kind of water level measurement, so that if for some reason the level drops below the set limit, the heating resistor is switched off.



## 7 SUMMARY

This master's thesis studied the factors influencing the deposition and hardening of magnetite in the steam generators of a pressurized water nuclear power plant. The first part of the thesis focused on the operation of the steam generator itself and the corrosion problems that occur in the secondary circuit. The dissolved magnetite by flow-accelerated corrosion from the carbon steel parts of the secondary circuit is transported to the steam generator by the feed water, where fouling contributes to the formation of the deposit. Among the interparticle forces, the deposit formation is influenced by the electrical double layer and the zeta potential, whereby the charged magnetite particles adhere to the surface of the steam generator. As the magnetite particles become attached to the surface and more and more of them accumulate, along with other substances such as alumina and silica, the deposit begins to harden.

Two experimental setups were designed for the study of deposition and hardening of magnetite. Experiments with the magnetite pipe cell were conducted at the secondary circuit pressures, temperatures, and water chemistry of the PWR plant. Samples from these experiments were analysed together with the SEM and EDS to detect even the smallest differences. Although not all the applied substances deposited on the inner surface of the pipe in the cell experiments, informative results were obtained after filtering the loose material. Both visual and microscopic examination of the filtrations revealed the formation of agglomerations and porous lumps. Hardened deposits were formed when only alumina and silica were present, and when the experiment temperature was increased from 250 °C to 275 °C in the last two pipe cell experiments.

The second experimental setup, the in-situ laboratory system, allowed shorter experiments to be performed and to test whether the electrochemical impedance spectroscopy would be suitable for detecting the presence of deposits. A visual inspection was possible during the experiments to observe the experimental conditions and whether a deposit was forming. No coherent deposit was formed during the laboratory experiments with the different substances. The oxide layer on the metal surface was identified in the EIS measurements, and in a few cases the electrical double layer was also detected. When this particular setup was destroyed during the magnetite experiment, an improved model was suggested.

## REFERENCES

- Aalto yliopisto. 2015. Sähkökemialliset tutkimusmenetelmät - Impedanssispektroskopia [online]. Available at: <https://docplayer.fi/48303105-Mt-sahkokemialliset-tutkimusmenetelmat.html> [accessed May 31, 2022].
- Agilent. 2022. Inductively Coupled Plasma Optical Emission Spectroscopy (ICP-OES) [online]. Available at: <https://www.agilent.com/en/support/atomic-spectroscopy/inductively-coupled-plasma-optical-emission-spectroscopy-icp-oes/icp-oes-instruments/icp-oes-faq> [accessed February 25, 2022].
- Ahmed, W.H. 2012. Flow Accelerated Corrosion in Nuclear Power Plants, Nuclear Power - Practical Aspects. IntechOpen. <https://doi.org/10.5772/51346>
- AspenCore. 2022. Phasor Diagram and Phasor Algebra used in AC Circuits [online]. Basic Electron. Tutor. Available at: <https://www.electronics-tutorials.ws/accircuits/phasors.html> [accessed March 8, 2022].
- Bard, A.J., Faulkner, L.R. 2001. Electrochemical methods: fundamentals and applications, 2nd ed. Wiley, New York.
- Bergman, T.L., Incropera, F.P. (Eds.). 2011. Fundamentals of heat and mass transfer, 7th ed. Wiley, Hoboken, NJ.
- Breeze, P.A. 2014. Power generation technologies, Second edition. Newnes, Amsterdam.
- Burrill, K.A. 1977. The deposition of magnetite particles from high velocity water onto isothermal tubes. Canada.
- Elimelech, M. (Ed.). 2010. Particle deposition and aggregation: measurement, modelling and simulation, Nachdr., Colloid and surface engineering series. Butterworth-Heinemann, Woburn, Mass.
- EPRI. 2003. Multivariable Assessment of Flow Accelerated Corrosion and Steam Generator Fouling: Literature Review. Palo Alto.
- EPRI. 2002. Identification and Testing of Amines for Steam Generator Chemistry and Deposit Control.
- Féron, D. 2012. Nuclear corrosion science and engineering, Woodhead Publishing series in energy. Woodhead Pub, Cambridge, UK ; Philadelphia, PA.
- Green, S.J., Hetsroni, G. 1995. PWR steam generators. *Int. J. Multiph. Flow*, Annual Reviews in Multiphase Flow 1995 21, 1–97. [https://doi.org/10.1016/0301-9322\(95\)00016-Q](https://doi.org/10.1016/0301-9322(95)00016-Q)
- Hunter, R.J. 1981. Zeta potential in colloid science: principles and applications, Colloid science. Academic Press, London ; New York.
- IAEA. 2011. Chemistry programme for water cooled nuclear power plants: specific safety guide, IAEA Safety standards series Specific safety guide. IAEA, Vienna.

IAEA. 2008. Water Chemistry of WWER Nuclear Power Plants.

IEA. 2022. IEA – International Energy Agency [online]. IEA. Available at: <https://www.iea.org> [accessed February 8, 2022].

Ikäläinen, T., Sipilä, K., Jäppinen, E. 2020. Zeta potential of stainless steel particles in NH<sub>3</sub> or NH<sub>3</sub>+ODA controlled water chemistries (No. VTT-R-00143-20). VTT Technical Research Centre of Finland, Espoo.

Jones, R.H. (Ed.). 1992. Stress-corrosion cracking. ASM International, Materials Park, Ohio.

Kang, K.S., Kupca, L., IAEA. 2011. Assessment and management of ageing of major nuclear power plant components important to safety: steam generators. International Atomic Energy Agency, Vienna.

Khalifeh, A. 2019. Stress Corrosion Cracking Damages, Failure Analysis. IntechOpen. <https://doi.org/10.5772/intechopen.80826>

Kritsky, V.G. 1999. Water chemistry and corrosion of nuclear power plant structural materials, Russian materials monograph series. American Nuclear Society, La Grange Park, Ill.

Li, Z., Chanéac, C., Berger, G., Tireau, J., Graff, A., Bachet, M., Lefèvre, G. 2020. Mechanism and kinetics of hematite reduction under typical PWR secondary circuit condition. J. Nucl. Mater. 533, 152132. <https://doi.org/10.1016/j.jnucmat.2020.152132>

Lyklema, H.J. 1995. Fundamentals of interface and colloid science. Academic press, London.

Makhlouf, A.S.H., Aliofkhazraei, M. 2016. Handbook of materials failure analysis with case studies from the oil and gas industry. Elsevier Butterworth-Heinemann, Amsterdam.

McCafferty, E. 2010. Introduction to corrosion science. Springer, New York.

Melo, L.F., Bott, T.R., Bernardo, C.A. 1988. Fouling Science and Technology. Springer Netherlands, Dordrecht.

Murtomäki, L., Kallio, T., Lahtinen, R. 2019. Fundamental electrochemistry [online]. Available at: <https://mycourses.aalto.fi/mod/book/view.php?id=388663> [accessed February 4, 2022].

Nanakoudis, A. 2019. What is SEM? Scanning Electron Microscopy Explained [online]. Accel. Microsc. Available at: <https://www.thermofisher.com/blog/microscopy/what-is-sem-scanning-electron-microscopy-explained/> [accessed December 8, 2021].

NASA. 2013. Understanding the Atom [online]. Available at: <https://imagine.gsfc.nasa.gov/science/toolbox/atom.html> [accessed March 1, 2022].

Nishida, K., Saka, K., Tanahashi, A. 2002. IMPROVEMENT OF SLUDGE REMOVAL PERFORMANCE FOR STEAM GENERATORS 11.

Odar, S., Nordmann, F. 2010. PWR AND VVER SECONDARY SYSTEM WATER CHEMISTRY – STAND ALONE REPORT 65.

PalmSens. 2022. Introduction to the Corrosion Research Knowledgebase [online]. PalmSens. Available at: <https://www.palmsens.com/knowledgebase-article/introduction-to-the-corrosion-research-knowledgebase/> [accessed December 15, 2021].

Pedefferri, P. 2018. Corrosion Science and Engineering, Engineering Materials. Springer International Publishing, Cham. <https://doi.org/10.1007/978-3-319-97625-9>

Riznic, J.R. (Ed.). 2017. Steam generators for nuclear power plants, Woodhead Publishing series in energy. Woodhead Publishing, Oxford.

Shaw, D.J. 1992. Introduction to colloid and surface chemistry, 4th ed. Butterworth-Heinemann, Oxford ; Boston.

Slugeň, V. 2011. Safety of VVER-440 Reactors. Springer London, London. <https://doi.org/10.1007/978-1-84996-420-3>

Swapp, S. 2017. Scanning Electron Microscopy (SEM) [online]. Techniques. Available at: [https://serc.carleton.edu/research\\_education/geochemsheets/techniques/SEM.html](https://serc.carleton.edu/research_education/geochemsheets/techniques/SEM.html) [accessed December 1, 2021].

Thermo Fisher. 2022. SEM Sample Preparation [online]. Available at: <https://www.thermofisher.com/uk/en/home/materials-science/learning-center/applications/sample-preparation-techniques-sem.html> [accessed April 13, 2022].

Top Analytica Oy Ab. 2021. Elektronimikroskopia (SEM-EDS/WDS) [online]. Available at: [https://www.topanalytica.com/Elektronimikroskopia-\(SEM-EDS/WDS/EBSD\)](https://www.topanalytica.com/Elektronimikroskopia-(SEM-EDS/WDS/EBSD)) [accessed December 15, 2021].

Trunov, N.B., Dragunov, Yu.G. 2004. Optimization of the Tube-Bundle Arrangement in Horizontal Steam Generators. At. Energy 97, 450–458. <https://doi.org/10.1023/B:ATEN.0000045696.90836.cf>

Turner, C.W. 2011. Implications of Steam Generator Fouling on the Degradation of Material and Thermal Performance 14.

Tyapkov, V.F., Erpyleva, S.F. 2017. Water chemistry of the secondary circuit at a nuclear power station with a VVER power reactor. Therm. Eng. 64, 357–363. <https://doi.org/10.1134/S0040601517050081>

Varrin, R., Jr. 1996. Characterization of PWR Steam Generator Deposits. EPRI, Palo Alto.

Vepsäläinen, M. 2010. Deposit formation in PWR steam generators (No. VTT-R-00135-10). VTT Technical Research Centre of Finland, Espoo.

Vidojkovic, S., Rodriguez-Santiago, V., Fedkin, M.V., Wesolowski, D.J., Lvov, S.N. 2011. Electrophoretic mobility of magnetite particles in high temperature water. Chem. Eng. Sci. 66, 4029–4035. <https://doi.org/10.1016/j.ces.2011.05.021>

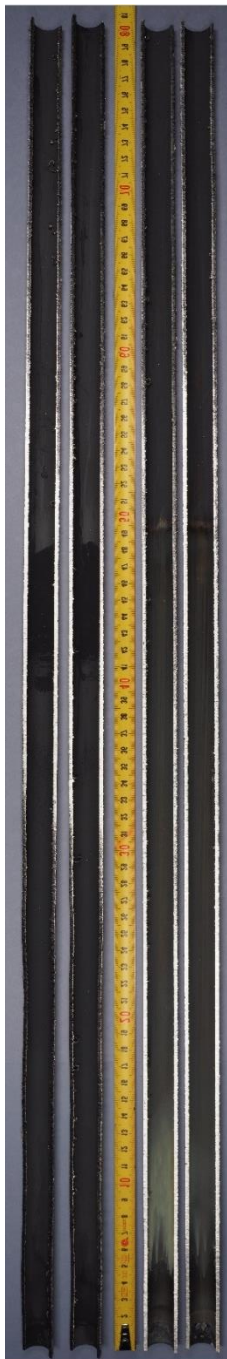
WebCorr. 2022. Different Types of Corrosion - Mechanisms, Recognition & Prevention [online]. Available at: [https://www.corrosionclinic.com/different\\_types\\_of\\_corrosion.htm](https://www.corrosionclinic.com/different_types_of_corrosion.htm) [accessed February 17, 2022].

World Nuclear Association. 2022. Nuclear Energy in Finland | Finnish Nuclear Power - World Nuclear Association [online]. Available at: <http://www.world-nuclear.org/information-library/country-profiles/countries-a-f/finland.aspx> [accessed February 8, 2022].

Xie, Y., Zhang, J. 2016. Corrosion and deposition on the secondary circuit of steam generators. *J. Nucl. Sci. Technol.* 53, 1455–1466.  
<https://doi.org/10.1080/00223131.2016.1152923>

Appendix I High-pressure and temperature magnetite cells

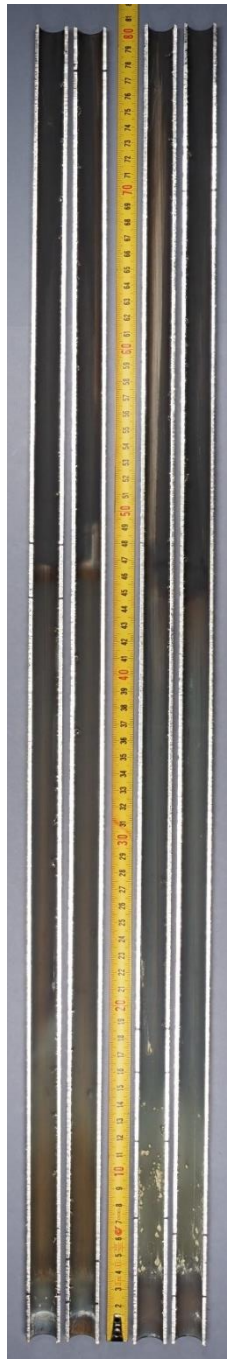
1 & 2



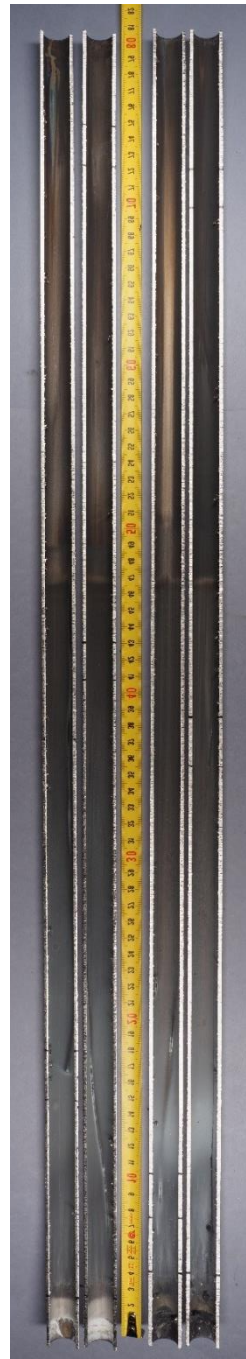
3 & 4



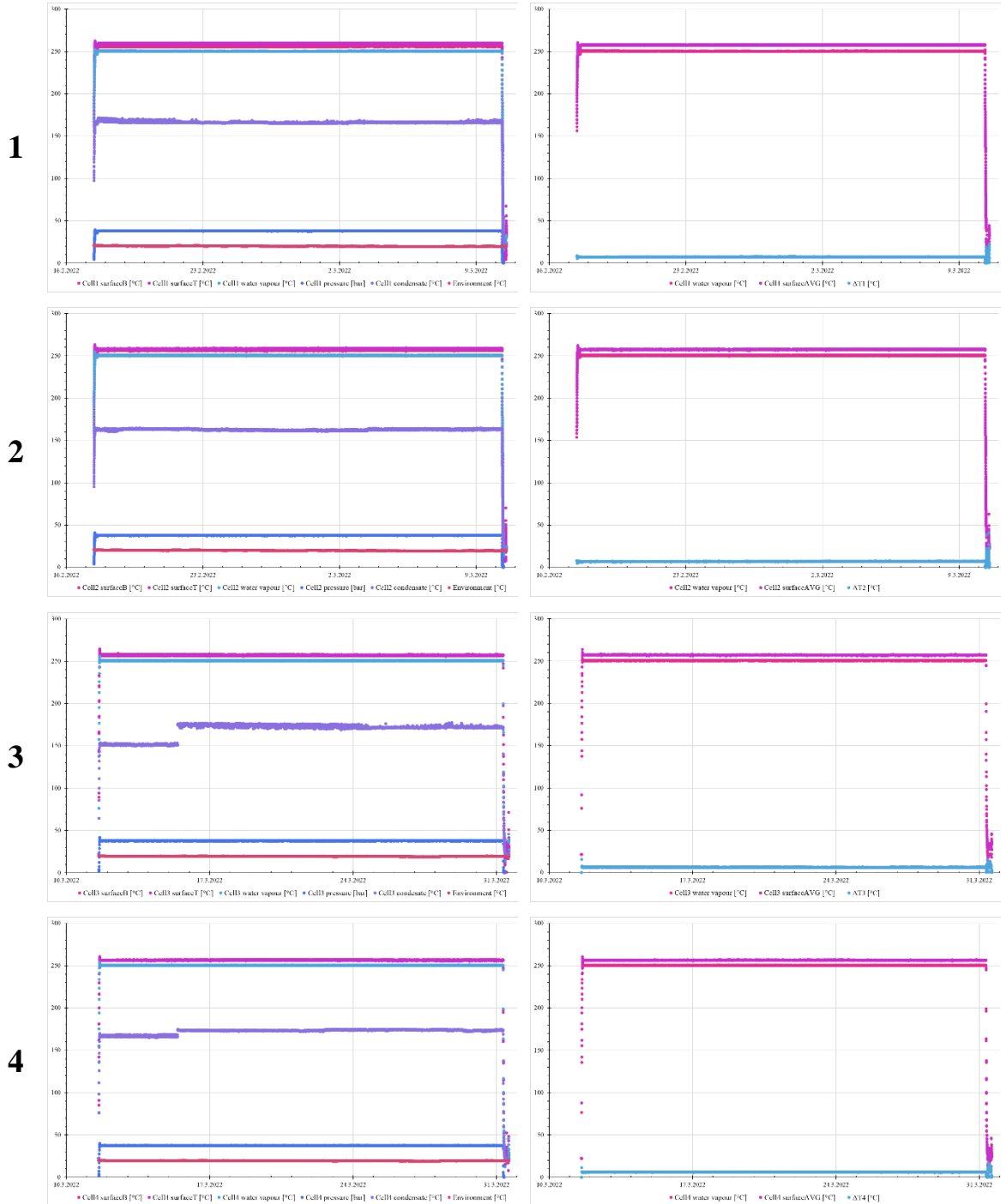
5 & 6



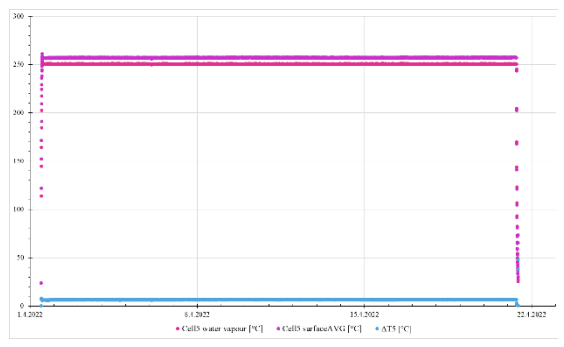
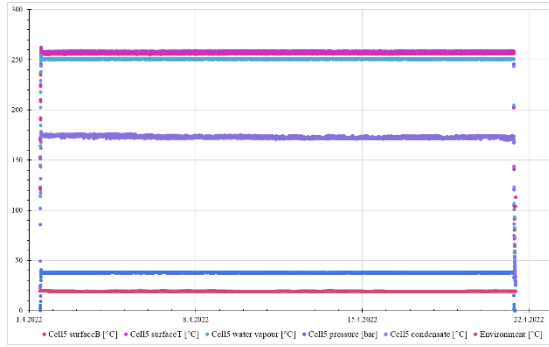
7 & 8



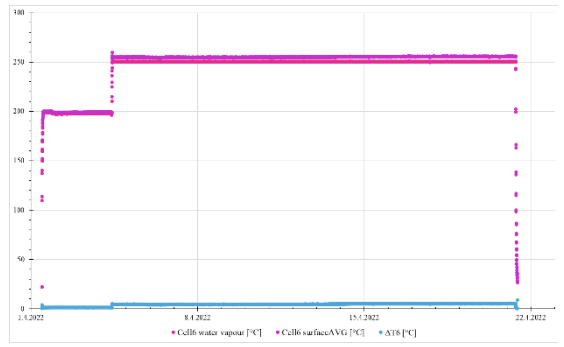
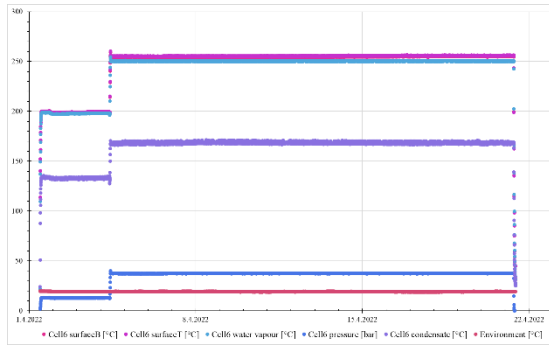
## Appendix II Temperature and pressure data measurements from the magnetite cell experiments



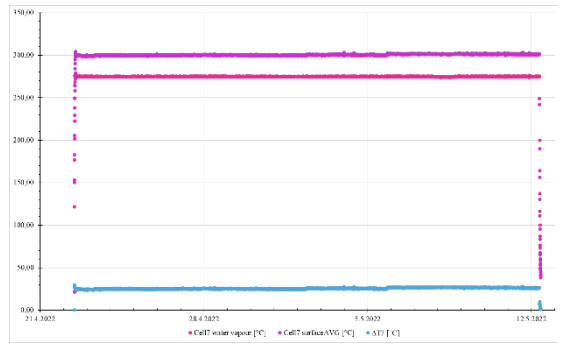
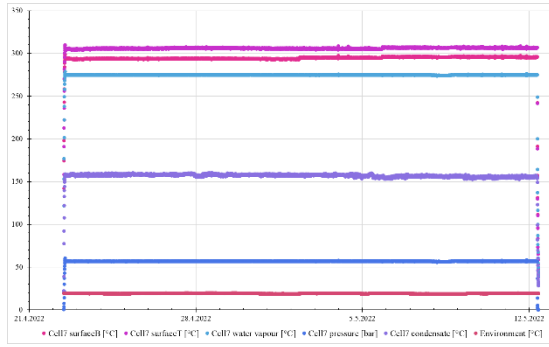
5



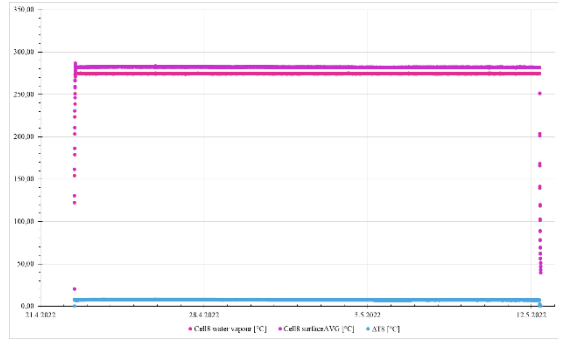
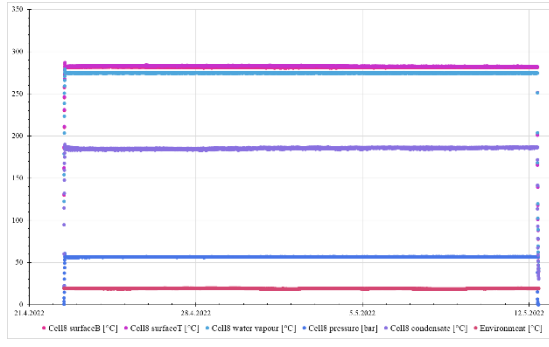
6



7

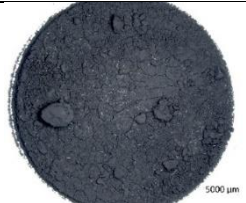
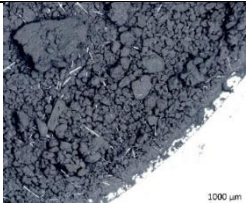
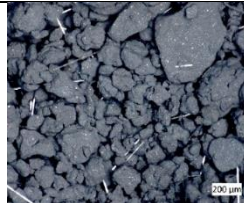
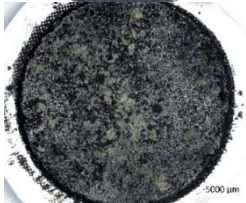
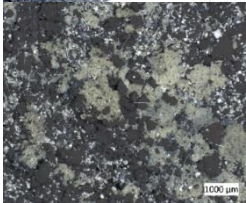
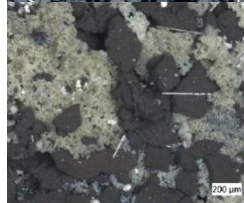
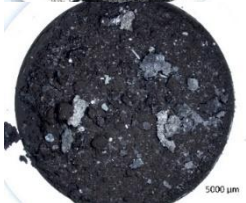
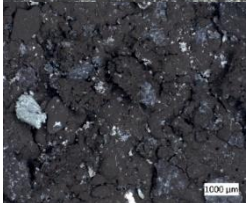
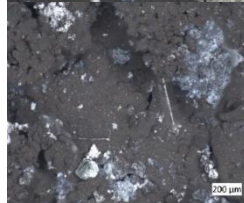
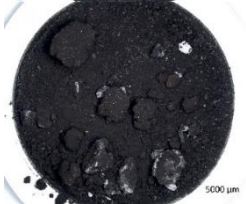
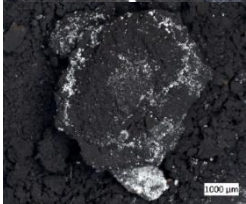
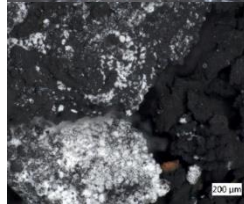

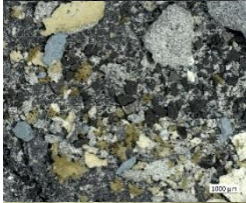
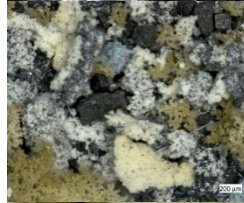











8



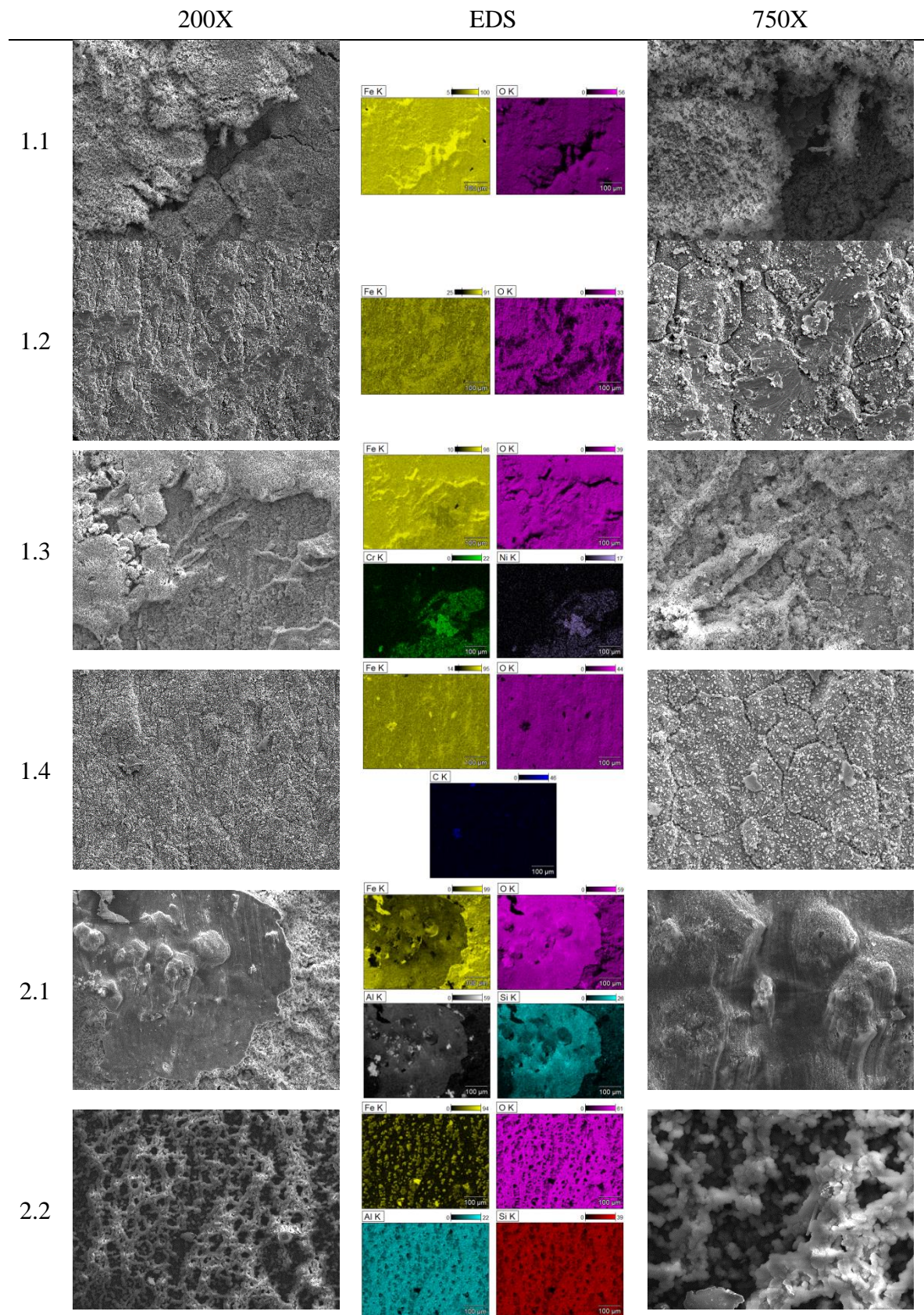


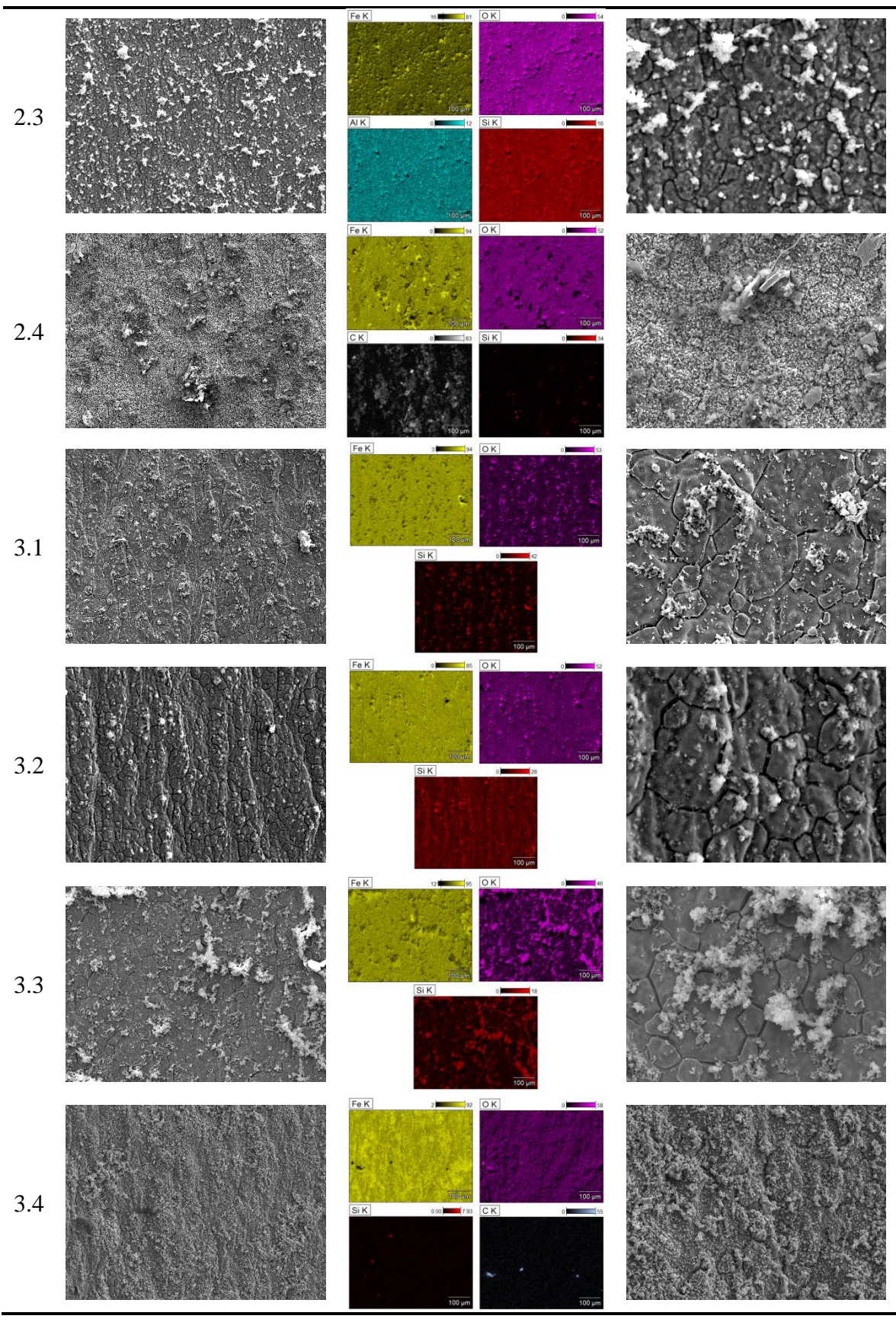
Appendix III Filtrations with Zeiss Axio Zoom V16 microscope

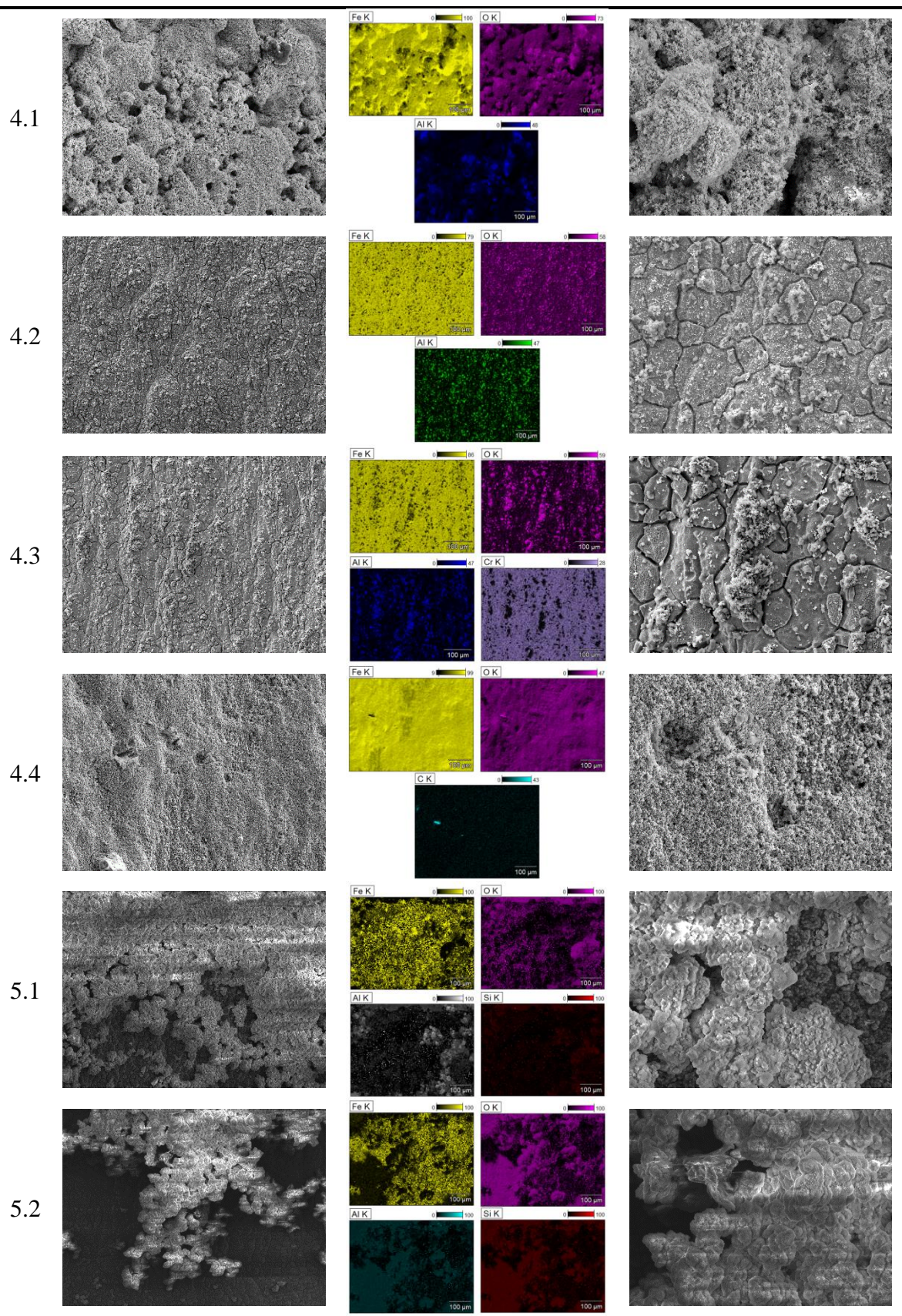
| Experiment | Overview  | 16X  | 56X   |
|------------|---|--|---|
| 1          |    |    |    |
| 2          |    |    |    |
| 3          |   |   |   |
| 4          |  |  |  |
| 5          |  |  |  |
| 6          |  |  |  |
| 7          |  |  |  |
| 8          |  |  |  |

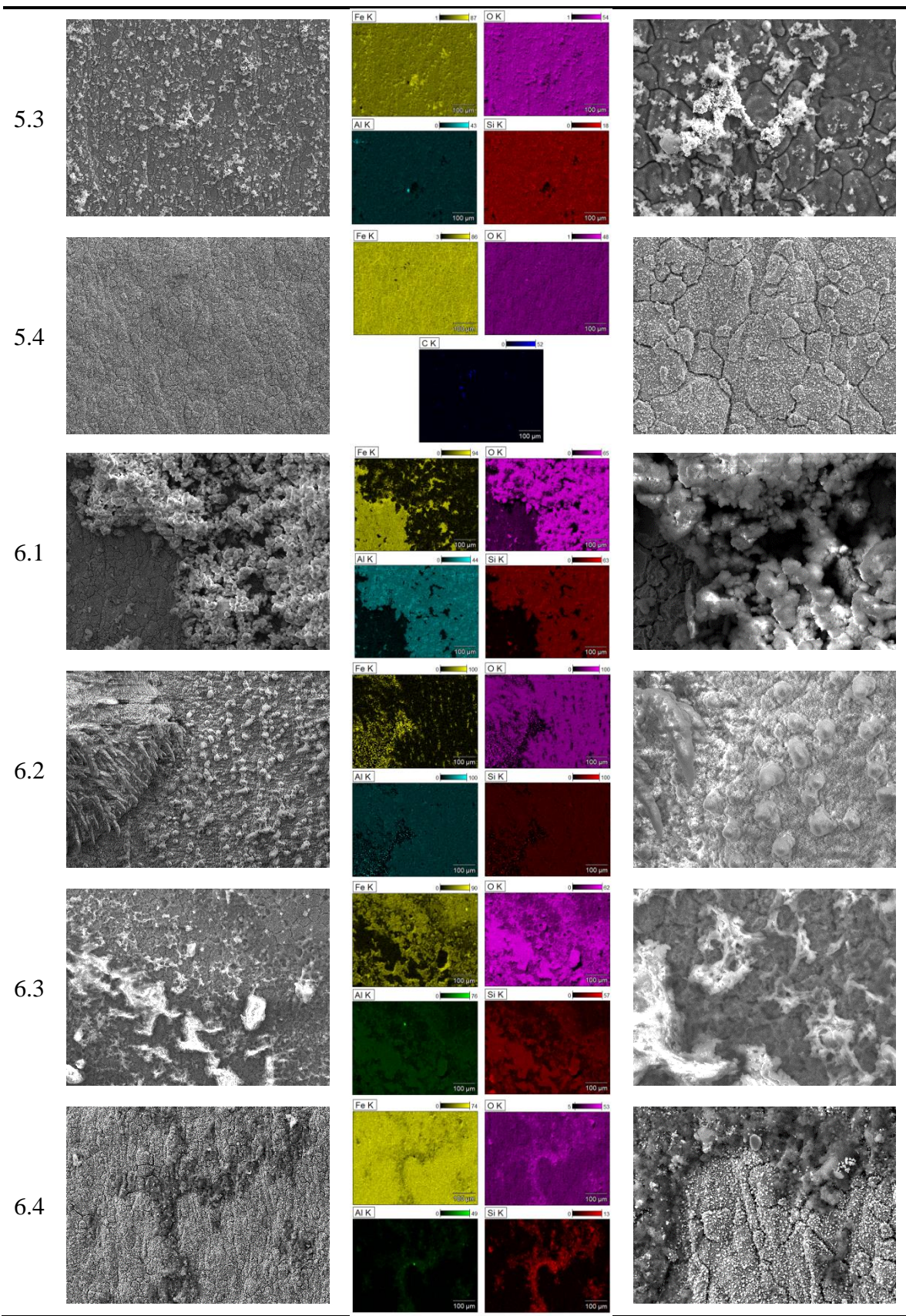
# Appendix IV SEM images and elemental maps

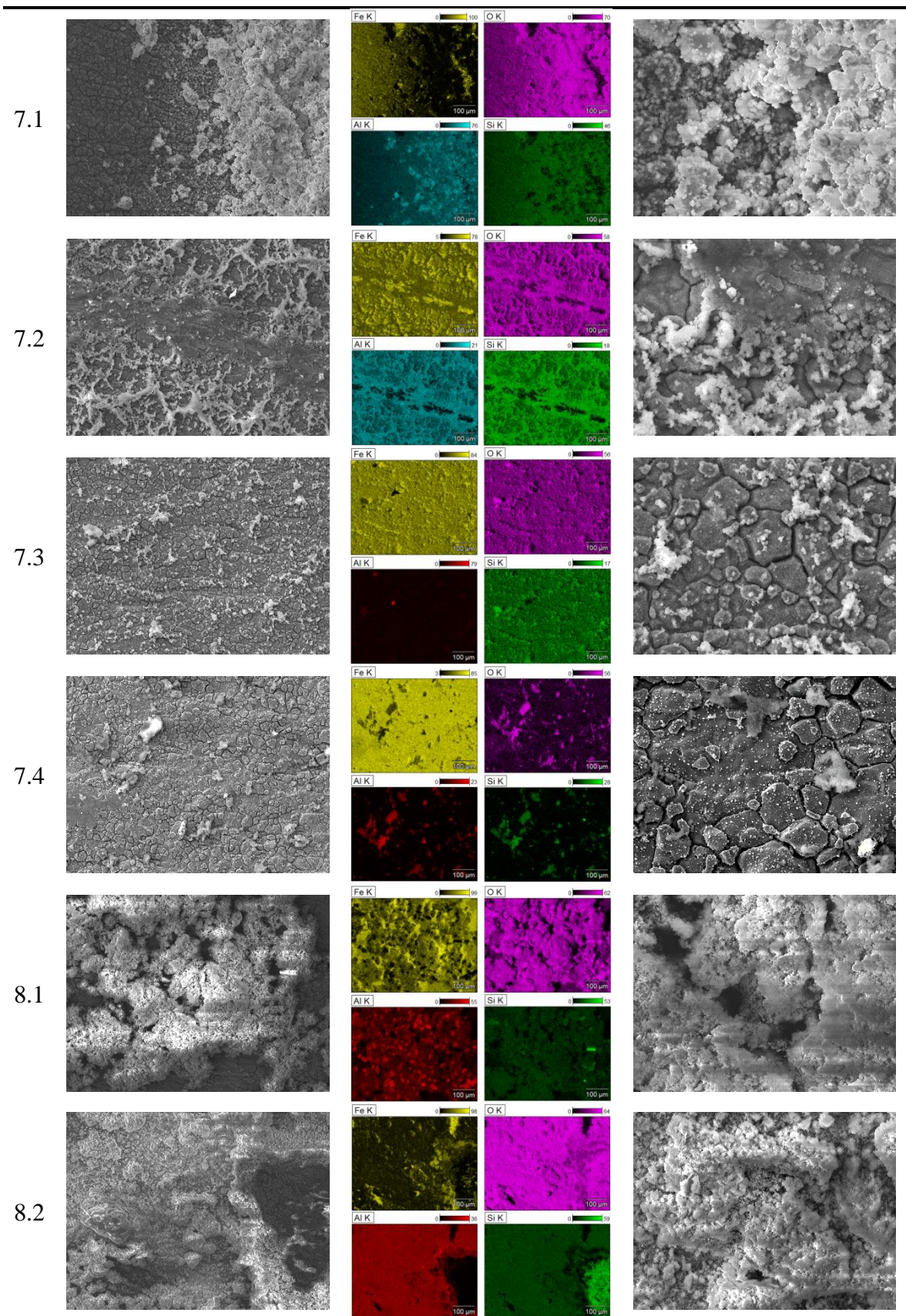
## Pipe pieces

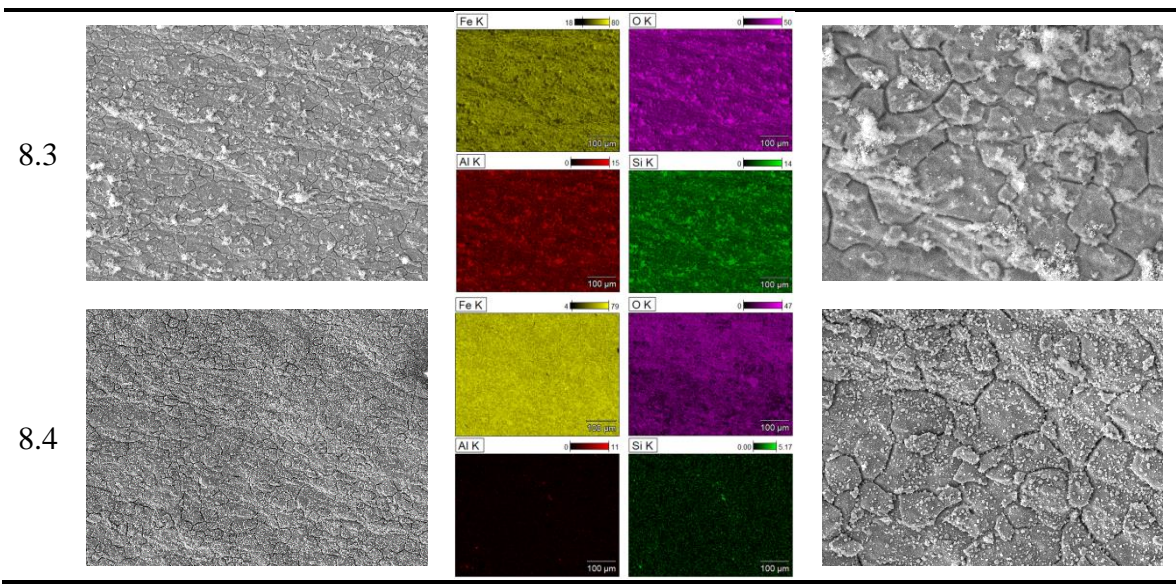




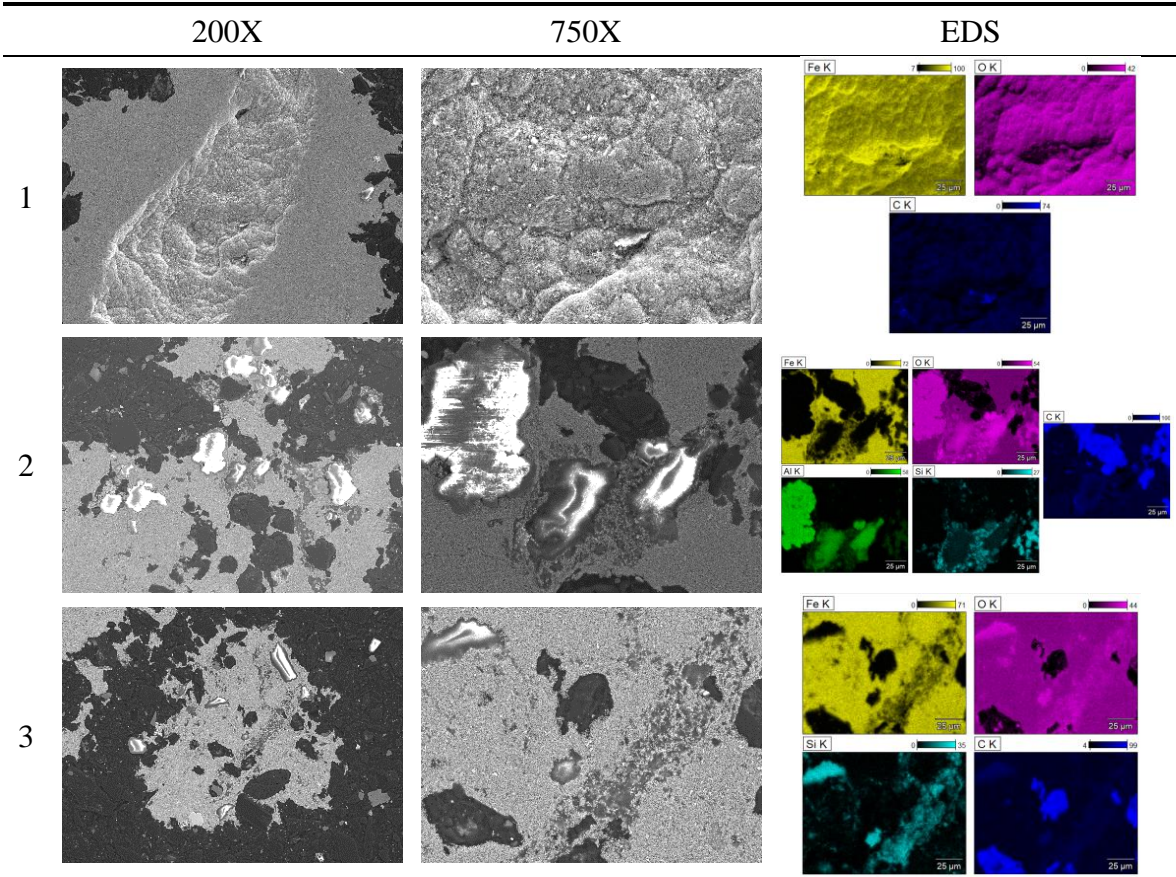


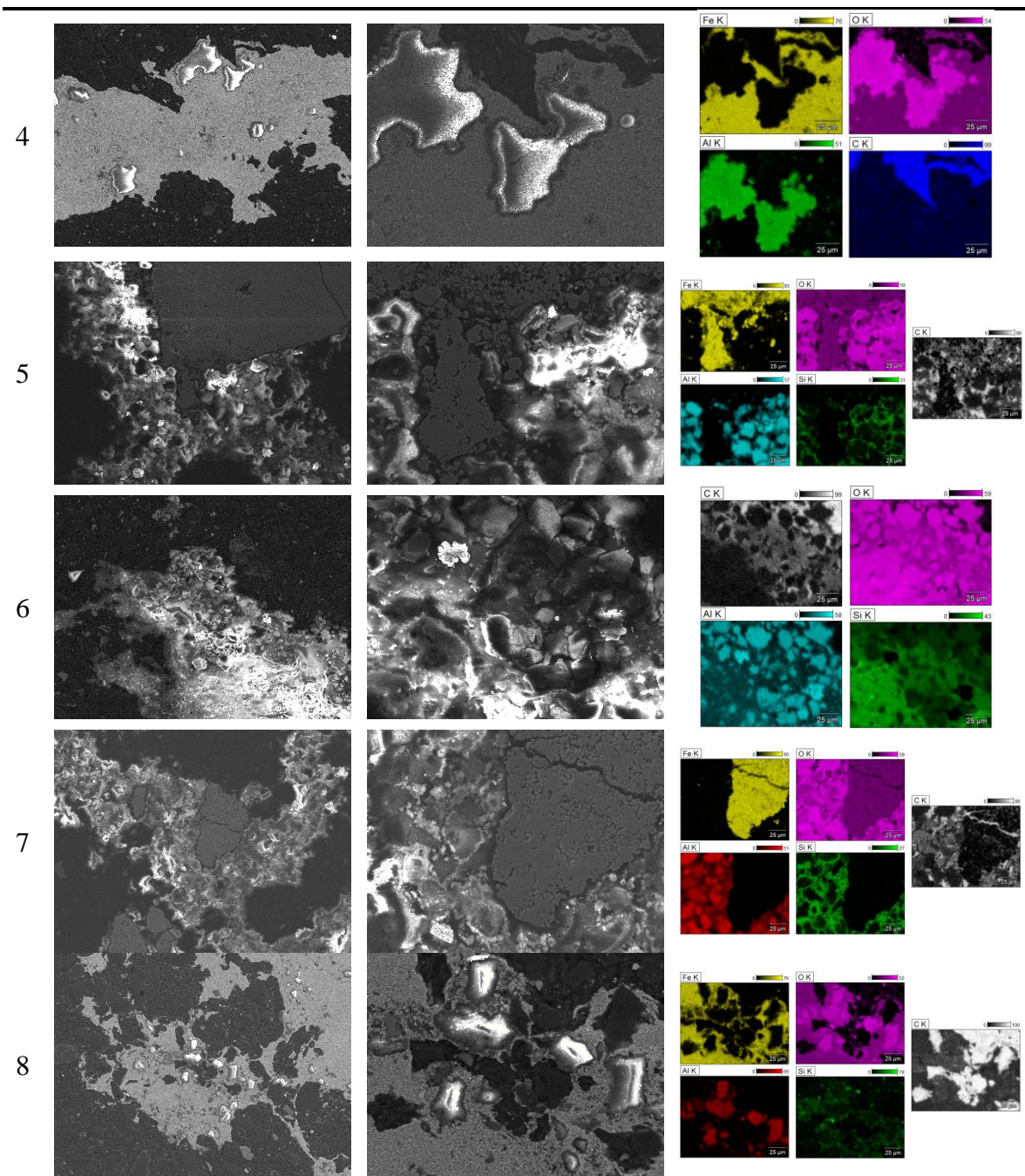






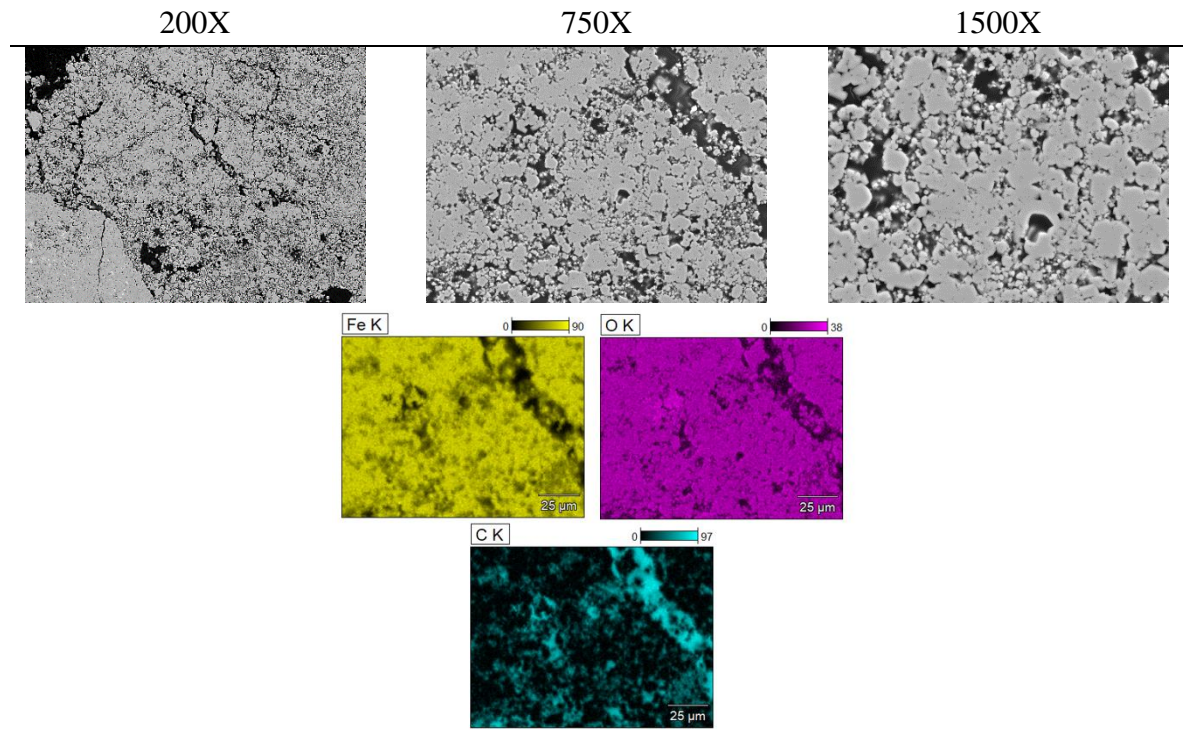
Filtrations in SEM buttons







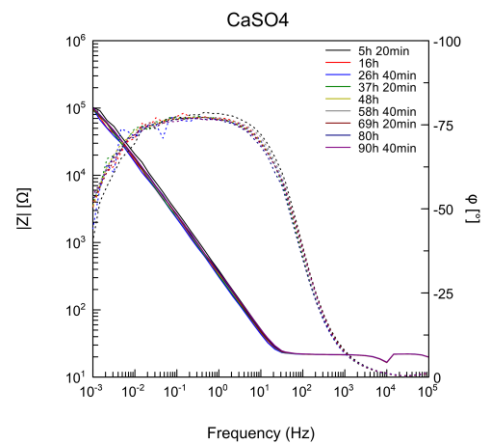
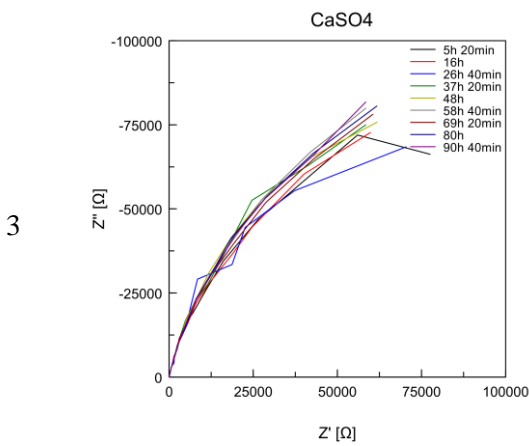
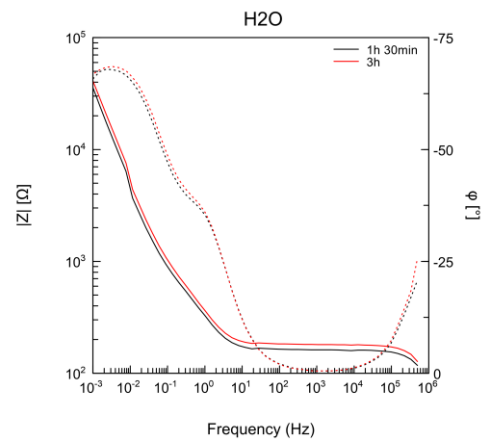
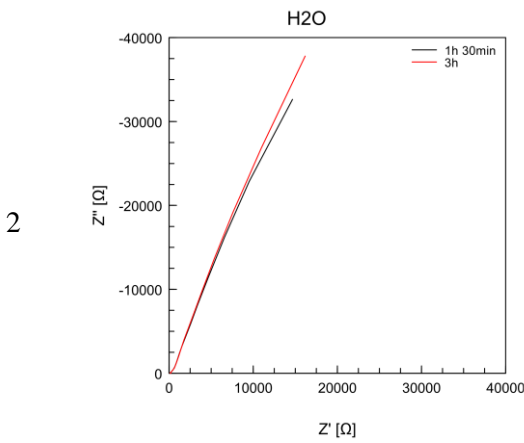
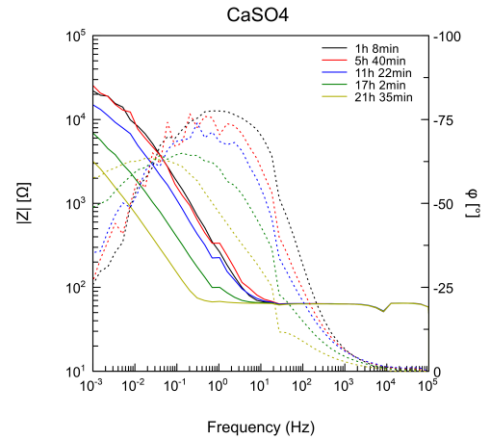
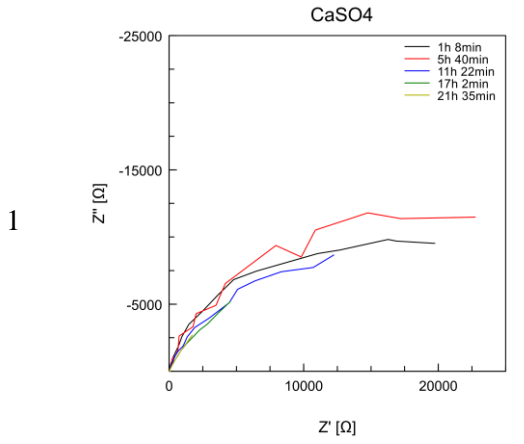
Magnetite powder from Loviisa NPP



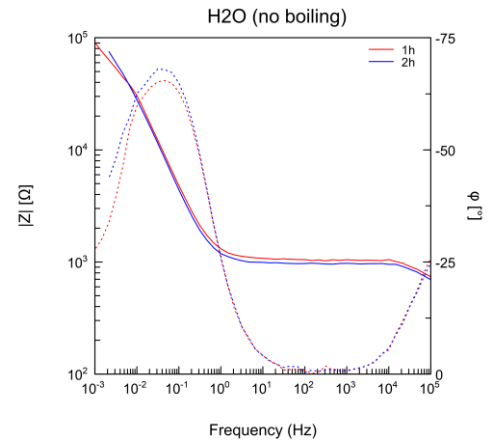
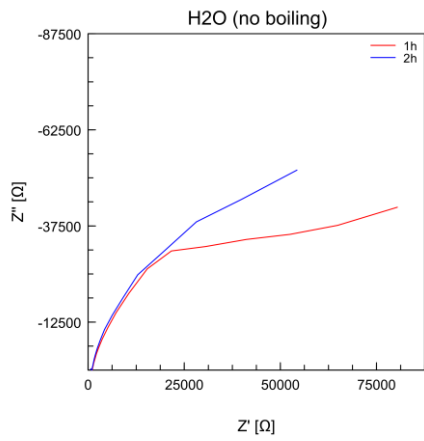
# Appendix V EIS – Nyquist and Bode plots

Nyquist

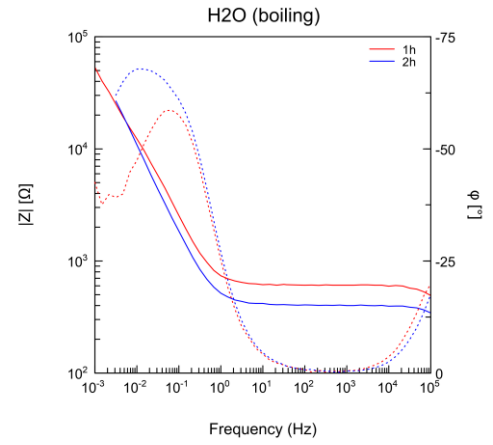
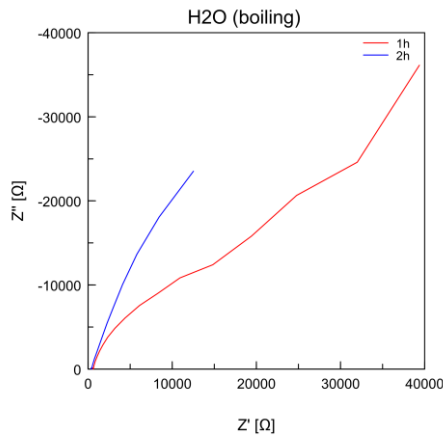
Bode



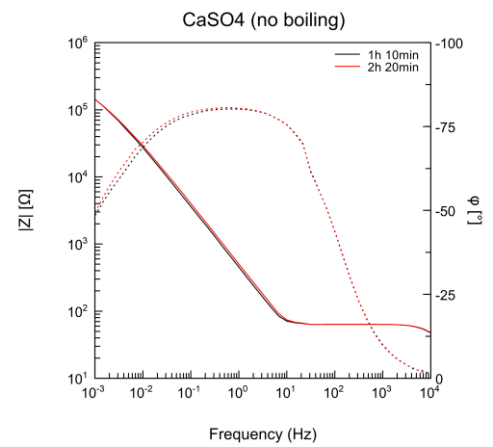
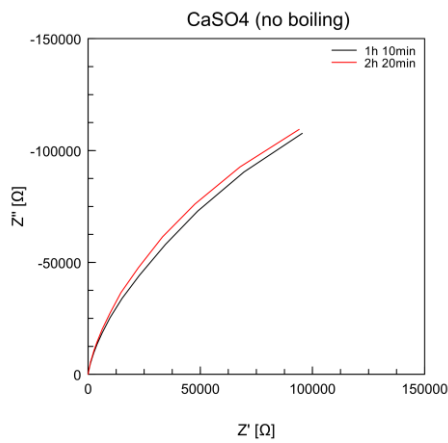
4



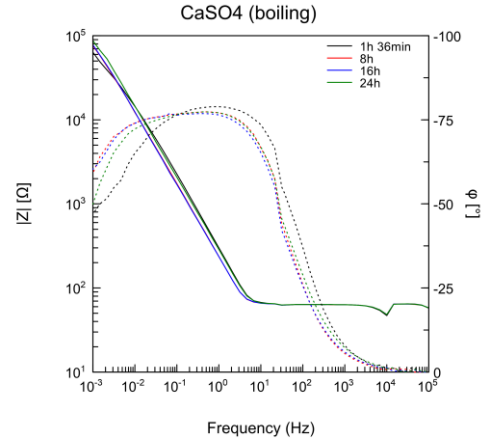
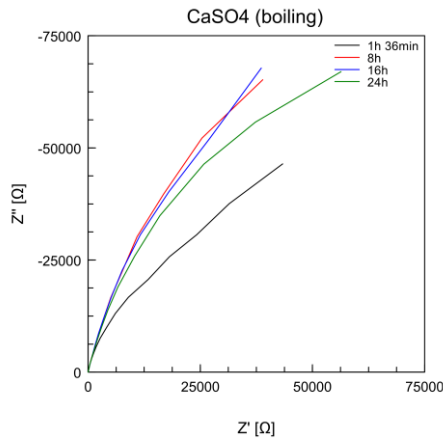
5



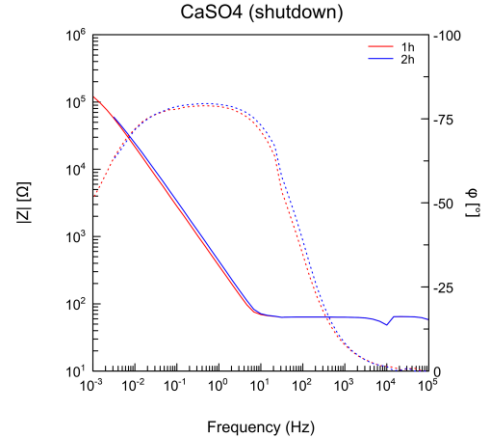
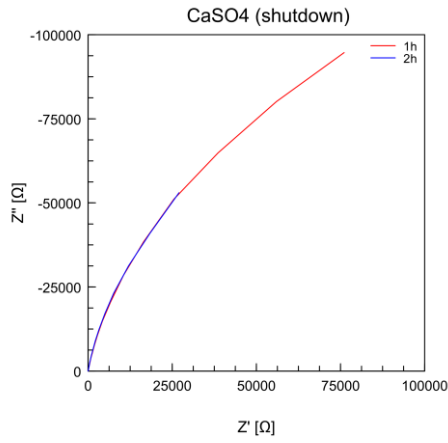
6



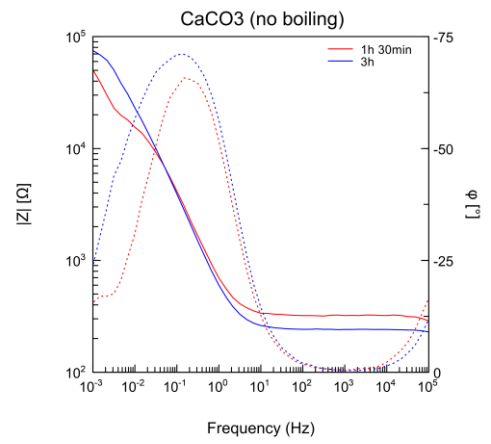
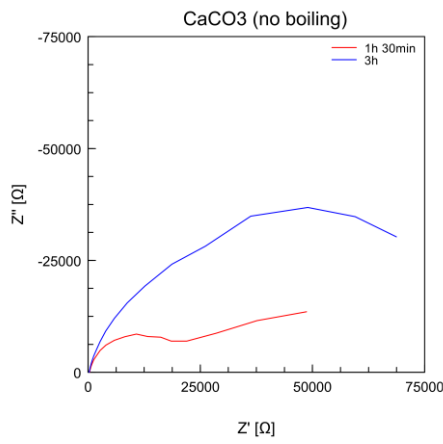
7



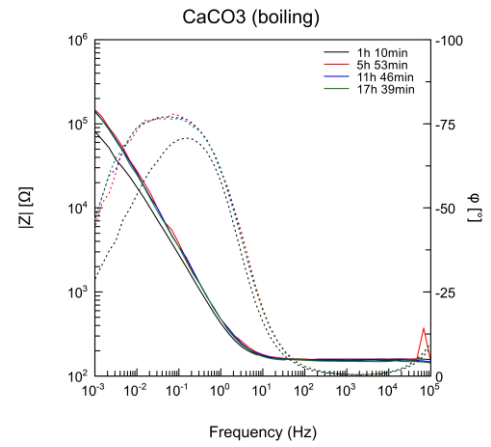
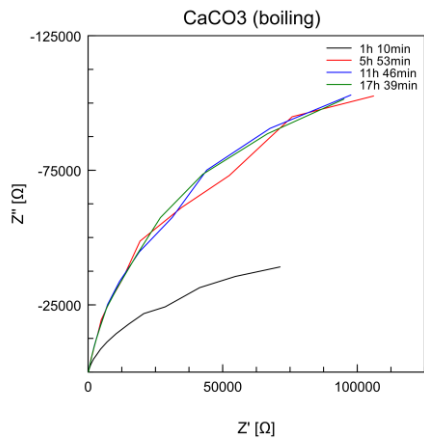
8



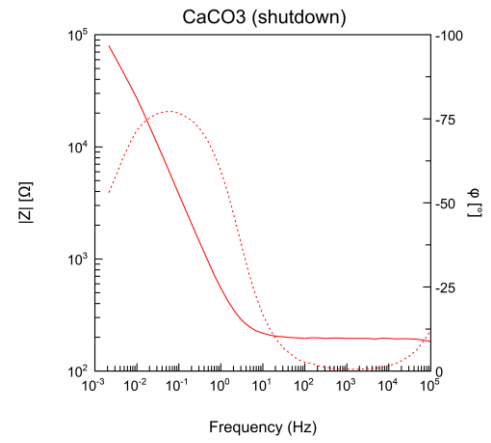
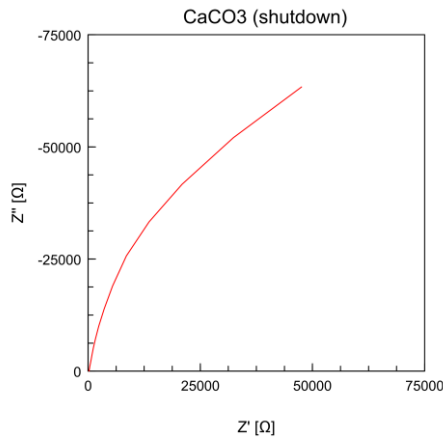
9



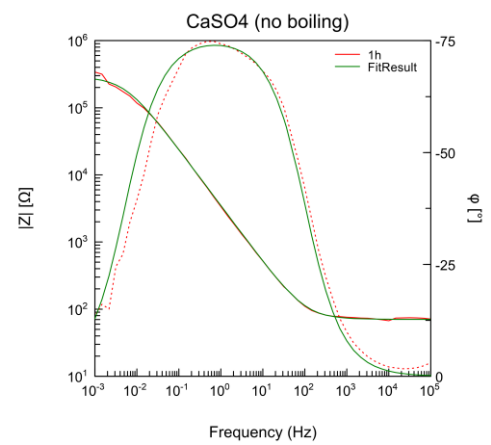
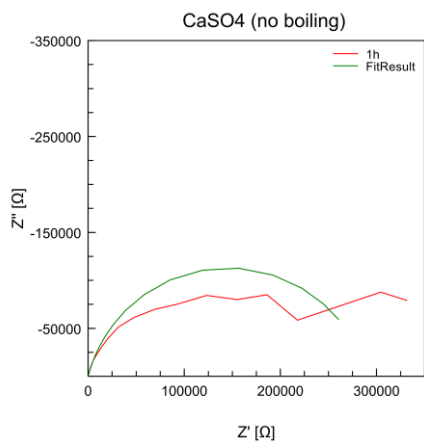
10



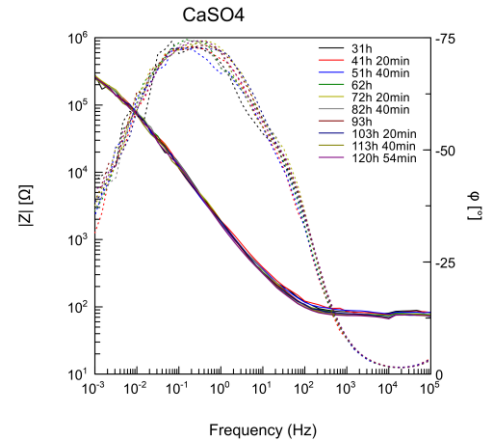
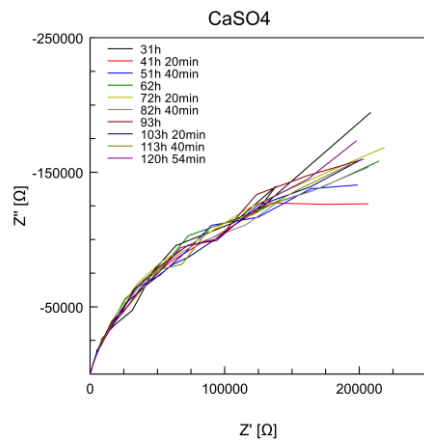
11



12



13



14

